Université de Neuchâtel
Institut de Microtechnique

# Polarization Optics of Periodic Media

Thèse

Présentée à la Faculté des Sciences pour obtenir le grade de docteur ès sciences par

Christian Bohley

Neuchâtel, avril 2004

IMPRIMATUR POUR LA THESE

# Polarization Optics of Periodic Media

**M. Christian BOHLEY**

---

UNIVERSITE DE NEUCHATEL

FACULTE DES SCIENCES

La Faculté des sciences de l'Université de Neuchâtel, sur le rapport des membres du jury

MM. R. Dändliker (directeur de thèse), H.-P. Herzig, J. Grupp (Asulab Marin) et H. Stark (Konstanz D)

autorise l'impression de la présente thèse.

Neuchâtel, le 20 avril 2004

La doyenne:

Martine Rahier

Denke, jemand zeigte auf eine Stelle der Iris in einem Rembrandtschen Auge und sagte: „Die Wände in meinem Zimmer sollen in dieser Farbe gemalt werden.“

Ludwig Wittgenstein, Bemerkungen über die Farben I, 58

Thesis Abstract

# *Polarization Optics of Periodic Media*

Christian Bohley
Applied Optics Group, Institute of Microtechnology, University Neuchâtel

The thesis describes different approaches for the simulation of light propagation in anisotropic media. It will focus, especially, on polarization effects in anisotropic media with periodic structure.
The work gives shortly a theoretical background with some essential considerations for polarization optics. This includes Maxwell's equations, the explanation of matrix concepts for optical elements and a mathematical discussion concerning the conditions for a possible separation of problems for two particular orthogonal polarizations.
Methods for the simulation of light propagation with application examples for each method are described. The introduced methods will be used to analyze periodic or quasi-periodic structures.
The 4x4 matrix method is used for the investigation of the reflection behaviour of cholesteric liquid crystals. Expanding this method by statistical means to inhomogeneous liquid crystals such as polymer-dispersed liquid crystals are investigated. Moreover, a special optimization method for cholesteric Bragg filters is proposed.
A space-grid time-domain method is presented and applied to liquid crystal gratings, for which the director configurations are calculated explicitly.
The last chapter deals with special phases of chiral nematic liquid crystals: the Blue Phases. The diffraction effects of Blue Phase structures are examined applying a 4x4 matrix method. The method was extended to be applicable to anisotropic crystal problems. The polarization and interference effects are described. Finally, Mueller matrices of the light, which is Bragg reflected by the Blue Phase structures, are calculated and compared with published experimental values for the some components of the Mueller matrices. Additionally, experimental aspects like preparation, polymerization and measurements of Blue Phases are presented and evaluated.

## TABLE OF CONTENTS


**1 INTRODUCTION ..... 5**

**2 ANALYTICAL BACKGROUND ..... 7**

2.1 MAXWELL'S EQUATIONS ..... 7
2.2 SEPARATION OF POLARIZATIONS FOR 2D ANISOTROPIC PROBLEMS ..... 8
2.3 SEPARATION OF POLARIZATIONS FOR INHOMOGENEOUS ISOTROPIC PROBLEMS ..... 9
2.4 DIELECTRIC TENSOR AND INDEX ELLIPSOID ..... 10
2.5 MATRIX CONCEPTS ..... 12
*2.5.1 THE JONES CONCEPT ..... 12*
*2.5.2 THE STOKES CONCEPT ..... 13*
2.6 CONCLUSIONS ..... 16

**3 SIMULATION METHODS AND EXAMPLES ..... 18**

3.1 THE MATRIX METHODS ..... 18
*3.1.1 THE 4x4 BERREMAN METHOD ..... 18*
*3.1.2 PROPAGATION IN CHOLESTERIC LIQUID CRYSTALS ..... 23*
*3.1.3 APODIZATION OF CHOLESTERIC BRAGG FILTERS ..... 24*
*3.1.4 COLOR OF THE LIGHT REFLECTED BY CHOLESTERIC LIQUID CRYSTALS 27*
*3.1.5 REFLECTION BY POLYMER-DISPERSED CLC ..... 29*
*3.1.6 DEPOLARIZATION EFFECTS FOR REFLECTION BY POLYMER DISPERSED CHOLESTERIC LIQUID CRYSTALS ..... 35*
*3.1.7 STACKED SYSTEMS OF POLYMER-DISPERSED CHOLESTERIC LIQUID CRYSTALS ..... 38*
*3.1.8 CONCLUSIONS ..... 40*
3.2 SPACE-GRID TIME-DOMAIN TECHNIQUES ..... 41
*3.2.1 DESCRIPTION OF THE FDTD METHOD ..... 42*
*3.2.2 NEMATIC LIQUID CRYSTAL CAPILLARIES ..... 46*
*3.2.3 LIQUID CRYSTAL GRATINGS ..... 51*
*3.2.4 CONCLUSIONS ..... 58*

**4 BLUE PHASES ..... 60**

4.1 INTRODUCTION ..... 60
4.2 BLUE PHASE LATTICES ..... 61
*4.2.1 STRUCTURE MODELS ..... 61*
*4.2.2 BRAGG REFLECTION OF SIMPLE CUBIC CRYSTALS ..... 65*
4.3 PLANE WAVE APPROACH TO THE OPTICS OF BLUE PHASES ..... 67
*4.3.1 MATRIX METHOD FOR ANISOTROPIC CRYSTALS ..... 67*
*4.3.2 APPLICATIONS TO THE BLUE PHASE II STRUCTURE ..... 71*
4.4 EXPERIMENTAL RESULTS ..... 75
*4.4.1 PREPARATION AND APPEARANCE OF BPII CRYSTALS ..... 75*
*4.4.2 POLYMERIZATION OF BP CRYSTALS ..... 76*
*4.4.3 DIFFRACTION PATTERNS IN EXPERIMENT AND SIMULATION ..... 77*
*4.4.4 BLUE PHASE OF DYE DOPED LIQUID CRYSTALS ..... 79*
*4.4.5 CONCLUSIONS ..... 81*

**5 SUMMMARY AND CONCLUSIONS ..... 82**

**6 REFERENCES ..... 84**

# 1 INTRODUCTION

The progress of optical sciences over the last 50 years was caused by several developments: the invention of the laser, the discovery and synthesis of new optically relevant materials (such as liquid crystals), and the manufacturing of microstructures. According to the enlarged features of optical elements, their design became more and more complex. This required a better understanding of the behavior of light in complex structured media.

The thesis describes different approaches for the simulation of light propagation. Especially, I will focus on periodic media, possibly anisotropic and polarization sensitive.

Chapter 2 of this work gives shortly a theoretical background with some essential considerations for polarization optics. This includes Maxwell's equations, the explanation of matrix concepts for optical elements and a mathematical discussion concerning the conditions for a possible separation of the problems for two particular polarizations.

Chapter 3 describes three methods for the simulation of light propagation with application examples for each method. The introduced methods will be applied to periodic or quasi-periodic structures.

First we show how the 4x4 matrix method can be used for stratified or quasi-stratified anisotropic structures. In this method the light is assumed to propagate as plane waves through anisotropic materials. We used this method for the investigation of the reflection behaviour of cholesteric liquid crystals. Expanding this method by statistical means, inhomogeneous liquid crystals such as polymer-dispersed cholesteric liquid crystals are investigated. Moreover, a special optimization method for cholesteric Bragg filters is proposed.

Second, we present a space-grid time-domain method that uses directly a discretization of Maxwell's equations. Starting with an discretization of the simulation domain with an appropriate spatial step, a computational time evolution is proceeded by an explicit updating scheme. The discretization has to be adapted to the gradient of the dielectric tensor of the material. The special rigorous method used here is the finite-difference time-domain method. It will be applied to liquid crystal gratings, for which the director configurations are calculated explicitly.

Chapter 4 deals with special phases of chiral nematic liquid crystals: the Blue Phases. This phase has extraordinary properties because of the three-dimensional structure, which is untypical for the liquid crystal world, although there exist other cubic phases. Blue Phases exhibit lattice structures with a period of the order of the visible wavelengths and therefore they show visible Bragg reflection. They have been studied in the past theoretically and practically and it was figured out that Blue Phases are optically active but not birefringent. In this chapter, the diffraction effects of Blue Phase structures are

examined applying a 4x4 method like the one presented in chapter 3. The method was extended to be applicable to anisotropic crystal problems. The polarization and interference effects are described. Finally, Müller matrices of the light, which is Bragg reflected by the Blue Phase structures, are calculated and compared with published values for some components of the Mueller matrices. Additionally, experimental aspects like preparation, polymerization and measurements of Blue Phases are presented and evaluated.
In chapter 5 the conclusions of the thesis are summarized.

Some results have been published previously in:


C. Bohley, T. Scharf, R. Klappert, J. Grupp, "Reflection of multi-domain structured cholesteric liquid crystals", *Proc. SPIE* (*Liquid Crystals V)* **4463**, 181 (2001)

C. Bohley, T. Scharf, "Depolarization effects of light reflected by domain-structured cholesteric liquid crystals", *Opt. Comm.* **214**, 193 (2002)

T. Scharf, C. Bohley, "Light propagation through alignment-patterned liquid crystal gratings", *Mol. Cryst. Liq. Cryst.* **375**, 491 (2002)

C. Bohley, T. Scharf, "Depolarization of light reflected by stacked displays from multi-domain structured cholesteric liquid crystals", *Proc. of the 22nd International Display Research Conference*, Nice (2002)

C. Bohley, T. Scharf, "Blue Phases as Photonic Crystals", *Proc. SPIE, (Physics, Theory and Applications of Periodic Structures in Optics II)* **5184**, 202 (2003)

C. Bohley, T. Scharf, "Optics of cholesteric Blue Phases", *Proc. of the ICO topical meeting on Polarization Optics*, Joensuu (2003)

C. Bohley, T. Scharf, "Polarization of light reflected by cholesteric Blue Phases", *J. Opt. A* **6**, 77 (2004)

# 2 ANALYTICAL BACKGROUND

## 2.1 MAXWELL'S EQUATIONS

The behavior of the time-dependent electromagnetic field is described by the Maxwell's equations [Born & Wolf 1959]

$$\nabla \times \mathbf{E} = -\mu_0 \mu \frac{\partial \mathbf{H}}{\partial t} \quad , \quad \nabla \times \mathbf{H} = \varepsilon_0 \boldsymbol{\varepsilon} \frac{\partial \mathbf{E}}{\partial t} \quad , \tag{2.1}$$

where **E** and **H** are the electric and magnetic field vectors in a Cartesian coordinate system (x,y,z), $\boldsymbol{\varepsilon}$ is the dielectric tensor (locally variant), $\mu$ the magnetic permeability and $\mu_0$ and $\varepsilon_0$ are constants. These equations hold if the electric charge density and the electric current density are assumed to be zero.
Furthermore, in this chapter *all materials are assumed as nonabsorbing and nongyroscopic.* For isotropic materials the dielectric tensor is a scalar and for anisotropic non-absorbing materials a symmetric three dimensional tensor [Born & Wolf 1959].
For a homogeneous medium the stationary plane wave equations

$$\mathbf{E}(\mathbf{r}, t) = \mathbf{E_0} \exp(i(\omega t - \mathbf{kr})) \quad , \quad \mathbf{H}(\mathbf{r}, t) = \mathbf{H_0} \exp(i(\omega t - \mathbf{kr})) \tag{2.2}$$

are valid, where **r** is the position vector, **k** the wave vector and $\omega$ the angular frequency. For an inhomogeneous medium we get together with (2.1) the Maxwell's equations in matrix description

$$\begin{pmatrix} 0 & 0 & 0 & 0 & -\frac{\partial}{\partial z} & \frac{\partial}{\partial y} \\ 0 & 0 & 0 & \frac{\partial}{\partial z} & 0 & -\frac{\partial}{\partial x} \\ 0 & 0 & 0 & -\frac{\partial}{\partial y} & \frac{\partial}{\partial x} & 0 \\ 0 & \frac{\partial}{\partial z} & -\frac{\partial}{\partial y} & 0 & 0 & 0 \\ -\frac{\partial}{\partial z} & 0 & \frac{\partial}{\partial x} & 0 & 0 & 0 \\ \frac{\partial}{\partial y} & -\frac{\partial}{\partial x} & 0 & 0 & 0 & 0 \end{pmatrix} \begin{pmatrix} E_x \\ E_y \\ E_z \\ H_x \\ H_y \\ H_z \end{pmatrix} = i\frac{\omega}{c} \begin{pmatrix} \varepsilon_{xx} & \varepsilon_{xy} & \varepsilon_{xz} & 0 & 0 & 0 \\ \varepsilon_{yx} & \varepsilon_{yy} & \varepsilon_{yz} & 0 & 0 & 0 \\ \varepsilon_{zx} & \varepsilon_{zy} & \varepsilon_{zz} & 0 & 0 & 0 \\ 0 & 0 & 0 & \mu & 0 & 0 \\ 0 & 0 & 0 & 0 & \mu & 0 \\ 0 & 0 & 0 & 0 & 0 & \mu \end{pmatrix} \begin{pmatrix} E_x \\ E_y \\ E_z \\ H_x \\ H_y \\ H_z \end{pmatrix}, \tag{2.3}$$

where $c = (\varepsilon_0 \mu_0)^{-1/2}$ is the vacuum speed of light.

## 2.2 SEPARATION OF POLARIZATIONS FOR 2D ANISOTROPIC PROBLEMS

The differential vector equation (2.3) holds for an inhomogeneous anisotropic material in 3D space. This equation can only be solved analytically in some special cases, but under certain circumstances it is possible to simplify the system of the equations by separation. Let us consider light propagating in the x-y-plane (i.e. no variation in z-direction), as shown in Fig 2.1. We distinguish two main polarizations: the transverse magnetic (TM)

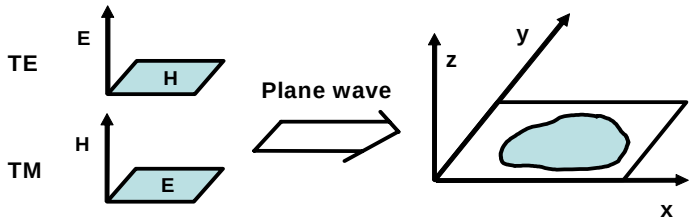


Fig. 2.1: Geometry and polarization definitions for the two dimensional problem

polarization and the transverse electric (TE) polarization. For the TM mode only the field components $E_x$, $E_y$ and $H_z$ are non-zero, whereas $E_z = H_x = H_y = 0$. For the TE mode only the components $E_z$, $H_x$ and $H_y$ are non-zero. Note, that in both cases light is propagating in the x-y-plane. What are the conditions for the dielectric tensor in a two-dimensional material domain that the propagation of these two orthogonal polarizations is completely independent, i.e., that an entering TE wave remains TE polarized during the propagation in the simulation domain and the same for TM polarization. This will be the case, if (2.3) is separable into two systems of differential equations, the first with the field components $E_x$, $E_y$, $H_z$ (TM) and the second with $E_z$, $H_x$ and $H_y$ (TE). In order to examine this, we rearrange the fields in (2.3), taking into account that all derivatives $\partial/\partial z$ are zero. We get then

$$\begin{pmatrix} i\frac{\omega}{c}\varepsilon_{xx} & i\frac{\omega}{c}\varepsilon_{xy} & i\frac{\omega}{c}\varepsilon_{xz} & 0 & 0 & -\frac{\partial}{\partial y} \\ i\frac{\omega}{c}\varepsilon_{yx} & i\frac{\omega}{c}\varepsilon_{yy} & i\frac{\omega}{c}\varepsilon_{yz} & 0 & 0 & \frac{\partial}{\partial x} \\ -\frac{\partial}{\partial y} & \frac{\partial}{\partial x} & 0 & 0 & 0 & i\frac{\omega}{c}\mu \\ 0 & 0 & \frac{\partial}{\partial y} & i\frac{\omega}{c}\mu & 0 & 0 \\ 0 & 0 & -\frac{\partial}{\partial x} & 0 & i\frac{\omega}{c}\mu & 0 \\ i\frac{\omega}{c}\varepsilon_{zx} & i\frac{\omega}{c}\varepsilon_{zy} & i\frac{\omega}{c}\varepsilon_{zz} & \frac{\partial}{\partial y} & -\frac{\partial}{\partial x} & 0 \end{pmatrix} \begin{pmatrix} E_x \\ E_y \\ H_z \\ H_x \\ H_y \\ E_z \end{pmatrix} = \mathbf{0} \quad . \tag{2.4}$$

Exchanging the columns 3 and 6 of the matrix in the left side of (2.4) gives

$$\begin{pmatrix} i\frac{\omega}{c}\varepsilon_{xx} & i\frac{\omega}{c}\varepsilon_{xy} & -\frac{\partial}{\partial y} & i\frac{\omega}{c}\varepsilon_{xz} & 0 & 0 \\ i\frac{\omega}{c}\varepsilon_{yx} & i\frac{\omega}{c}\varepsilon_{yy} & \frac{\partial}{\partial x} & i\frac{\omega}{c}\varepsilon_{yz} & 0 & 0 \\ -\frac{\partial}{\partial y} & \frac{\partial}{\partial x} & i\frac{\omega}{c}\mu & 0 & 0 & 0 \\ 0 & 0 & 0 & i\frac{\omega}{c}\mu & 0 & \frac{\partial}{\partial y} \\ 0 & 0 & 0 & 0 & i\frac{\omega}{c}\mu & -\frac{\partial}{\partial x} \\ i\frac{\omega}{c}\varepsilon_{zx} & i\frac{\omega}{c}\varepsilon_{zy} & 0 & \frac{\partial}{\partial y} & -\frac{\partial}{\partial x} & i\frac{\omega}{c}\varepsilon_{zz} \end{pmatrix} \begin{pmatrix} E_x \\ E_y \\ H_z \\ H_x \\ H_y \\ E_z \end{pmatrix} = \mathbf{0} \quad . \tag{2.5}$$

It means a complete decoupling of the differential equation systems for TE and TM polarization if the non-diagonal 3x3 submatrices are zero, i.e., if $\varepsilon_{xz} = \varepsilon_{yx} = 0$. So, the dielectric tensor $\varepsilon$ of the material has to have the form

$$\boldsymbol{\varepsilon} = \begin{pmatrix} \varepsilon_{xx} & \varepsilon_{xy} & 0 \\ \varepsilon_{xy} & \varepsilon_{yy} & 0 \\ 0 & 0 & \varepsilon_{zz} \end{pmatrix} \quad . \tag{2.6}$$

Later, in chapter 3.3, we will investigate liquid crystal materials having a dielectric tensor of the form (2.6) and we will make use of the polarization decoupling into TE and TM mode.

## 2.3 SEPARATION OF POLARIZATIONS FOR INHOMOGENEOUS ISOTROPIC PROBLEMS

It follows from equation (2.5) that the inhomogeneous isotropic 2D problem allows also to separate the TE and TM modes, because for an isotropic material all non-diagonal elements of the dielectric tensor are zero. But for the 3D problem the variations of the fields in z-direction may be non-zero and from (2.3) we get

$$\begin{pmatrix} i\frac{\omega}{c}\varepsilon & 0 & 0 & 0 & \frac{\partial}{\partial z} & -\frac{\partial}{\partial y} \\ 0 & i\frac{\omega}{c}\varepsilon & 0 & -\frac{\partial}{\partial z} & 0 & \frac{\partial}{\partial x} \\ 0 & 0 & i\frac{\omega}{c}\varepsilon & \frac{\partial}{\partial y} & -\frac{\partial}{\partial x} & 0 \\ 0 & -\frac{\partial}{\partial z} & \frac{\partial}{\partial y} & i\frac{\omega}{c}\mu & 0 & 0 \\ \frac{\partial}{\partial z} & 0 & -\frac{\partial}{\partial x} & 0 & i\frac{\omega}{c}\mu & 0 \\ -\frac{\partial}{\partial y} & \frac{\partial}{\partial x} & 0 & 0 & 0 & i\frac{\omega}{c}\mu \end{pmatrix} \begin{pmatrix} E_x \\ E_y \\ E_z \\ H_x \\ H_y \\ H_z \end{pmatrix} = \mathbf{0} \quad . \tag{2.7}$$

The matrix at the left side in (2.7) can not be rearranged such that the 6x6 matrix separates into non-diagonal 3x3 submatrices, although there are 18 non-zero elements. This can be shown algebraically. It follows that for the general isotropic 3D problem the decoupling of TE and TM modes is not possible.

## 2.4 DIELECTRIC TENSOR AND INDEX ELLIPSOID

The dielectric tensor $\boldsymbol{\varepsilon}$ that appears in (2.1) links the displacement vector **D** and the electric field vector **E**. $\boldsymbol{\varepsilon}$ is a real scalar in nonabsorbing isotropic media and a real and symmetric tensor in nonabsorbing and nongyroscopic but anisotropic materials.
The energy density $U_e$ of the electric field **E** in the anisotropic medium is

$$U_e = \frac{1}{2}\mathbf{E}\cdot\mathbf{D} = \frac{1}{2}\sum_{i,j=1}^{3} E_i \varepsilon_{ij} E_j = \frac{1}{2}\sum_{i,j=1}^{3} \varepsilon_{ij}^{-1} D_j D_i \quad . \tag{2.8}$$

The surfaces of constant energy density $U_e$ in the **D** space can be determined with (2.8) as

$$\frac{x^2}{\varepsilon_{xx}} + \frac{y^2}{\varepsilon_{yy}} + \frac{z^2}{\varepsilon_{zz}} = \text{const.} \quad , \tag{2.9}$$

where $\varepsilon_{ii}$ are the diagonal elements of the dielectric tensor after rotating to be diagonal. These elements are called principal dielectric constants. Equation (2.9) describes an ellipsoid in Cartesian space, which is known as the index ellipsoid. With the help of this geometrical construction it is possible to find two independent plane waves with the orthogonal polarizations $\vec{D}_1$ and $\vec{D}_2$ that propagate in the medium along a given direction of the wave-vector $\vec{k}$ and their corresponding two indices of refraction $n_1$ and $n_2$ (see Fig. 2.2). A more detailed description can be found in [Yariv & Yeh 1984].

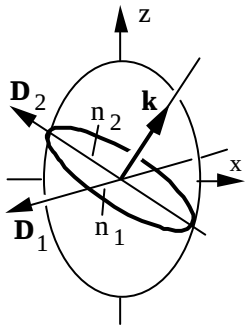


Fig. 2.2 : Biaxial index ellipsoid with polarization eigenstates $D_1$ , $D_2$ and eigenvalues of the indices of refraction $n_1$, $n_2$

The lengths of the semiaxes of the index ellipsoid described by (2.9) are

$$n_x = \sqrt{\varepsilon_{xx}}\ , \quad n_y = \sqrt{\varepsilon_{yy}} \qquad \text{and} \qquad n_z = \sqrt{\varepsilon_{zz}}\ ,$$

which are called also the principal indices of refraction of the material.
Nematic liquid crystals are optically modeled as uniaxial media, i.e. by an uniaxial index ellipsoid [Born &Wolf 1959]. $n_o = n_y = n_z$ is called the ordinary refractive index and $n_e = n_x$ the extraordinary index. Assuming the index ellipsoid positioned in a Cartesian

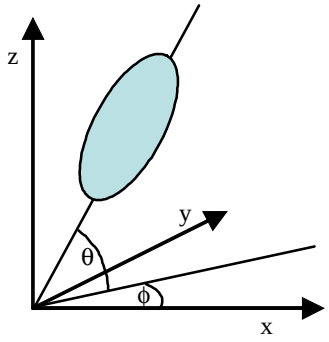


Fig. 2.3 : Orientation of the uniaxial index ellipsoid in the 3D space

coordinate system (x,y,z) with a twist ϕ with respect to the x-axis and a tilt θ with respect to the x-y-plane (see Fig. 2.3), the local dielectric tensor is then

$$\boldsymbol{\varepsilon} = R_z(\varphi)R_y(\theta)\begin{pmatrix} n_e^{\,2} & 0 & 0 \\ 0 & n_o^{\,2} & 0 \\ 0 & 0 & n_o^{\,2} \end{pmatrix} R_y^{-1}(\theta)R_z^{-1}(\varphi)\ , \qquad (2.10)$$

where $R_z(\varphi)$ and $R_y(\theta)$ are rotation matrices around the z-axis and the y-axis, respectively. The angles φ and θ are called twist and tilt. The diagonal matrix in (2.10) is

the dielectric tensor for the uniaxial medium with the major semi-axis lengths $n_e$, $n_o$, $n_o$, where the major axis with the semi-length $n_e$ lays parallel to the x-axis.
From (2.10) we get explicitly

$$\boldsymbol{\varepsilon} = \begin{pmatrix} n_0^2 + \Delta\varepsilon\cos^2\theta\cos^2\varphi & \Delta\varepsilon\cos^2\theta\,\sin\varphi\,\cos\varphi & \Delta\varepsilon\sin\theta\cos\theta\,\cos\varphi \\ \Delta\varepsilon\cos^2\theta\,\sin\varphi\,\cos\varphi & n_0^2 + \Delta\varepsilon\cos^2\theta\sin^2\varphi & \Delta\varepsilon\sin\theta\cos\theta\,\sin\varphi \\ \Delta\varepsilon\sin\theta\cos\theta\,\cos\varphi & \Delta\varepsilon\sin\theta\cos\theta\,\sin\varphi & n_0^2 + \Delta\varepsilon\sin^2\varphi \end{pmatrix} , \qquad (2.11)$$

where $\Delta\varepsilon = n_e^2 - n_o^2$. Note, that for $\theta = 0$ the dielectric tensor has the form of Eq. (2.6), and therefore decoupling of the TE and TM polarization for the planar anisotropic situation is possible if the major axis of the uniaxial index ellipsoids, also called director, remains in the propagation plane (x,y).

## 2.5 MATRIX CONCEPTS

### *2.5.1 THE JONES CONCEPT*

In order to characterize the propagation of plane waves of light and the effect of anisotropic optical devices, several matrix methods have been developed [Jones 1956, Born & Wolf 1959, McMaster 1961]. The light is presented only by its electric field and we inspect a monochromatic plane wave of angular frequency $\omega$, which propagates in direction z, perpendicularly to the x-y-plane. Then, the amplitude and phase behavior of the plane wave is determined by the two electric field vectors

$$E_x = E_{x0}\exp(i(\omega t+\phi_x)) \quad \text{and} \quad E_y = E_{y0}\exp(i(\omega t+\phi_y)) \ , \qquad (2.12)$$

from which we get

$$\text{real}(E_x) = E_{x0}\cos(\omega t+\phi_x) \quad \text{and} \quad \text{real}(E_y) = E_{y0}\cos(\omega t+\phi_y) \ . \qquad (2.13)$$

$E_{x0}$ and $E_{y0}$ are the amplitudes of the two electric fields, $\phi_x$ and $\phi_y$ their phases with the phase difference $\Delta = \phi_x - \phi_y$ . The column with the elements $E_x$ and $E_y$ is called Maxwell column and the corresponding time independent vector

$$\mathbf{E} = \begin{pmatrix} E_x \\ E_y \end{pmatrix} = \begin{pmatrix} E_{x0}\exp(i\varphi_x) \\ E_{y0}\exp(i\varphi_y) \end{pmatrix} \tag{2.14}$$

is called Jones vector. The polarization of the plane wave described by (2.14) is $\chi = E_x/E_y$ if we use the complex number notation for polarizations. The intensity of **E** is **EE*** (* means the complex conjugate). The vector in (2.14) has the same polarization and intensity as

$$\mathbf{E} = \begin{pmatrix} E_x \\ E_y \end{pmatrix} = \begin{pmatrix} E_{x0} \\ E_{y0}\exp(i\Delta) \end{pmatrix} \tag{2.15}$$

and in this form the Jones vector denotes the intensity and polarization properties of a plane wave. Because of the almost perfectly linear response of a medium to an electromagnetic wavefield at optical wavelengths [Gerrard 1975] a polarization dependent non-absorbing device can be characterized by a 2x2 matrix **J** which connects

$$\mathbf{E_{out}} = \begin{pmatrix} J_{11} & J_{12} \\ J_{21} & J_{22} \end{pmatrix} \begin{pmatrix} E_x \\ E_y \end{pmatrix} \quad . \tag{2.16}$$

the incoming and the outcoming wave in Jones vector description by
Note, that the elements of **J** are in general complex. The Jones matrix describes the linear transformation of the Jones vector of a plane wave by reflection or transmission. The Jones matrix of a device which is composed of several devices in series can be obtained as the product of the Jones matrices of the individual devices. Jones matrices can be measured with special setups by analyzing the outgoing intensities for incoming beams of different polarizations.

### *2.5.2 THE STOKES CONCEPT*

Using (2.15) for the field components, the so-called Stokes column **S** is defined as

$$\mathbf{S} = \begin{pmatrix} S_0 \\ S_1 \\ S_2 \\ S_3 \end{pmatrix} = \begin{pmatrix} E_{x0}^2 + E_{y0}^2 \\ E_{x0}^2 - E_{y0}^2 \\ 2E_{x0}E_{y0}\cos\Delta \\ 2E_{x0}E_{y0}\sin\Delta \end{pmatrix} \quad . \tag{2.17}$$

The four elements of **S** are directly obtained from intensity measurements and are related by

$$S_0^2 = S_1^2 + S_2^2 + S_3^2 \quad , \tag{2.18}$$

which can be shown by elementary algebra. $S_0$ is the intensity of the beam, $S_1$, $S_2$ and $S_3$ can have any real value between $-S_0$ and $+S_0$. Equation (2.18) allows a representation of the polarization states on the surface of a sphere, which is called Poincaré sphere (Fig. 2.4). Here, $S_1$, $S_2$ and $S_3$ may be regarded as Cartesian coordinates of a point P on a sphere of the radius $S_0$. Every possible state of polarization of a monochromatic plane

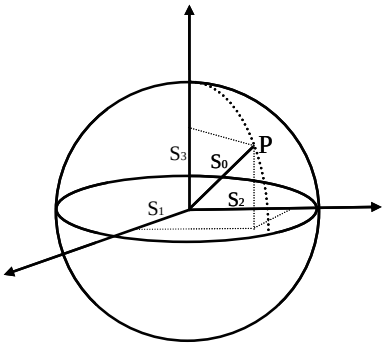


Fig. 2.4: Poincaré sphere representation of the polarization states of a monochromatic wave

wave corresponds to a point on the Poincaré sphere and vice versa. The right-handed circular polarization is presented by the north pole, the left-handed polarization by the south pole, the linear polarizations by the points in the equatorial plane and the elliptical states are represented by the points between the poles and the equatorial plane. The right-handed polarization points lie above the equatorial plane and the left-handed lie below. According the description of the polarization by complex numbers in 2.4.1, the ensemble of the polarization states is mapped onto the complex plane; here it is mapped on the surface of the Poincaré sphere and it exists an unique projection between them.

Contrary to the Jones concept, Stokes columns can also describe partially polarized light. This can be thought as combinations of several mutually incoherent beams of different polarizations. The combination can be obtained by addition of the intensities which are represented by the individual elements of the Stokes column, which are directly related to the so-called coherency matrix [Goodman 1985].

For partially polarized light the condition (2.18) will no longer be fulfilled. A “measure” for the “validity” of this condition can be the parameter

$$p = \frac{\sqrt{S_1^2 + S_2^2 + S_3^2}}{S_0} \quad , \tag{2.19}$$

which is called the degree of polarization. p is equal to 1 for fully polarized light (mathematically, this is valid for all Stokes columns which are transformed directly from Maxwell columns) and equal to 0 for non-polarized (natural) light which can be seen as a balanced mixture of all possible polarization states. Stokes columns with a degree of polarization between 0 and 1 represent partially polarized light beams. Stokes vectors of partially polarized light beams can also be presented with the help of the Poincaré sphere, but the corresponding points P will not lay on the surface of the sphere, but rather inside the sphere. The distance between P and the center is $pS_0$. In 3.1 we will make use of this representation.

Similarly to the Jones matrix that characterizes polarization sensitive devices, there exists also a matrix form for partially depolarizing devices. These matrices relate the Stokes vector of a light beam leaving an optical device with the Stokes vectors of the input beam. This matrix is called after its inventor Mueller matrix. It is a 4x4 matrix with real elements. The Stokes vectors **S** are then transformed by

$$\mathbf{S'} = \begin{pmatrix} S_0' \\ S_1' \\ S_2' \\ S_3' \end{pmatrix} = \begin{pmatrix} M_{11} & M_{12} & M_{13} & M_{14} \\ M_{21} & M_{22} & M_{23} & M_{24} \\ M_{31} & M_{32} & M_{33} & M_{34} \\ M_{41} & M_{42} & M_{43} & M_{44} \end{pmatrix} \begin{pmatrix} S_0 \\ S_1 \\ S_2 \\ S_3 \end{pmatrix} \quad . \tag{2.20}$$

Not every real 4x4 matrix can be a Mueller matrix **M,** there exist conditions for testing the consistence of a matrix to be a Mueller matrix [Brosseau 1998]. These conditions can be formulated as inequalities.

Mueller matrices can also be specified for non depolarizing devices. Then they are called Mueller-Jones matrices. It exists a mathematical correspondence between the Mueller-Jones and the Jones matrices, namely

$$\mathbf{M} = \mathbf{A}\left(\mathbf{J} \otimes \mathbf{J}^*\right)\mathbf{A}^{-1} \quad , \tag{2.21}$$

where **J** is the corresponding Jones Matrix, **M** the corresponding Mueller matrix, and **A** is defined by

$$\mathbf{A} = \begin{pmatrix} 1 & 0 & 0 & 1 \\ 1 & 0 & 0 & -1 \\ 0 & 1 & 1 & 0 \\ 0 & \mathrm{i} & -\mathrm{i} & 0 \end{pmatrix}, \tag{2.22}$$

where $\otimes$ designates the so-called Kronecker product (or outer product), which transforms two 2x2 matrices into a 4x4 matrix by multiplication of submatrices component for component. The form of **M** in terms of the Jones matrix elements is

$$\begin{pmatrix} \frac{1}{2}\left(|J_{11}|^2 + |J_{12}|^2 + |J_{21}|^2 + |J_{22}|^2\right) & \frac{1}{2}\left(|J_{11}|^2 - |J_{12}|^2 + |J_{21}|^2 - |J_{22}|^2\right) & \mathrm{Re}\left(J_{11}^* J_{12} + J_{21}^* J_{22}\right) & -\mathrm{Im}\left(J_{11}^* J_{12} + J_{21}^* J_{22}\right) \\ \frac{1}{2}\left(|J_{11}|^2 + |J_{12}|^2 - |J_{21}|^2 - |J_{22}|^2\right) & \frac{1}{2}\left(|J_{11}|^2 - |J_{12}|^2 - |J_{21}|^2 + |J_{22}|^2\right) & \mathrm{Re}\left(J_{11}^* J_{12} - J_{21}^* J_{22}\right) & -\mathrm{Im}\left(J_{11}^* J_{12} - J_{21}^* J_{22}\right) \\ \mathrm{Re}\left(J_{11}^* J_{21} + J_{12}^* J_{22}\right) & \mathrm{Re}\left(J_{11}^* J_{21} - J_{12}^* J_{22}\right) & \mathrm{Re}\left(J_{11}^* J_{22} + J_{12}^* J_{21}\right) & -\mathrm{Im}\left(J_{11}^* J_{22} - J_{12}^* J_{21}\right) \\ \mathrm{Im}\left(J_{11}^* J_{21} + J_{12}^* J_{22}\right) & \mathrm{Im}\left(J_{11}^* J_{21} - J_{12}^* J_{22}\right) & \mathrm{Im}\left(J_{11}^* J_{22} + J_{12}^* J_{21}\right) & \mathrm{Re}\left(J_{11}^* J_{22} - J_{12}^* J_{21}\right) \end{pmatrix}.$$

Mueller matrices of optical devices can be determined by Stokes vector measurements for different polarizations of the incident light, also for partially polarized light. Examples for Jones and Mueller matrices of particular devices and their measurement schemes can be found in [Gerrard & Burch 1975] and [Brosseau 1998].

## 2.6 CONCLUSIONS

In this chapter we presented the theoretical background for understanding the propagation of electromagnetic waves by Maxwell's equations in anisotropic media. From the matrix form of the Maxwell's equations, we figured out that decoupling of the TE and TM polarization for the planar anisotropic situation is only possible if the director of the uniaxial index ellipsoid remains in the plane of propagation. We will make use of this property in section 3.3, where 2D problems in liquid crystals are analyzed. A decoupling of TE and TM mode is evident for 2D isotropic inhomogeneous problems, but except for special cases not for 3D isotropic inhomogeneous problems.

The dielectric tensor representing an uniaxial optically anisotropic element arbitrarily oriented in the space was calculated as a function of the twist and tilt angles of its director. These relations will be needed in sections 3.1 and 3.3, where inhomogeneous liquid crystal structures are analyzed.

Matrix methods for polarization optics were introduced. The Jones concept uses the Maxwell column as an amplitude and phase description of a fully polarized plane wave.

The Jones matrix transforms the Maxwell column of the incoming beam into the Maxwell column of the outgoing beam. The Jones concept is an essential part of the 4x4 matrix method [Berreman 1972] that will be elucidated in 3.1.1 and applied in 3.1.3-7 and in chapter 4.

The basic element of the more general Stokes concept is the Stokes column, which can also describe partially polarized light. The Mueller matrix relates the Stokes vectors and describes the optical functionality of a polarizing device, which may change the degree of polarization of the incoming plane wave. The Stokes concept will be required in section 3.1.6 and chapter 4 of the present work in order to characterize depolarized light.

# 3 SIMULATION METHODS AND EXAMPLES

The Maxwell equations described in chapter 2 can only be handled analytically in special cases, such as plane waves in free space or in homogeneous anisotropic media, or media of special geometries. Therefore, a multitude of numerical methods has been developed, which are based on different approximations or geometrical assumptions. In this chapter we characterize 2 methods and apply them to particular problems.

## 3.1 THE MATRIX METHODS

A main idea of approximation methods for monochromatic light propagation is to reduce the number of the electromagnetic-field variables. This is e.g. possible if the medium is assumed to be stratified. The problem is then reduced for an isotropic medium to a 2D problem and after chapter 2.3 it can be separated into two independent orthogonal electric field components. The field components can be eliminated and the first order Maxwell differential equations can be replaced by second order differential equations.
These will be solved numerically in taking to account the dielectric properties of the medium. Every layer of the stratified medium is characterized by a matrix. 2x2 matrix methods for isotropic stratified media were introduced by Jones [Jones 1941] and Abelès [Abelès 1950].
We learned also from section 2.3 that the separation of orthogonal polarizations is generally not possible for the 2D or 3D anisotropic problem. But in assuming a stratified structure, the 3D problem can be reduced to the treatment of 4 electromagnetic field variables. This leads to a system of second order Maxwell equations or to the corresponding first order equation system. Matrix methods based on these equations were developed by Yeh [Yeh 1979] and Berreman [Berreman 1972]. Both methods introduce eigenmodes of the fields that will be ordered so that the 4x4 formalism reduces to a 2x2 Jones formalism in the limit of isotropic media. In the following, we will focus on the 4x4 method of Berreman, which can be considered as a generalization of the Abelès 2x2 matrix method [Abelès 1950].

### *3.1.1 THE 4x4 BERREMAN METHOD*

As shown in Fig. 3.1, we consider first a monochromatic plane wave obliquely incident from an isotropic ambient medium onto a homogeneous anisotropic layer perpendicular to the z-axis. The plane of incidence is the x-z plane.

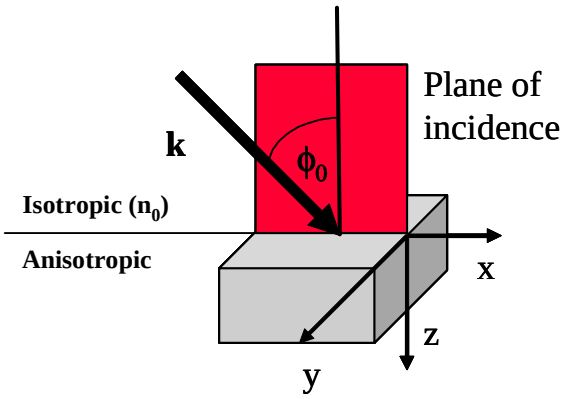


Fig. 3.1: Scheme of geometrical arrangement for a single homogeneous anisotropic layer

Note that, in contrast to the model of section 2.2, we treat here a three dimensional problem. However, the dielectric tensor is constant in the x-y plane and varies only as a function of z. Therefore, the problem is invariant in the y-direction, so that

$$\frac{\partial}{\partial y} = 0 \quad . \tag{3.1}$$

All waves that are excited by the incident plane wave $E = E_0 e^{i(\omega t - \mathbf{kr})}$ must have the same spatial dependence in the x-direction as the incident wave, which is the x component

$$\xi = \frac{\omega}{c} n_0 \sin\varphi_0 \quad , \tag{3.2}$$

of the wave vector, where $n_0$ is the refractive index of the ambient medium and $\phi_0$ the angle of incidence. Therefore, the variation of all fields in the x-direction is $\exp(-i\xi x)$ and

$$\frac{\partial}{\partial x} = -i\xi \quad . \tag{3.3}$$

The curl operator becomes with (3.1) and (3.3)

$$\nabla\times = \begin{pmatrix} 0 & -\frac{\partial}{\partial z} & \frac{\partial}{\partial y} \\ \frac{\partial}{\partial z} & 0 & -\frac{\partial}{\partial x} \\ -\frac{\partial}{\partial y} & \frac{\partial}{\partial x} & 0 \end{pmatrix} = \begin{pmatrix} 0 & -\frac{\partial}{\partial z} & 0 \\ \frac{\partial}{\partial z} & 0 & i\xi \\ 0 & -i\xi & 0 \end{pmatrix} \quad . \tag{3.4}$$

For the Maxwell equations (2.3) we get then

$$\begin{pmatrix} -\frac{\partial}{\partial z}H_y \\ \frac{\partial}{\partial z}H_x + i\xi H_z \\ -i\xi H_y \\ \frac{\partial}{\partial z}E_y \\ -\frac{\partial}{\partial z}E_x - i\xi E_z \\ i\xi E_y \end{pmatrix} = i\frac{\omega}{c}\begin{pmatrix} \varepsilon_{xx}E_x + \varepsilon_{xy}E_y + \varepsilon_{xz}E_z \\ \varepsilon_{yx}E_x + \varepsilon_{yy}E_y + \varepsilon_{yz}E_z \\ \varepsilon_{zx}E_x + \varepsilon_{zy}E_y + \varepsilon_{zz}E_z \\ \mu H_x \\ \mu H_y \\ \mu H_z \end{pmatrix} \tag{3.5}$$

and a linear dependence of $E_z$ and $H_z$ along z for the other field variables becomes evident with

$$E_z = -\frac{\xi c}{\varepsilon_{zz}\omega}H_y - \frac{\varepsilon_{zx}}{\varepsilon_{zz}}E_x - \frac{\varepsilon_{zy}}{\varepsilon_{zz}}E_y \quad \text{and} \quad H_z = \frac{\xi c}{\omega\mu}E_y \quad . \tag{3.6}$$

This leads to four linear homogeneous first order differential equations

$$\frac{\partial}{\partial z}\begin{pmatrix} E_x \\ H_y \\ E_y \\ -H_x \end{pmatrix} = \begin{pmatrix} -i\frac{\omega}{c}\left(-\frac{\xi c}{\omega}\frac{\varepsilon_{zx}}{\varepsilon_{zz}}E_x - \frac{1}{\varepsilon_{zz}}\frac{\xi^2 c^2}{\omega^2}H_y + \mu H_y - \frac{\xi c}{\omega}\frac{\varepsilon_{zy}}{\varepsilon_{zz}}E_y\right) \\ -i\frac{\omega}{c}\left(\varepsilon_{xx}E_x - \frac{\varepsilon_{xz}\varepsilon_{zx}}{\varepsilon_{zz}}E_x - \frac{\varepsilon_{xz}}{\varepsilon_{zz}}\frac{\xi c}{\omega}H_y - \frac{\varepsilon_{xz}\varepsilon_{zy}}{\varepsilon_{zz}}E_y + \varepsilon_{xy}E_y\right) \\ -i\frac{\omega}{c}(-\mu H_x) \\ -i\frac{\omega}{c}\left(\varepsilon_{yx}E_x - \frac{\varepsilon_{yz}\varepsilon_{zx}}{\varepsilon_{zz}}E_x - \frac{\varepsilon_{yz}}{\varepsilon_{zz}}\frac{\xi c}{\omega}H_y + \varepsilon_{yy}E_y - \frac{\xi^2 c^2}{\omega^2\mu}E_y - \frac{\varepsilon_{yz}\varepsilon_{zy}}{\varepsilon_{zz}}E_y\right) \end{pmatrix} \tag{3.7}$$

for the field variables $E_x$, $E_y$, $H_x$ and $H_y$ and we get the wave equation for the so-called generalized field vector $\boldsymbol{\psi} = [E_x, H_y, E_y, -H_x]$, which can be written in matrix form as

$$\frac{\partial}{\partial z}\begin{pmatrix} E_x \\ H_y \\ E_y \\ -H_x \end{pmatrix} = -i\frac{\omega}{c}\begin{pmatrix} -\frac{\xi c}{\omega}\frac{\varepsilon_{zx}}{\varepsilon_{zz}} & \mu - \frac{1}{\varepsilon_{zz}}\frac{\xi^2 c^2}{\omega^2} & -\frac{\xi c}{\omega}\frac{\varepsilon_{zy}}{\varepsilon_{zz}} & 0 \\ \varepsilon_{xx} - \frac{\varepsilon_{xz}\varepsilon_{zx}}{\varepsilon_{zz}} & -\frac{\varepsilon_{xz}}{\varepsilon_{zz}}\frac{\xi c}{\omega} & \varepsilon_{xy} - \frac{\varepsilon_{xz}\varepsilon_{zy}}{\varepsilon_{zz}} & 0 \\ 0 & 0 & 0 & \mu \\ \varepsilon_{yx} - \frac{\varepsilon_{yz}\varepsilon_{zx}}{\varepsilon_{zz}} & -\frac{\varepsilon_{yz}}{\varepsilon_{zz}}\frac{\xi c}{\omega} & \varepsilon_{yy} - \frac{\varepsilon_{yz}\varepsilon_{zy}}{\varepsilon_{zz}} - \frac{\xi^2 c^2}{\omega^2\mu} & 0 \end{pmatrix}\begin{pmatrix} E_x \\ H_y \\ E_y \\ -H_x \end{pmatrix} \tag{3.8}$$

or as

$$\frac{\partial}{\partial z}\boldsymbol{\Psi} = -i\frac{\omega}{c}\Delta\boldsymbol{\Psi} \quad , \tag{3.9}$$

where $\Delta$ is called the differential propagation matrix, which depends on the dielectric tensor of the anisotropic medium, the refraction index of the isotropic medium, the angle of incidence and the frequency of the light.
We consider now a layer between z and z+h. Equation (3.9) can be solved numerically by developing in the Taylor series

$$\boldsymbol{\Psi}(z+h) = (I - i\frac{\omega}{c}h\Delta - \frac{\omega^2 h^2}{2!c^2}\Delta^2 + i\frac{\omega^3 h^3}{3!c^3}\Delta^3 \pm ...)\boldsymbol{\Psi}(z) \quad . \tag{3.10}$$

This delivers the generalizes field vector $\boldsymbol{\psi}$ in z+h, if $\boldsymbol{\psi}$ is known in z. Equation (3.10) describes the linear matrix relationship between the generalized field vectors at both sides of an anisotropic layer of thickness h.

ANISOTROPIC STRATIFIED MEDIUM

Figure 3.2 shows an anisotropic stratified medium between two ambient isotropic media with the indices of refraction $n_0$ and $n_2$ , where the entering plane wave comes from the ambient medium with the index $n_0$.

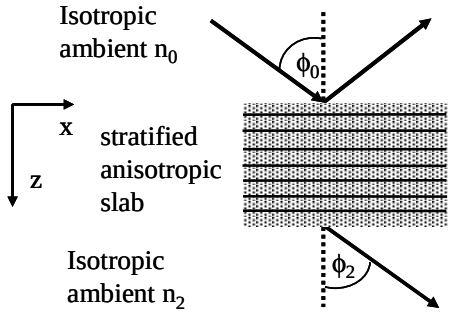


Fig. 3.2: Stratified anisotropic slab between isotropic ambient media

Let ($E_{ip}$, $E_{is}$), ($E_{rp}$, $E_{rs}$) and ($E_{tp}$, $E_{ts}$) be the components of the incident, reflected and transmitted electric field vectors, parallel (p) or perpendicular (s) to the plane of incidence x-z. Using the fact that the orthogonal electric and magnetic fields are related by $n_0$ respectively $n_2$ in the ambient isotropic media, i.e.,

$$\frac{H_{ip}}{E_{is}} = \frac{H_{is}}{E_{ip}} = n_0 \quad , \quad \frac{H_{rp}}{E_{rs}} = \frac{H_{rs}}{E_{rp}} = n_0 \quad \text{and} \quad \frac{H_{tp}}{E_{ts}} = \frac{H_{ts}}{E_{tp}} = n_2 \quad , \tag{3.11}$$

the generalized field vectors of incidence, reflection and transmission can be written as

$$\boldsymbol{\Psi}_i = \begin{pmatrix} E_{ip}\cos\varphi_0 \\ n_0 E_{ip} \\ E_{is} \\ n_0 E_{is}\cos\varphi_0 \end{pmatrix} \qquad \boldsymbol{\Psi}_r = \begin{pmatrix} -E_{rp}\cos\varphi_0 \\ n_0 E_{rp} \\ E_{rs} \\ -n_0 E_{rs}\cos\varphi_0 \end{pmatrix} \qquad \boldsymbol{\Psi}_t = \begin{pmatrix} E_{tp}\cos\varphi_2 \\ n_2 E_{tp} \\ E_{ts} \\ n_2 E_{ts}\cos\varphi_2 \end{pmatrix} \quad . \tag{3.12}$$

We will now consider a plane wave, which propagates in the stratified medium from one homogeneous anisotropic layer to the next. This plane wave can be described by a generalized field vector $\boldsymbol{\psi}$. The product $\mathbf{L}$ of the matrices in (3.10) for every single layer relates the generalized field vectors $\boldsymbol{\psi}_i+\boldsymbol{\psi}_r$ and $\boldsymbol{\psi}_t$. With (3.12) we get

$$\begin{pmatrix} E_{tp}\cos\varphi_2 \\ n_2 E_{tp} \\ E_{ts} \\ n_2 E_{ts}\cos\varphi_2 \end{pmatrix} = \begin{pmatrix} l_{11} & l_{12} & l_{13} & l_{14} \\ l_{21} & l_{22} & l_{23} & l_{24} \\ l_{31} & l_{32} & l_{33} & l_{34} \\ l_{41} & l_{42} & l_{43} & l_{44} \end{pmatrix} \begin{pmatrix} (E_{ip} - E_{rp})\cos\varphi_0 \\ n_0 (E_{ip} + E_{rp}) \\ E_{is} + E_{rs} \\ (E_{is} - E_{rs})\, n_0\cos\varphi_0 \end{pmatrix} \quad . \tag{3.13}$$

Note that the material inside one layer is assumed to be homogeneous. Therefore, materials with continuously changing dielectric properties have to be divided in sufficiently thin layers.

Equation (3.13) results in a system of 4 linear equations for the 4 unknowns $E_{rp}$, $E_{rs}$, $E_{tp}$, and $E_{ts}$ if $E_{ip}$ and $E_{is}$ are assumed to be known. This system can be solved numerically. The equations for the reflected and transmitted electric fields can be separated into

$$\begin{pmatrix} E_{rp} \\ E_{rs} \end{pmatrix} = \begin{pmatrix} R_{pp} & R_{ps} \\ R_{sp} & R_{ss} \end{pmatrix} \begin{pmatrix} E_{ip} \\ E_{is} \end{pmatrix} \qquad \begin{pmatrix} E_{tp} \\ E_{ts} \end{pmatrix} = \begin{pmatrix} T_{pp} & T_{ps} \\ T_{sp} & T_{ss} \end{pmatrix} \begin{pmatrix} E_{ip} \\ E_{is} \end{pmatrix} \quad . \tag{3.14}$$

R and T are the reflection and transmission Jones matrices of the system. A more detailed description of the method can be found in [Azzam & Bashara 1977].

Recapitulating, with the 4x4 Berreman method the reflection and transmission Jones matrices of anisotropic stratified media can be calculated numerically. The ambient media are assumed to be isotropic and semi-infinite. This is a plane wave method, i.e., no lateral scattering is taken into account. The method gives very good results for real

stratified media. An application for three dimensional periodic media, which are assumed to be stratified, will be given in chapter 4, which deals with Bragg reflection of blue phase liquid crystals.
As a first application of the 4x4 Berreman method we shall treat the problem of the cholesteric filter design presented in 3.1.3.

### *3.1.2 PROPAGATION IN CHOLESTERIC LIQUID CRYSTALS*

Cholesteric liquid crystals (CLC) are liquid crystal materials in the cholesteric (or better: chiral nematic) phase, wherein the rod-like (uniaxial) molecules are arranged parallel in planes [de Gennes 1993]. The averaged molecular direction changes linearly from plane to plane so that the molecular structure forms an ideal helix. As a result of the helical director arrangement we get some unique and interesting optical properties, such a very strong optical rotatory power and selective reflection of circularly polarized light.
The optically important parameters of the CLC are the pitch p and the principal refractive indices $n_o$ (ordinary) and $n_e$ (extraordinary). Between planes at a distance p the molecule director makes a full turn of $2\pi$. The values for the pitch of the cholesteric liquid crystals are between 300 nm and 500 nm. For liquid crystal materials with $n_o < n_e$ Bragg reflection occurs in the wavelength range $n_o p < \lambda < n_e p$.
The dielectric tensor of an uniaxial liquid crystal in the principal local coordinate system is, following section 2.4

$$\varepsilon(z) = \begin{pmatrix} n_e^2 & 0 & 0 \\ 0 & n_o^2 & 0 \\ 0 & 0 & n_o^2 \end{pmatrix} \quad . \tag{3.15}$$

This assumption can be made for most of CLC media. For the CLC layer it is assumed that the optical axis of the molecule remains in the x-y plane but changes its orientation depending on the position z by the pitch p. Using (2.11) with $\theta = 0$ and $\phi = 2\pi z/p$, the dielectric tensor in the fixed laboratory system becomes

$$\boldsymbol{\varepsilon}(z) = \begin{pmatrix} \bar{\varepsilon} + \Delta\varepsilon\cos\frac{4\pi z}{p} & \Delta\varepsilon\sin\frac{4\pi z}{p} & 0 \\ \Delta\varepsilon\sin\frac{4\pi z}{p} & \bar{\varepsilon} - \Delta\varepsilon\cos\frac{4\pi z}{p} & 0 \\ 0 & 0 & n_o^2 \end{pmatrix} \quad , \tag{3.16}$$

with $\bar{\varepsilon} = 0.5\,(n_e^2 + n_o^2)$ and $\Delta\varepsilon = 0.5\,(n_e^2 - n_o^2)$. $\boldsymbol{\varepsilon}$ is a periodic function of z with a period of p/2. With (3.16) the equation for the propagation of plane waves along the helical axis

z can be established. This equation has two analytic solutions with elliptical polarizations [de Vries 1951]. Furthermore it can be shown that in the frequency gap $n_o p < \lambda < n_e p$ circularly polarized light is almost fully reflected if it is of the handedness of the cholesteric liquid crystal helix and it is transmitted if it is of the opposite handedness. The calculated reflectance as a function of the wavelength consists of a main peak with sharp cut-offs (the "stopband") and a series of so-called sidelobes (see left side of Fig. 3.3). The analytical solution for the reflectance exists only for normal incidence. The 4x4 Berreman algorithm offers a numerical solution also for oblique incidence and was developed originally for this situation [Berreman & Scheffer 1970]. The method presented in section 3.1 is an extension of this algorithm to arbitrarily varying anisotropic layers. It can be applied by employing the dielectric tensor (3.16) of the cholesteric liquid crystal in (3.8) in order to obtain the local differential propagation matrix of each layer. This procedure allows, contrary to the analytical solution, to calculate the light propagation in a cholesteric material with spatially varying optical parameters, i.e., varying pitch or refraction indices of the liquid crystal material along the helical axis. We will show in the next chapter why this can be useful.

### *3.1.3 APODIZATION OF CHOLESTERIC BRAGG FILTERS*

The selective reflection property of the CLC makes it appropriate to be a stopband filter. This is an optical device which reflects at the best 100% over a given spectral band and transmits 100% on each side of the reflected band. These filters are realized since many years by index matching structures, i.e. layers which consist of quarterwave stacks of alternating low and high index layers [Born & Wolf 1959]. This arrangement provides a stopband for a preferred wavelength region with sidelobes around the reflecting region. In order to suppress these undesired effects the index matching is amplitude modulated (or "apodized"). These sidelobe reduced interference filters are called "rugate" filters [Southwell 1989] and [Abu-Safia 1993].

Following the idea of apodization we designed a cholesteric Bragg filter with reduced sidelobes by modulating the extraordinary refraction index along the helical axis of the cholesteric liquid crystal.

The left side of Fig. 3.3 shows the typical reflected intensity of a CLC for circular polarized light of the same handedness as the material. The reflectance was simulated by the 4x4 Berreman method for an element thickness of 10 μm, a pitch of 350 nm and for the refraction indices $n_o = 1.5$ and $n_e = 1.7$. The CLC was numerically subdivided in 1000 layers.

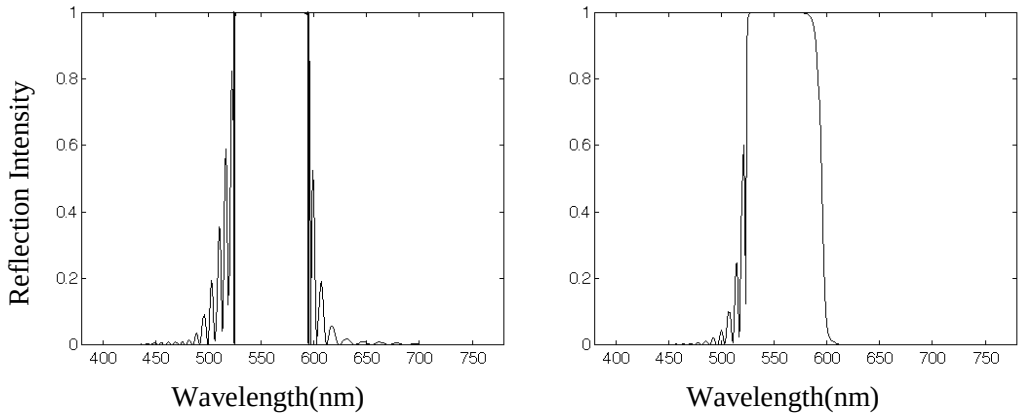


Fig. 3.3: Calculated reflection intensity vs. wavelength (nm) for a cholesteric liquid crystal; left: without apodization (the vertical lines mark the wavelengths with a reflection intensity of 90%); right: with optimized trapezoidal apodization function

The sidelobes of the reflected intensity are mostly suppressed for the apodized cholesteric liquid crystal (right side of Fig. 3.3) by the modification of the extraordinary refraction index between 1.5 and 1.7. We compared various types of apodization functions (trapezoidal and exponential). The ideal filter has a reflectance of 1 in the stopband and of 0 outside the stopband. In order to determine the quality of a stopband filter made of a CLC, we introduced the functions *FilterQuality* and *CurveQuality*. These functions depend on integral sums of reflections over the wavelength within certain bands. E90 is the integral of reflection over wavelengths between the wavelengths at the left and at the right side of the stopband for which the reflection is equal to 90% (see left side of Fig. 3.3). E10 and E50 are defined similarly. The difference between the wavelengths with 50% reflection is called halfwidth. The integrals of reflection over the wavelengths at the left and the right side of the stopband corresponding to E50 are called *Sidelobe1* and *Sidelobe2*, respectively.

We define

$$CurveQuality = \frac{E50}{E50 + Sidelobe1 + Sidelobe2} \qquad FilterQuality = \frac{E90}{E10} \quad . \qquad (3.17)$$

First we investigate trapezoidal apodizations and introduce the parameter *par* for determining the form of the apodization. *par* is equal to 0 for the triangular form and equal to 1 for the rectangular apodization form. *par* between 0 and 1 means a trapezoidal form. The maximal value of $n_e$ is 1.7 and $n_o$ remains 1.5 for all layers. The apodization functions for the extraordinary index and the corresponding curve and filter qualities are shown in Fig. 3.4.

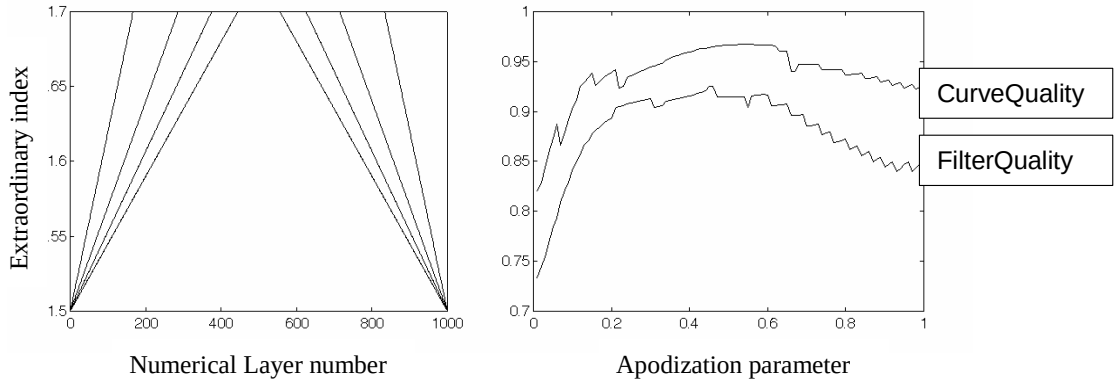


Fig. 3.4: Left: some trapezoidal apodization curves of the extraordinary refraction index vs. depth in terms of number of the numerical layers of the CLC. Right: *CurveQuality* and *FilterQuality* vs. apodization form parameter *par*

The form parameter *par* for exponential sinusoidal apodizations is defined by $n_e = n_o+0.2\sin(2\pi z/\text{thickness})^{par}$, z is the depth of the optical element, between 0 and thickness, $n_e$ is between 1.5 and 1.7, $n_o$ remains again equal to 1.5 for all layers. By that *par* = 0 means a pure sinusoidal apodization and *par* = 1 means a constant extraordinary index over the whole layer (the corresponding reflectance is shown on the left side of Fig. 3.3). Different exponential sinusoidal apodization forms and the corresponding *CurveQuality* and *FilterQuality* are shown in Fig. 3.5.

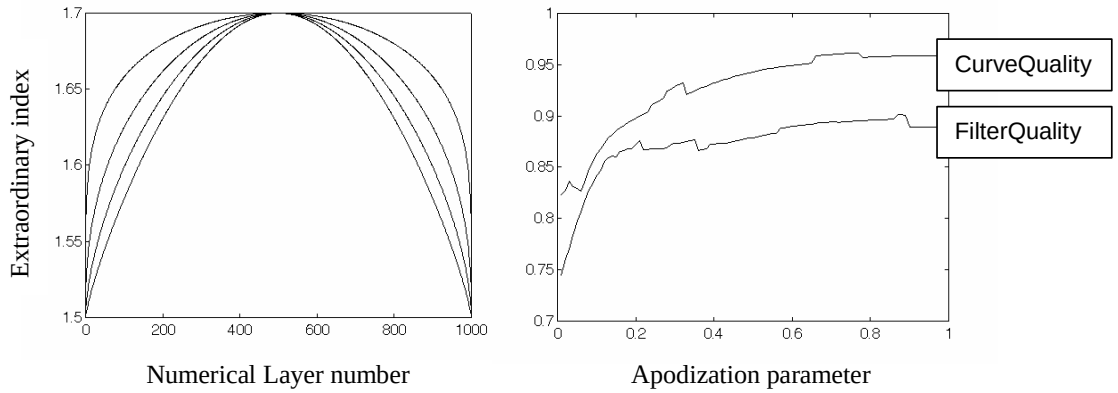


Fig. 3.5: Left: exponential sinusoidal apodization curves vs. depth in terms of number of the numerical layers of the CLC. Right: *CurveQuality* and *FilterQuality* vs. apodization form parameter *par*

The same material parameters as above were used and the CLC was again subdivided numerically in 1000 layers.

The maximal *FilterQuality* for trapezoidal apodizations (see Fig. 3.4) is 0.924 at *par* = 0.52. The best quality for exponential sinusoidal apodizations gives *par* = 0.88 with *FilterQuality* = 0.901. Maximal curve qualities are 0.97 for both groups of apodization.

The highest filter and curve quality is obtained for trapezoidal apodization and the correspondent reflectance is shown on the right side of Fig. 3.3.
All calculations were made using the 4x4 Berreman method assuming isotropic ambient media with a refraction index of 1.5. The layer matrix (in 3.10) was approximated up to the 3rd order.

### *3.1.4 COLOR OF THE LIGHT REFLECTED BY CHOLESTERIC LIQUID CRYSTALS*

Because of their selective reflection and bistability properties, CLCs are also of interest for reflective display applications. Reflective displays are suitable for portable information systems because of their low power consumption. Using three CLC cells providing different colors a controllable display based on additive color mixture is feasible [Wu & Yang 2001]. In order to verify the available color space of this display type it is important to determine the chromaticities and luminances of the three basic colors red, green and blue, produced by the CLC.
All following reflected intensities are calculated for circularly polarized light of the handedness of the CLC material. The determination of chromaticities and luminances is based on the assumption of an identical light source and the colormatching functions of the CIE 1931 Standard Colorimetric System, a special area model for the description of colors [Yeh & Gu 1999]. The chromaticities are defined by the values x,y corresponding to this standard.
For the calculations of the reflectance the 4x4 Berreman method was used.

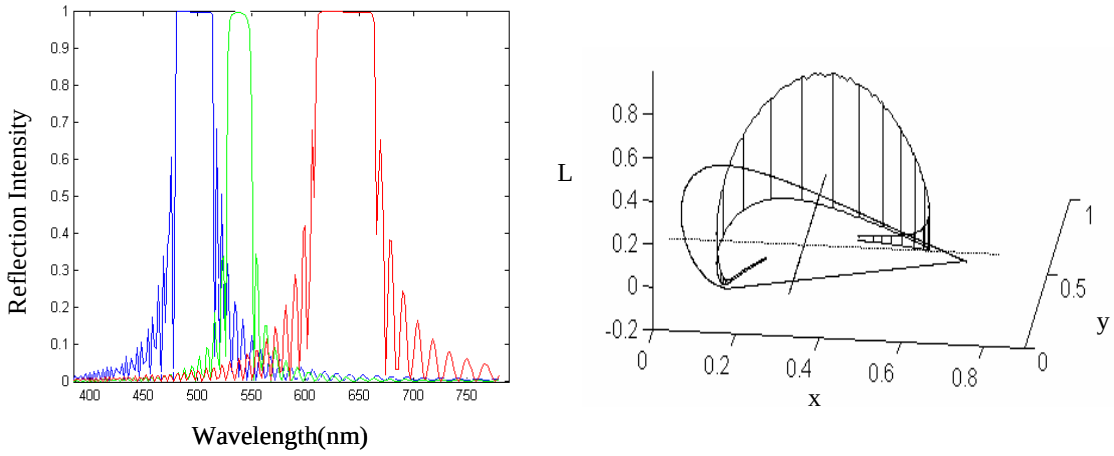


Fig. 3.6: Left: Reflection spectra of blue, red, green CLC vs. wavelength. Right: luminance L vs. chromaticity of cholesteric liquid crystals with pitches between 200 and 500 nm. The refractive indices are $n_o = 1.5$, $n_e = 1.8$. The CIE 1931 colorsystem diagram lays in the plane of luminance = 0

The left side of Fig. 3.6 shows the reflection spectra of single CLCs for a blue, a green and a red reflecting cell. Each of these reflectance spectra has a luminance of 20%. The product of the birefringence and the pitch determines the width of the reflection spectra. The refractive indices times the pitch give the wavelength positions of the reflection band.

For the design of CLC cells of maximal luminance and best colors it is not sufficient to vary the pitch but it is also necessary to take into account different refractive indices. The reflection luminances of single CLCs for constant refraction indices of $n_o = 1.5$ and $n_e = 1.8$ and for a pitch between 200 nm and 500 nm are illustrated on the right side of Fig. 3.6. The luminance L is presented on the axis in the third dimension over the chromaticity plane x-y. Read from this figure, for instance a maximal luminance of 0.79 in circular polarized light can be reached with a pitch of 343 nm, i.e. for gold color. The red and blue corner regions are represented only by reflection spectra delivering very low luminances below 0.05.

The applicability of a display that is based on color mixture depends on the luminance of the CLC-provided basic colors and of the colorspace covered by them. The curves in Fig. 3.7 are isoluminances of CLCs which are optimized to have a maximal luminance for a given chromaticity if the pitch is allowed to be between 200 and 500 nm and the extraordinary index $n_e$ between 1.55 and 1.8, while the ordinary refraction index remains at $n_o = 1.5$.

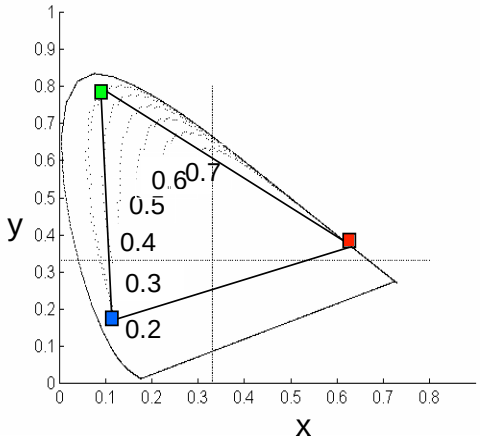


Fig. 3.7: Maximal isoluminances vs. chromaticity of cholesteric liquid crystals with pitches between 200 and 500 nm and extraordinary refraction indices $n_e$ between 1.55 und 1.8. Isoluminance lines are drawn for luminances of 0.2, 0.3, .. , 0.7

The squares in Fig. 3.7 indicate the chromaticity coordinates for the three CLC reflection spectra of Fig. 3.6 left. The available colorspace is the triangle spread by the single basic chromaticities.

### *3.1.5 REFLECTION BY POLYMER-DISPERSED CLC*

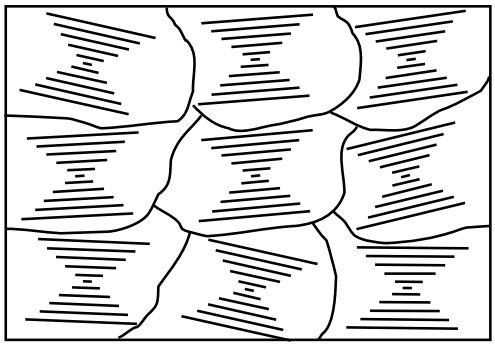

Fig. 3.8: Simple model of a multi-domain polymer-dispersed LC layer, also called "gel"

For reasons of stability in the mentioned display devices, mixtures of liquid crystals and polymers are used. If a small amount of polymer is dispersed in the LC, the system will be divided into domains, which are bound by thin polymer borders [Drzaic 1995] as shown schematically in Fig. 3.8. The cholesteric texture LC display assumes different stable states. We consider three states, which appear in the following order if an electric field is applied: planar state (reflection), focal conic state (forward scattering), and uniformly lying state (transmission) [Yeh & Gu 1999]. This is shown schematically in Fig. 3.9. In case of the planar textures, the LC molecules

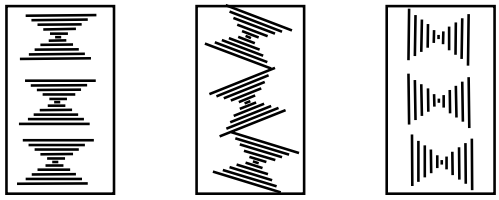


Fig. 3.9: The three main states of helix orientation. The transition between these states can be simulated by changing the two parameters 1. middle helix orientation and 2. helix orientation SD.

are parallel to the surface of the cell and the incident light is selectively reflected by the system. In focal conic textures the orientation of the helical axes is assumed to be randomly distributed, but centered perpendicular to the substrate surfaces. In case of the uniformly lying state, the helix axes lie parallel to the substrate and no reflection occurs.

In the focal conic state the reflection depends on the distribution of the helical axis orientation and the internal structure of the multi-domain texture.

In this chapter we will describe the properties (intensity, chromaticity and depolarization) of the light reflected by these multi-domain structured CLCs. The investigations will be made using a statistical approach which is based on the 4x4 matrix method. We consider an inhomogeneous random material with the help of a quasi-three-dimensional raytrace method.

Taking into account the domain structure of the focal conic textures of a cholesteric liquid crystal, one has to consider, in addition to the properties of the LC material,

parameters such as number and thickness of domains, the orientations of the helices inside the domains and the refractive index of the polymer that forms the borders of the domains. John et al. investigated the influence of pitch variations and helical axis orientation distribution on a cholesteric system by averaging the reflection spectra, neglecting the internal structure of the multi-domain texture, schematically shown on the left side of Fig. 3.10 [John et al. 1995]. We will call their approach the single-domain model.

The model applied here by us includes the refractive indices of the polymer and the CLC, the absorption coefficients of the CLC and the pitch of the helix, as well as the variations of the helical axis orientation and different domain sizes inside the liquid crystal cell (right side of Fig. 3.10). Our multi-domain model (that takes into account the domains), works as follows: one simulates the propagation of light through successive domains, while the orientation of the helix inside the domains is assumed to be normally distributed. Each domain is modeled as stratified medium according Fig. 3.2 and the Jones matrices of reflection and transmission are calculated for each domain with the 4x4 Berreman method (see section 3.1.1). The inclination of the domain borders with respect to the propagation direction is included by taking into account an angle of incidence ($\phi_0$ in Fig. 3.2). The Jones matrices of reflection and transmission for a column consisting of different domains are calculated by multiplication of the corresponding individual matrices.

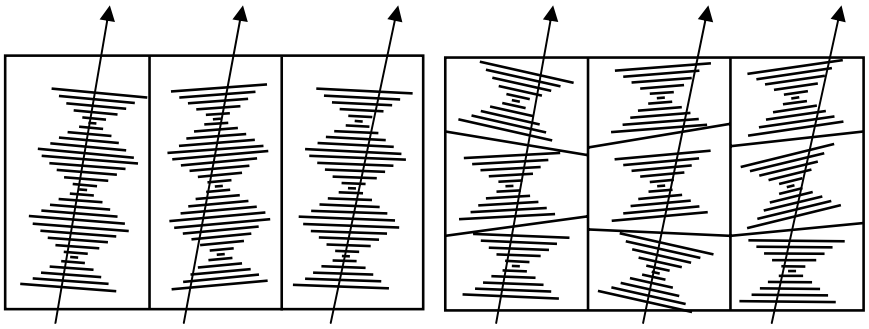

Fig. 3.10: Single-domain model (left): Light is going through various samples with different but uniform helix orientations
Multi-domain model (right): Light is going through different examples which are divided in different domains of different helix orientations

The reflection spectra of the columns are then calculated as averaged sum of a number of reflection spectra (non-coherent light) of randomly generated LC multi-domain sample structures (columns in Fig. 3.10) with statistically normal distributed helix orientations and domain sizes. As a measure for the distribution we have taken the variance respectively the correspondent standard deviation (SD). This model will be called by us

multi-domain model. Testing this model in a previous investigation [Bohley et al. 2001], we obtained the predicted development of the reflection spectra by changing parameters like domain size, angle of incidence and birefringence. As an example, for an increasing angle of incidence a shift to shorter wavelengths is expected, which was proven by our simulations. Moreover, we investigated the influence of the number of the domains considered to show the differences of quality between the single and the multi-domain system.

For the following simulations we supposed a cholesteric layer with a thickness of 5 µm, subdivided into domains of variable thickness and variable orientations of the helical axis. As material parameters of CLC we assumed $n_o$ = 1.516-0.004i, $n_e$ = 1.744-0.006i, pitch = 331 nm.

Refraction indices with a small imaginary part were used in order to accelerate the convergence for the summation within our statistical approach. We observed that a small imaginary part does not influence the single reflection spectrum significantly, but the statistical summation of these spectra converges much faster.

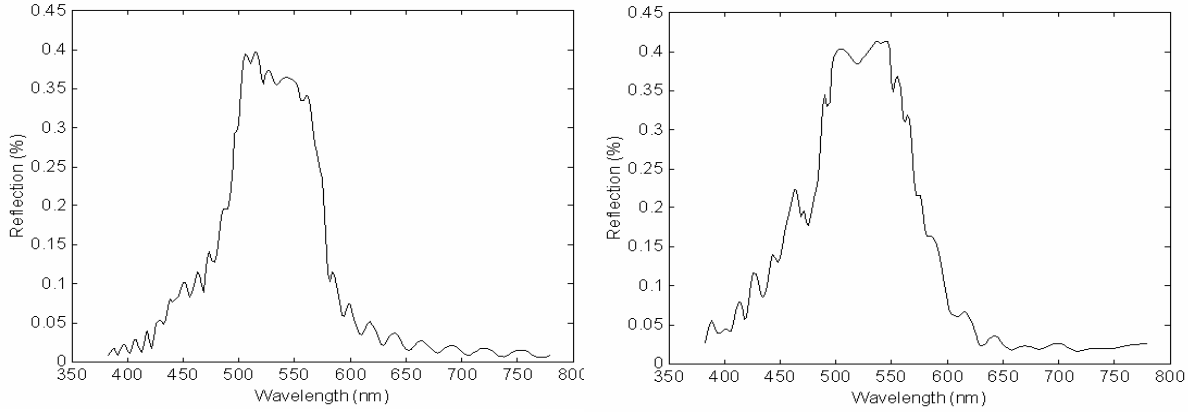


Fig. 3.11: Simulated reflection spectra of a single-domain (left) and multi-domain structured (right) CLC with a SD of 10° for the helix orientation and for linear polarized light at normal incidence

Nevertheless, the method can also take into account absorptive materials, for instance dye-doped LC materials. We will make use of this feature in chapter 4.

Figure 3.11 shows the Bragg reflection spectra of a single-domain layer (left side) without any subdivision and a domain structure subdivided into 10 domains (right side).

The orientation of the helical axes is normally distributed with SD = 10°. For the linearly polarized light normal incidence is assumed. For the multi-domain structure, the reflection spectra become wider. The maximum reflection wavelength and the maximum reflectivity remain the same for both models. The main difference between the single-domain and the multi-domain model becomes evident for larger angles of incidence and larger distributions of the helical axis. Figure 3.12 shows simulations for oblique

incidence at 35°. Both reflection spectra, for the single-domain and the multi-domain model, are shifted to shorter wavelengths. For the multi-domain structure the reflectivity is about 15% higher and the width at half height becomes larger.

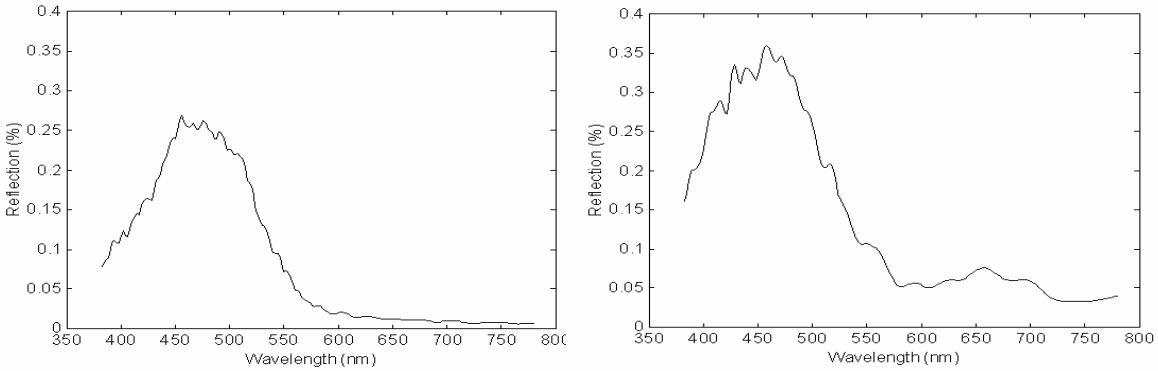


Fig. 3.12: Simulated reflection spectra of a single-domain (left) and multi-domain structured (right) CLC with a SD of the helix orientation of SD = 10° for oblique incidence and for linear polarized light (35°)

To test our simulation model for different parameters, we performed calculations for different angles of incidence and different numbers of domains. For increasing angle of incidence a shift to shorter wavelengths is expected. This is illustrated on the left side of Fig. 3.13 for the multi-domain model with 10 subdomains. The distribution of the helical axis orientation has a standard deviation of SD = 5°. The shift of the center reflection wavelength is clearly visible. In addition, a broadening of the reflection band by a factor of two is observed.

The dependence of the simulated reflections on the domain size is shown on the right side of Fig. 3.13. The layer with a thickness of 5 µm is divided for the simulations in 1, 10 and 40 domains, the helix orientations have a SD of 10°. One notes a wider reflection band

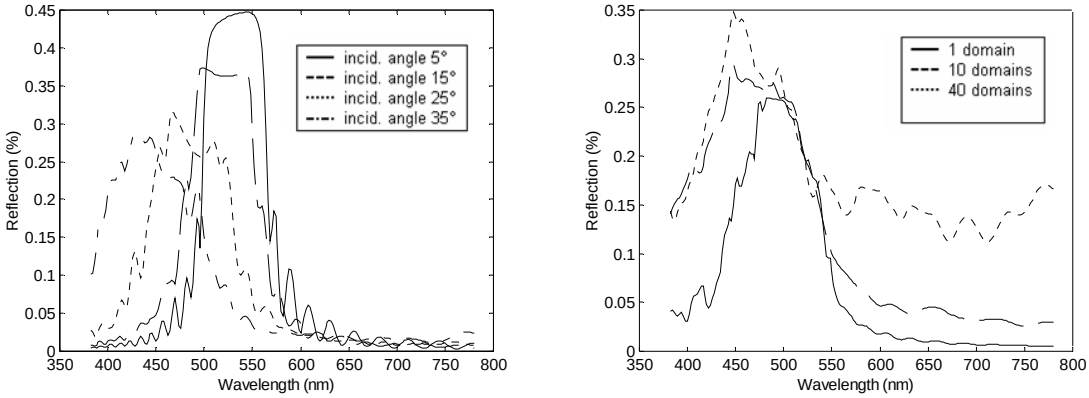


Fig. 3.13: Left side: Simulated reflection spectra of a 10-domain structured CLC for different angles of incidence. Right side: Simulated reflection spectra for multi-domain structured CLC systems with different numbers of domains (linear polarized light, oblique incidence under 30°)

and a change of the maximum reflectivity for increasing number of domains. All simulations were made for linear polarized light and by averaging 100 randomized examples.

To simulate the optical properties for different states of the multistable system (Fig. 3.9), the SD of the orientation of the helical axis can be used as a relevant parameter. This might give the possibility to associate the applied voltages to a helical axis distribution and the internal domain structure in the liquid crystal cell. We assumed a CLC with refractive index $n_o$ = 1.516-0.014i, $n_e$ = 1.744-0.018i, pitch = 331nm and thickness of 5µm. As parameters we used helix orientation SD values from 0° to 30°. The results for normal incidence are shown on the left side of Fig. 3.14. With increasing variance, the reflection spectra shift to shorter wavelengths, become wider and the maximum reflectivity decreases.

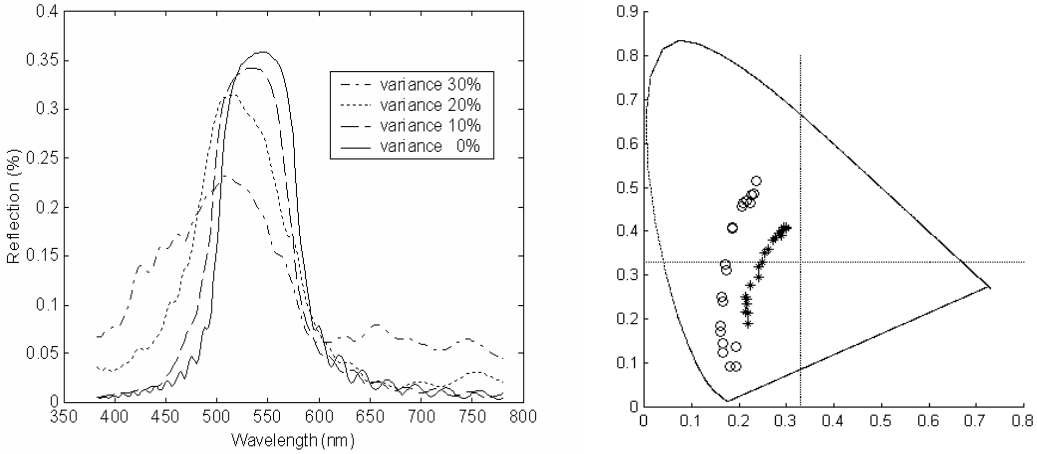


Fig. 3.14: Left side: Simulated reflection spectra of domain structured CLC with various helix orientation variances, normal incident linear polarized light; Right side: Chromaticities in CIE1931 of multi-domain CLC systems under viewing angles between 0° and 40°, single-domain method: o, multi-domain method: *

In order to compare the chromaticities of the averaged reflection curves, computed for the single- and the multi-domain structure, we have chosen an example with a large SD of 30° for the helix orientations. Because of the large variance, we averaged over more than 100 samples. As can be seen on the left side of Fig. 3.15, the colors are significantly different for the mono-domain and the multi-domain model. In general, a reduced color space for multi-domain calculations is observed. Colors change from green to blue by increasing the angle of incidence, corresponding to the shift to shorter reflection wavelengths.

An interesting point of discussion is the dependence of the color coordinates on the variance of the helical axis. The right side of Fig. 3.15 shows the chromaticities of three

CLCs with increasing variance of the helical axis orientation. We assumed refractive indices of $n_o$ = 1.516-0.014i and $n_e$ = 1.744-0.018i and calculated for three different pitches, 290 nm for blue, 331 nm for green and 400 nm for red. The helix orientation SD increases from zero to 45°. The chromaticity of the simulated reflections spectra moves into the direction of the white point of the color system (x = 0.33, y = 0.33). One observes only a small color change for the blue. This can be understood by the shift towards shorter wavelengths when the SD of the helix orientation is increased. The influence is small because the blue is already at the short wavelength side of the spectrum. For the green and the red color the behavior is more spectacular. The green color loses more or

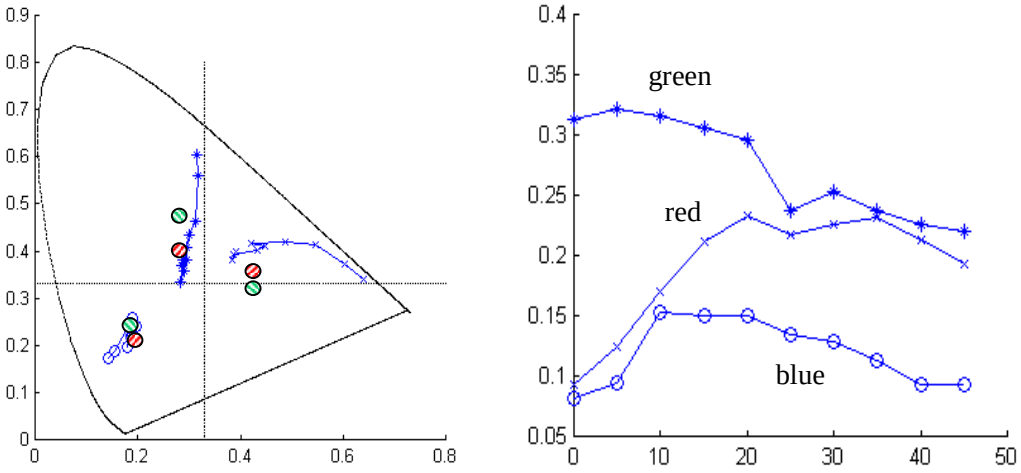


Fig. 3.15: Left: Chromaticities of 3 CLCs ($n_o$, $n_e$ as above; pitches 290 nm–blue–o, 331 nm–green-*; 400 nm–red–x; linear polarized light; normal incidence). The chromaticities go from the outer to the inner space with increasing variance of helix axis orientation
Right: Luminance vs. variance of helix axis distribution for 3 CLCs

less directly its brilliance and the color coordinates approach the white-point. The red color shifts at first towards yellow, because of the increasing intensity in the lower wavelength part of the spectra. After that, the white point is approached. It is instructive to see up to what extend the luminance of the different colors is changed for increasing variance of the helical axis distribution. The development of the luminances is shown on the right side of Fig. 3.14. The luminance of the green color is always decreasing, the blue does not change significantly and for the red it is increasing. The left side of Fig. 3.14 contains also information of experimentally obtained color spaces by different groups ([Davis et al. 1998] ⊘ and [Hashimoto et al. 1998] ⊘). For blue and green the experimentally found colors correspond well with the multi-domain model. The calculated color coordinates for the red color do not fit the experimental findings. These

might be due to dye in the red liquid crystal mixture or to different liquid crystal parameters.
Concluding, we did simulate the reflection of light from polymer-dispersed cholesteric liquid crystals, taking into account the domain structured profile of the layer. The necessity of this new, physically more realistic model, is especially evident for larger viewing angles. We did develop a model, based on the 4x4 Berreman matrix method, which considers the different orientations of the helical axes in the individual domains. The distribution of the helical axis can be correlated with the structural profile of focal conic textures, which changes with the applied voltage (electric field) to the display cell. The model shows the expected behavior if parameters like domain size, the angle of incidence or the birefringence are changed. On the other hand, the difficulties to create a large color-space using three CLC cells for the basic colors became more evident.

### *3.1.6 DEPOLARIZATION EFFECTS FOR REFLECTION BY POLYMER DISPERSED CHOLESTERIC LIQUID CRYSTALS*

As shown in the previous section (3.1.5), the light reflected by polymer dispersed CLC is composed of many plane light waves of different intensities and polarizations. In order to investigate the polarization properties of the complete reflected light, we use the concept of the Stokes column, as described in section 2.4.2. The Berreman method delivers plane wave descriptions in Jones vector representation and these can be transformed into the Stokes column representations by (2.14). Extending this formula to a number of n plane waves and adding the individual contributions of the corresponding Stokes elements, we get the description of the actually observed incoherent light. The corresponding degree of polarization of the incoherent light represented by this Stokes column can be computed after [Gerrard & Burch 1975].
In detail: the Berreman method applied to the polymer-dispersed CLC layer delivers the reflected light in the form of n Jones vectors

$$\begin{pmatrix} E_{xi} \\ E_{yi} \end{pmatrix} = \begin{pmatrix} E_{x0i} \\ E_{y0i}\cos\Delta_i \end{pmatrix} \qquad i = 1...n \qquad , \tag{3.17}$$

which are different, because of the propagation through different zones of the domain structured layer. These Jones vectors were obtained by means of the multi-domain method described in 3.1.5.
Applying (2.17) and the principle of incoherent superposition of individual Stokes vectors, we get

$$\mathbf{S} = \begin{pmatrix} S_0 \\ S_1 \\ S_2 \\ S_3 \end{pmatrix} = \begin{pmatrix} \sum_{i=1}^{n} E_{x0i}{}^2 + E_{y0i}{}^2 \\ \sum_{i=1}^{n} E_{x0i}{}^2 - E_{y0i}{}^2 \\ \sum_{i=1}^{n} 2E_{x0i}E_{y0i}\cos\Delta_i \\ \sum_{i=1}^{n} 2E_{x0i}E_{y0i}\sin\Delta_i \end{pmatrix} \tag{3.18}$$

for the reflected light in Stokes column representation. The degree of polarization can now be calculated from (2.19).

In order to represent the polarization of the n contributions, we use the Poincaré sphere (Fig. 2.4). The modulus of the Jones vector corresponds to the intensity of the individual contributions $S_{0i}$ and is represented in the Poincaré space by the distance of the points from the center of the sphere. This way of representation is very useful here because it allows us to show the polarization states and intensities of the light at the same time. (Natural light would be presented by an uniform distribution of states on and inside the Poincaré sphere, light of single linear polarization would be presented by one point on the equator). Figure 3.16 shows Poincaré spheres with a radius of 1 in stereo representation with intensity-weighted polarization states of 50 examples of reflection. The material is a 10-domain-structured CLC with a thickness of 10 µm, refraction indices $n_o$ = 1.516, $n_e$ = 1.744, pitch = 331 nm. The incident light is linearly polarized (of intensity 2) and is represented by the point marked with + at the left side of the equator of the spheres. Increasing the standard deviation SD of the helix orientation causes a larger distribution. of the polarization states and a shift of the states towards the center, because of the decreasing intensity of the reflection. This explains the decreasing degree of polarization when moving from the planar state to the focal conic state (Fig. 3.9), as measured by Khan et al. [Khan et al. 2001].

Using (2.16) we are able to look at the development of the degree of polarization for different SDs of the helix axis orientation in a multi-domain structured liquid crystal. Figure 3.17 shows the degree of polarization and the intensity of light for a wavelength of 520 nm reflected by a CLC vs. the SD of the helix orientation. The difference between the results obtained by the multi-domain method (10 domains) and by the single-domain method (1 domain) is shown. For larger SDs of helix orientation, the degree of polarizations tends not towards zero, because the state of completely disordered helix orientations has still a finite degree of polarization. Note that the state of completely disordered helix orientations can be reached by increasing the SD of the helix orientation starting from the planar or from the uniformly lying state.

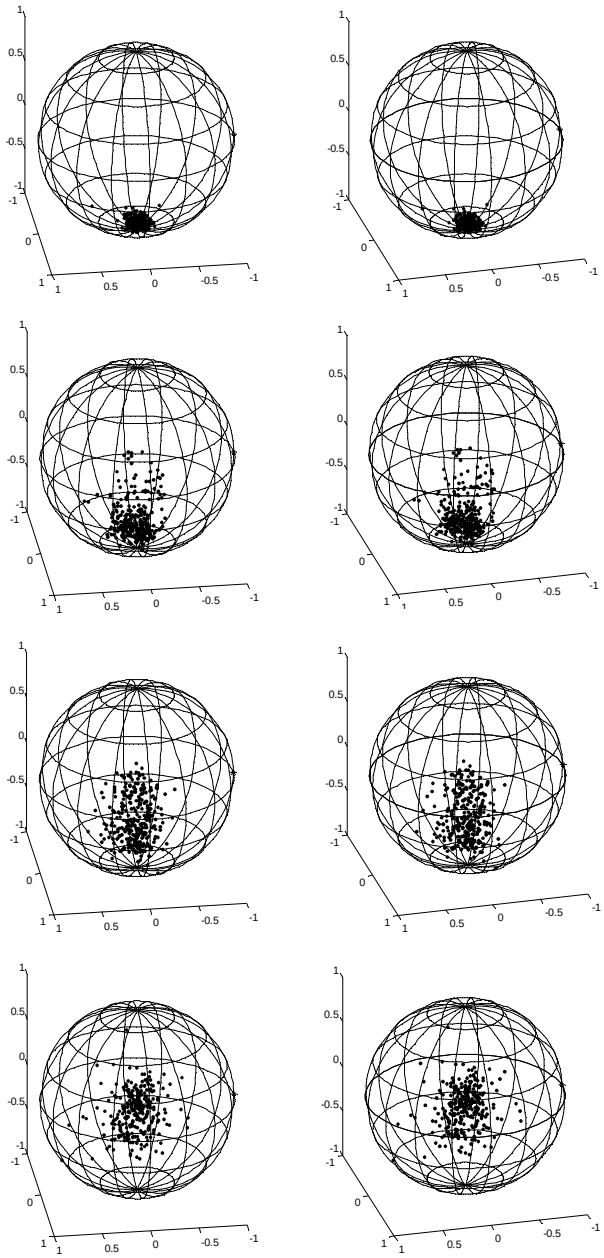

Fig. 3.16: Poincaré sphere representation in stereo[1] with intensity-weighted polarizations of light which is reflected by a polymer-dispersed CLC, calculated with the multi-domain method for linear polarized light at normal incidence (wavelength 520 nm) and different standard deviations for the helix orientation. Top to bottom: SD = 0°, 20°, 40° and 60°

[1]Use the 3D free-viewing method, which is called cross-viewing or the cross-eyed method. You aim your eyes so that the lines of sight of your eyes cross in front of the image.

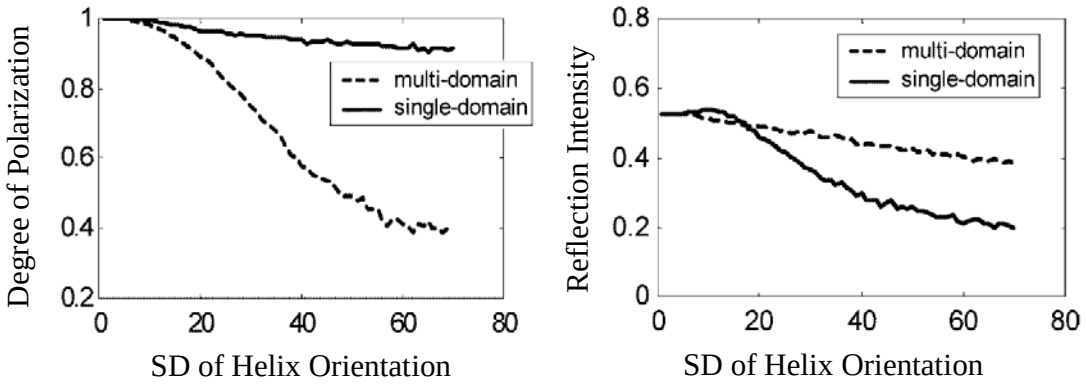


Fig. 3.17: Degree of polarization (left) and intensity (right) of light reflected by a CLC vs. helix orientation SD (°) for a wavelength of 520 nm, simulated for multi- and single-domain structured systems. The input light is linearly polarized and of normal incidence.

Again it is seen that the multi-domain model gives a smaller degree of polarization than the single domain model and is therefore in better agreement with experimental results [Khan et al. 2001]. On the other hand, the single-domain model predicts a larger decrease of the reflected intensity than the multi-domain model.

### *3.1.7 STACKED SYSTEMS OF POLYMER-DISPERSED CHOLESTERIC LIQUID CRYSTALS*

In practice, most reflective displays are designed as matrices of controllable basic color cells that lie in a common plane [Yeh & Gu 1999] and [Wu & Yang 2001]. If the basic cells (blue, green and red) consist of CLC material a stacked design can be used, i.e. the three basic color cells, which control one pixel are arranged one behind the other. This is possible because the circular polarized light of same handedness as the CLC material outside the selective wavelength region is fully transmitted by each cell. Using the multi-domain method we investigated the state and degree of polarization of the light that is reflected and transmitted by stacked CLC systems. Considering the question of different combinations of the handedness of 3 stacked CLC cells (red-green-blue) we compared two constellations. First: the 3 cells have the same handedness (+++). Second: the two outer cells have the same handedness and the inner cell has the opposite handedness (+–+). The spectra of the light passing through these 2 constellations are different and the intensities of the +–+ constellation are higher, as it is observed in experiments. The reason is that single CLC cells reflect the parts of the incident light, which is circular polarized with the same handedness as the CLC director helix. The parts, which are circular polarized with the opposite handedness are transmitted for all wavelengths.

Therefore, the +–+ constellation has a better power budget. This is obvious for the perfectly aligned single-domain CLC display.

For multi-domain CLC systems the advantage is not so clear, because of the depolarization effects described in section 3.1.6. In order to investigate this problem we have computed the reflection spectra of the two stacked CLC systems +++ and +–+ (Fig. 3.18). Comparing the spectra in the case of SD = 0° (planar textures – reflection state), it is noticed that differences in the reflection spectra mainly appear in the regions between the edges of the reflection bands of the single cells. For a larger SD of the helix orientation the spectra differ more. Surprisingly, the intensity is about twice as high as for the +–+ configuration, compared with the +++ configuration, which was not expected at all.

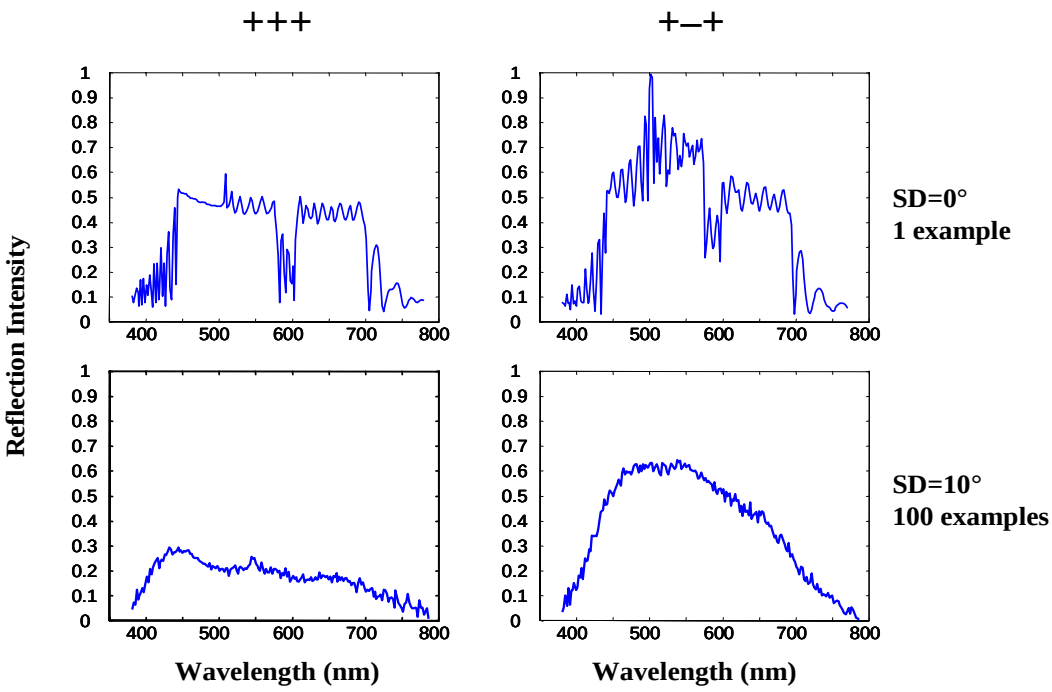


Fig. 3.18: Reflection spectra of the two different stacked CLC systems in “white” configuration (thickness 3x5µm) with different SD of the helix orientation. 10 domains, linear polarized light, normal incidence. LC materials of the single cells have the same refractive indices as above and pitches of 290, 331, 400 nm.

This effect appears not only for the “white” state (all cells in full reflection) but also for “color states” where the single basic cells are only partially switched. The “color states” correspond to different SDs of the helix orientation, produced by different voltages applied at the cells, (as described in section 3.1.5). Here we model the transition from the planar state to focal conic states for a multi-domain CLC by increasing the SD of the helix orientation up to SD = 90°, which describes the state of the total disordered helix

orientations. From this state we go to the uniformly lying state by decreasing the SD of the helix orientation but keeping the average helix orientation parallel to the CLC layer. Following this sequence we simulate a complete transition from the planar through the focal conic to the uniformly lying state, as it happens when the applied voltage is increased. By this way, changing the "control" parameters (average helix orientation and SD of the helix orientation) we are able to reproduce the spectra for the different "color

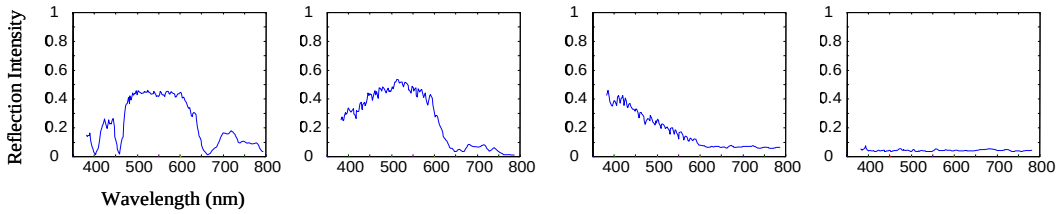


Fig. 3.19: Transition from green to black for a single multi-domained CLC cell, caused by the transition from the planar to the uniformly lying state; refraction indices like above, pitch 331nm, cell thickness 10µm

states" for a single CLC display. Fig. 3.19 shows the simulated transition from green to black for a green polymer dispersed CLC cell. While the intensity decreases, the reflection color goes from green over blue-green to white. With the knowledge of the reflected color for different helix orientation states of each basic cell, an exact controlling of the reflective display colors can be obtained.

### *3.1.8 CONCLUSIONS*

The 4x4 Berreman method has been described and applied to different problems. Assuming a homogeneous CLC material, we studied an optimized filter design by apodization for the reflection color behaviour. The polymer dispersed CLC as nonhomogeneous material has been investigated with a new statistical approach. We developped a multi-domain model that takes into account the domain structure of the focal conic state of the CLC. We considered the reflection behaviour for different states of statistical order and different angles of incidence. The multi-domain model makes it possible to quantify the depolarization of the reflected light in the focal conic state. As a result, the behaviour of stacked display cells for different stack arrangements can be explained.

The 4x4 Berreman method, extended by a statistical approach, turns out to be a fast and reliable tool to study the light propagation through anisotropic stratified or quasi-stratified media.

## 3.2 SPACE-GRID TIME-DOMAIN TECHNIQUES

Assuming an arbitrary anisotropic, inhomogeneous medium with a known dielectric tensor, matrix methods (like the Berreman 4x4 matrix method, see section 3.1) are no longer applicable to the general case. Because no simplification of Maxwell's partial differential equation system is feasible, it is necessary to revert to Maxwell's equations in their original form.

This was done the first time before 1960 in order to solve antenna and radar problems. For the simulation of the wave propagation in such electromagnetic engineering systems principal approaches involving closed-form and infinite-series analytical solutions were developed. These techniques solve the steady-state Maxwell equations in a simplified way. After about 1960, numerical methods, the so-called "frequency domain approaches", became more sophisticated due to the rise of computational speed, storage capacity and high-level programming languages. The initial computational approaches included high-frequency asymptotic methods [Keller 1962] and the discretization of integral equations [Harrington 1968]. The application of these methods is limited to simply structured materials.

Because of these limitations, it was looked for an alternative, which was found in the 70s: a space-grid time-domain technique. The principal idea of this technique is to solve directly the Maxwell equations over a time-domain on spatial lattices. The basic algorithm of a space-grid time-domain technique was first introduced by Yee in 1966, which gave the fundament for the finite-difference time-domain (FDTD) method [Yee 1966]. After providing the correct numerical stability criterion for the Yee algorithm [Taflove & Brodwin 1975a], the FDTD method was applied to electromagnetic pulse problems [Kunz & Lee 1978] and, furthermore, sinusoidal steady-state solutions of two- and three-dimensional electromagnetic wave interactions with structured materials [Taflove & Brodwin 1975b] were found. An important step to complete the availability of the FDTD method was the introduction of numerically stable absorbing boundary conditions (ABC) for the Yee grid. In their first form they were published by Mur in second-order accuracy [Mur 1981]. Kriegsmann et al. worked out an ABC theory [Kriegsmann 1987] and Berenger introduced the highly effective perfectly matched layer (PML) for two-dimensional FDTD grids [Berenger 1994]. These were enhanced for physically realizable, uniaxial anisotropic PMLs [Sacks et al. 1995, Gedney 1996]. In the meantime, the FDTD method was applied to a multitude of electromagnetic problems like microwave amplifiers, cellular telephones, optical microdisk resonators and photonic bandgap microcavity lasers [Taflove 2000].

Space-grid time-domain techniques are based on a volumetric sampling of the electric and magnetic fields and on a sampling over a time period. Because the space sampling

has to have subwavelength resolution (typically 10-20 samples per wavelength) the discretization will be very extensive for small wavelengths like the optical ones. Furthermore, if the field values at some distance are desired, it is likely that this distance will force the computational domain to be excessively large. Far field extensions are available for the FDTD method, but require some amount of post processing.
This great disadvantage is gradually overridden by the technical development of the computer processors and storage capacities. Up to now, acceptable (relating to the effort) FDTD calculations of the wave propagation in large spatial domains are limited to two-dimensional problems. The FDTD method has a very high accuracy convergence, depending on the sampling resolution. Moreover, the FDTD method is very instructive because the electric and magnetic field arrays are calculated at every time step and can be simultaneously visualized to illustrate the field dynamics.
The next section will describe the FDTD method in more detail. We will use the algorithm described above, but extended here for the interaction with anisotropic materials. Recent investigations of liquid crystal materials in application of the FDTD method can be found in e.g. [Witzigmann et al. 1998], [Kriezis &Elston 1999] and [Titus et al. 1999]. Recently, Kriezis studied the scattering from liquid crystal droplets [Kriezis 2002].
In 3.2.2-3 we will apply the FDTD method to investigate the interaction of light with nematic liquid crystal materials in special configurations.

### *3.2.1 DESCRIPTION OF THE FDTD METHOD*

The FDTD method is a direct method for the solution of the Maxwell curl equations

$$\nabla \times \mathbf{E} = -\mu_0 \mu \frac{\partial \mathbf{H}}{\partial t} \quad , \quad \nabla \times \mathbf{H} = \varepsilon_0 \boldsymbol{\varepsilon} \frac{\partial \mathbf{E}}{\partial t} \quad , \tag{3.19}$$

as it was introduced in section 2.1. First, the simulation domain will be discretized at subwavelength resolution. The time evolution of the electromagnetic fields is then computed by means of an explicit iterative updating scheme. So, the discretization happens in time *and* space dimension. The most used FDTD formulations are based on the Yee grid [Yee 1966]. This describes two ranked Cartesian space meshes on whose points the electric respectively magnetic field components are alternatively updated in a simple second-order accurate scheme, referred to as leapfrog scheme (see Fig. 3.20).
The components of the electric and magnetic fields E and H will be interpolated at the time points $t_n = n\Delta t$ and $t_{n+1/2} = (n+1/2)\Delta t$ (n is a positive integer), respectively, where the constant time step $\Delta t$ has to be chosen depending on the node distances and the refraction

index. In the discretized formulation of the partial differential Maxwell equations (3.19) the time derivations of the electric and magnetic field on a grid node can be approximated in the second order with the central difference equations

$$\frac{\delta}{\delta t} E_{i,n+1/2} = \frac{E_{i,n+1} - E_{i,n}}{\Delta t} \quad , \qquad \frac{\delta}{\delta t} H_{i,n} = \frac{H_{i,n+1/2} - H_{i,n-1/2}}{\Delta t} \quad , \tag{3.20}$$

where i stands for the indices x, y and z. Note, that the electric fields are updated at the "integer" time points and the magnetic fields at the "half" time points.

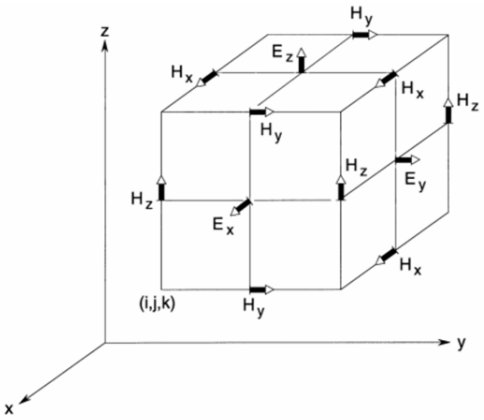


Fig. 3.20 : Primary and secondary grid in the Yee scheme concept (figure from [Yee 1966])

The spatial grid system (Fig. 3.20) can be thought as consisting of a primary integer grid for the actualization of the electric field components and a secondary grid for the actualization of the magnetic fields. The nodes of the secondary grid are at the centers of the primary cells formed by the primary grid vertices. This construction of the two staggered grids is adapted to the spatial central difference equations (3.20). Imagine the grid as a three dimensional chessboard on whose black areas lay the nodes for the computation of the electric fields and on whose white areas the nodes on which the magnetic field will be computed.

The discretization of the equation which yields the time derivative of the electric field in the Maxwell equations (3.19) will be made with

$$\begin{pmatrix} E_{x,\,n+1} \\ E_{y,\,n+1} \\ E_{z,\,n+1} \end{pmatrix} = \begin{pmatrix} E_{x,\,n} \\ E_{y,\,n} \\ E_{z,\,n} \end{pmatrix} + \frac{\varepsilon^{-1}}{\varepsilon_0} \Delta t \begin{pmatrix} \dfrac{H_{z,n+1/2}(y_0 + \Delta y/2) - H_{z,n+1/2}}{\Delta y} - \dfrac{H_{y,n+1/2}(z_0 + \Delta z/2) - H_{y,n+1/2}}{\Delta z} \\ \dfrac{H_{x,n+1/2}(z_0 + \Delta z/2) - H_{x,n+1/2}}{\Delta z} - \dfrac{H_{z,n+1/2}(x_0 + \Delta x/2) - H_{z,n+1/2}}{\Delta x} \\ \dfrac{H_{y,n+1/2}(x_0 + \Delta x/2) - H_{y,n+1/2}}{\Delta x} - \dfrac{H_{x,n+1/2}(y_0 + \Delta y/2) - H_{x,n+1/2}}{\Delta y} \end{pmatrix} \quad , \tag{3.21}$$

where $\boldsymbol{\varepsilon}^{-1}$ is the local inverse dielectric tensor, and $x_0$, $y_0$, $z_0$ indicate the current central grid point. The dielectric tensor $\boldsymbol{\varepsilon}$ may be locally different, representing a structured material. The discretization steps in the directions x, y and z are $\Delta x$, $\Delta y$ and $\Delta z$, which are at the same time the side lengths of the lattice primary cells. All field vectors depend on the time step number and the three spatial coordinates x, y and z. In our notation, the spatial arguments are not explicitly mentioned for reasons of simplicity. The electric fields lie on the primary grid nodes, therefore we mean $E_{x,n} = E_{x,n}(x_0,y_0,z_0)$ and e.g. $E_{x,n}(y_0+\Delta y) = E_{x,n}(x_0,y_0+\Delta y,z_0)$. The magnetic fields lie on the secondary grid nodes. Therefore, we will understand $H_{x,n+1/2}$ as $H_{x,n+1/2}(x_0-\Delta x/2,\ y_0-\Delta y/2,\ z_0-\Delta z/2)$ and e.g. $H_{x,n+1/2}(y_0+\Delta y/2)$ as $H_{x,n+1/2}(x_0-\Delta x/2,\ y_0+\Delta y/2,\ z_0-\Delta z/2)$.
The magnetic fields will be updated by

$$\begin{pmatrix} H_{x,\,n+1/2} \\ H_{y,\,n+1/2} \\ H_{z,\,n+1/2} \end{pmatrix} = \begin{pmatrix} H_{x,\,n-1/2} \\ H_{y,\,n-1/2} \\ H_{z,\,n-1/2} \end{pmatrix} + \frac{\Delta t}{\mu_0} \begin{pmatrix} \dfrac{E_{y,n}(z_0+\Delta z)-E_{y,n}}{\Delta z} - \dfrac{E_{z,n}(y_0+\Delta y)-E_{z,n}}{\Delta y} \\ \dfrac{E_{z,n}(x_0+\Delta x)-E_{z,n}}{\Delta x} - \dfrac{E_{x,n}(z_0+\Delta z)-E_{x,n}}{\Delta z} \\ \dfrac{E_{x,n}(y_0+\Delta y)-E_{x,n}}{\Delta y} - \dfrac{E_{y,n}(x_0+\Delta x)-E_{y,n}}{\Delta x} \end{pmatrix}, \qquad (3.22)$$

where we use the same notation as in (3.21). Here, the material is assumed as nonmagnetic ($\mu = 1$).
The algorithm, which associates the updating of the electric (3.21) and the magnetic (3.22) fields is commonly called the leapfrog time-marching scheme: Starting from initial values of the electric and magnetic fields on all nodes of the lattice, the electric field values will be updated by (3.21), corresponding to a time step of $\Delta t/2$. The next time step (again $\Delta t/2$) will update the magnetic fields with (3.22), using the previous magnetic fields and the electric fields that were computed directly before. After that, (3.21) will be used again for the updating of the electric fields and so on.
Note, that all updates of the electric (3.21) and magnetic (3.22) fields are made at the same time points *for the whole lattice*.
Applying this time updating scheme from the Maxwell equations, the local material parameters have to be known. That means at every grid point in the primary and secondary grid the dielectric tensor has to be defined. The FDTD can be also generalized to materials of arbitrary conductivity and magnetic permeability, but here we restrict the problem to non-conductive and non-magnetic media.
Usually the spatial steps $\Delta x$, $\Delta y$ and $\Delta z$ are equal (the primary cell is then a cube) but in special cases different discretization steps can be advantageous, e.g. if a material has a rapidly changing anisotropy in only one direction. Then the space sampling in this direction has to have a higher resolution than in the other directions. Generally,

anisotropic materials require a sampling resolution of about 20 per wavelength while a sampling of 10 per wavelength is sufficient for isotropic materials.
The time advancing updating bases on the condition that the discretization scheme is conditionally stable. In order to ensure that, the time step $\Delta t$ fits to the spatial grid; we have to choose $\Delta t < \Delta t_{max}$, where $\Delta t_{max}$ is the propagation time of the wave with the velocity $c_0/n$ along the spatial step $\Delta x$. n is the minimal refraction index of the medium and $c_0$ is the light velocity in vacuum. By this way we obtain $\Delta t_{max} = n\Delta x/c_0$ as necessary condition. Taflove gave for a three dimensional isotropic cubic grid the condition

$$\Delta t_{max} = \frac{n\Delta x}{c_0\sqrt{3}} \tag{3.23}$$

for numerical stability [Taflove 2000].
Since surrounding components are required for the computation of the fields, the described scheme can not be applied at the outermost lattice planes of the simulation grid. Consequently, special updating schemes were developed for the outer grid boundaries. For periodic structures the computation domain can be truncated by applying periodic boundary conditions. This means that in the discretization that the field values required in (3.21) and (3.22) outside a border will be taken from the spatially antipodal border, but from the corresponding nodes inside the lattice.
Non-periodic finite structures have to be simulated by the use of absorbing boundary conditions (ABC) and for this reason the border domains are parts with a sufficiently low level of reflection.
The idea of the Mur boundary condition is the modification of the discretized Maxwell equations in the truncated domains. The central difference equations (3.21) and (3.22) are replaced by so-called one-way wave equations. The normal derivatives in the update equation are here replaced by derivatives with respect to tangential directions [Mur 1981].
Nowadays, most often ABCs are used, which are based on the construction of artificial absorbing media in the truncated border domains. The advantage of this idea is that the truncation can be made with orders of magnitude lower errors than employing one-way wave equations. The truncation border domains are filled virtually with a special anisotropic material for which it can be shown that a plane wave incident from vacuum with an arbitrary wave vector is transmitted without reflection. This phenomenon is referred to as perfect matching. For sufficiently thick layers the transmitted wave will be exponentially decaying within the truncating medium if the uniaxial material has major axis elements in the diagonal of the dielectric tensor, which have an imaginary part larger than zero [Ziolkowski 1997]. The so-called perfectly matched layers (PMLs) were

introduced by Berenger for isotropic materials [Berenger 1997] and later extended to domains of anisotropic materials [Peréz et al. 1998].
A last word to the wave sources: the FDTD is free concerning the definition of source conditions, that means, e.g. an arbitrary light source can be initiated by a simple addition of a constant electric or magnetic field value in the right side of (3.21) respectively (3.22) at each time step at the desired source region. Usually, point, line or Gaussian beam sources are used corresponding to the simulation requirements. A more sophisticated way for a plane wave source definition is to use a domain boundary as source region. This can be done by the total-field/scattered-field formulation, which separates the domain into a scattering and a total field region. The scattering field region contains the material (or scattering) domain and the total field region is free of scatterers. If the electric and magnetic field values are updated at the total-field/scattering-field boundary, both total field and scattered field quantities appear in the second term on the right side of (3.21) and (3.22). In this formulation it is the virtual interface between the total and the scattered field region, which serves as generator of the incident wave. For details and discussion of this method the reader is referred to [Mur 1981] and [Umashankar & Taflove 1982].

### *3.2.2 NEMATIC LIQUID CRYSTAL CAPILLARIES*

In this section the FDTD method will be applied to a special confined liquid crystal problem. We will study the light propagation through nematic liquid crystal capillaries. These tubular geometries are not only of structural interest but also interesting for nonlinear optics applications [Khoo 1988]. In more recent publications induced self waveguiding structures in dye doped nematic liquid crystals were investigated. The liquid crystal material is confined in fiber size capillaries and one analyzes the interaction with a source beam which is self focused by the liquid crystal in the capillary. Different aspects like focusing, multi focus regime, filamentation and undulation are of interest [Warenghem & Henninot 1998].
Here we will focus on the interaction of a plane wave with the cross-section of a nematic

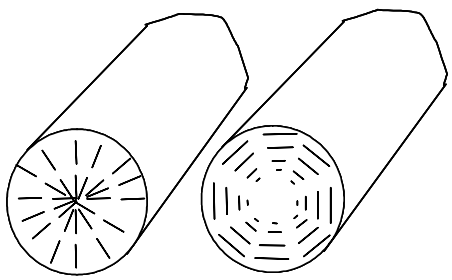

Fig. 3.21 : Liquid crystal filled capillaries of radial (left) and concentric (right) configuration

liquid crystal capillary. Depending on the anchoring and the type of the nematic liquid crystal material different configurations inside the capillary are possible. Figure 3.21 shows two capillaries with radial and concentric configuration respectively. We will investigate the near- and far-field of the light diffracted by the anisotropic capillaries of different structural type (radial, concentric and bipolar). By reasons of symmetry these capillaries have identical cross sections along the capillary axis. Therefore, we can reduce the problem to a two-dimensional one: to the propagation of a plane wave in a cross-section plane.

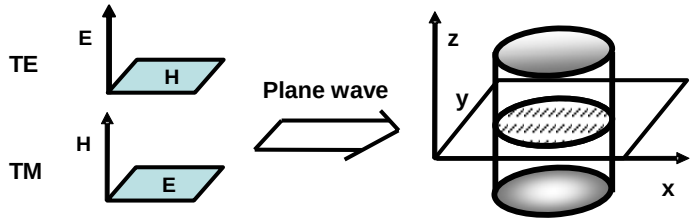


Fig. 3.22: A plane wave enters the capillary cross-section; geometry and polarization definitions for the two dimensional problem

The directors of the liquid crystal molecules lie for all considered capillary types in the cross-section plane. So, the situation is like described in 2.2 and the TE and TM polarizations can be considered separately (see the geometry of our case in Fig. 3.22). The TE polarization corresponds to a simple case, because the cross-section domain is "seen" as isotropic by the electric field due to uniaxial anisotropy of the liquid crystal material. So we will concentrate our studies to TM polarized plane waves.
Note, that for the application of the FDTD algorithm to the TM-polarization the formulae (3.21) and (3.22) are reduced to

$$\begin{pmatrix} E_{x,\,n+1} \\ E_{y,\,n+1} \end{pmatrix} = \begin{pmatrix} E_{x,\,n} \\ E_{y,\,n} \end{pmatrix} + \frac{\boldsymbol{\varepsilon}^{-1}}{\varepsilon_0} \Delta t \begin{pmatrix} \dfrac{H_{z,n+1/2}(y_0 + \Delta y/2) - H_{z,n+1/2}}{\Delta y} \\ -\dfrac{H_{z,n+1/2}(x_0 + \Delta x/2) - H_{z,n+1/2}}{\Delta x} \end{pmatrix} \tag{3.24}$$

and

$$H_{z,\,n+1/2} = H_{z,\,n-1/2} + \frac{\Delta t}{\mu_0}\left( \frac{E_{x,n}(y_0 + \Delta y) - E_{x,n}}{\Delta y} - \frac{E_{y,n}(x_0 + \Delta x) - E_{y,n}}{\Delta x} \right) \quad . \tag{3.25}$$

First, we will give reasons for the necessity of taking into account the anisotropy of the material. For a TM polarized plane wave passing a capillary of radial or concentric configuration (Fig. 3.28) we did calculate the diffracted light using the FDTD method in assuming the material inside the capillary as isotropic. Therefore, the dielectric tensor $\boldsymbol{\varepsilon}$ in

(3.24) and (3.25) is scalar (but locally variant) and equal to $n_{eff}^2$, where $n_{eff}$ is the refractive index of the molecule director "seen" from the propagation direction of the entering plane wave (that means in our simulations: coming from the left side). Formula (3.26) gives the simplified effective refractive index n for the liquid crystal material with the ordinary refractive ordinary index $n_o$, the extraordinary index $n_e$ and the angle $\theta$ between the propagation direction and the x-axis of the assumed index ellipsoid.

$$n_{eff} = \frac{n_o n_e}{\sqrt{n_o^2 \sin^2\theta + n_e^2 \cos^2\theta}} \qquad (3.26)$$

Using this simplification of the problem we neglect the anisotropy of the material. How the results are falsified by this simplification is shown by the direct comparison with the rigorous FDTD simulations, which take into consideration the anisotropy of the material. These are shown in the right side of Fig. 3.23 for capillaries of radial and concentric configurations. The plane wave enters from the left side and its wavelength is 400 nm. Fig. 3.23 shows the calculated intensities of the TM polarized wave propagating through the LC filled capillary, which has a radius of 1 µm. The refractive indices of the anisotropic material are $n_o = 1.5$ and $n_e = 1.8$. The refractive index outside the capillary is $n = 1.0$.

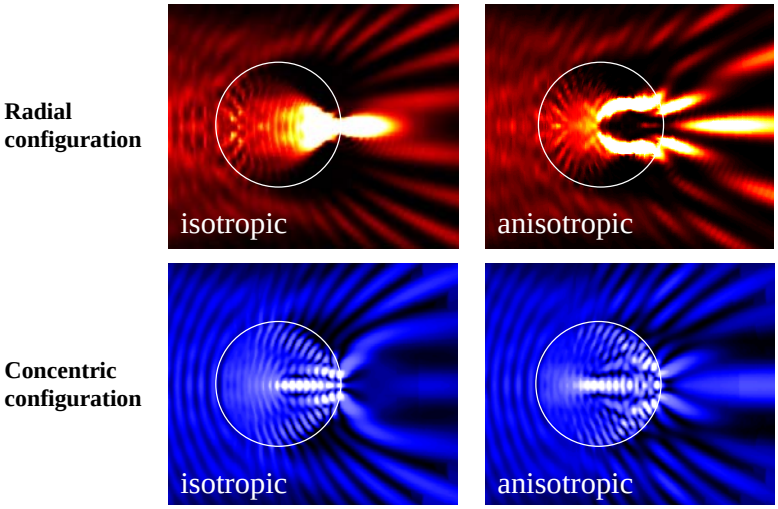


Fig. 3.23: Calculated intensities for TM polarized light propagating through a LC filled capillary of radial and concentric configuration with a radius of 1µm, $\lambda = 400$ nm. Left: assumed as isotropic but inhomogeneous ($n_{eff}$ "seen" from the propagation direction). Right: anisotropic with $n_o = 1.5$ and $n_e = 1.8$. Surrounding $n = 1.0$, size of the simulation domain 4.0 µm x 6.2 µm.

The significantly different distributions of the intensity for the anisotropic and the isotropic capillaries, in particular for the radial configuration, emphasize the necessity of

taking into account the anisotropy of the material. An approach, which considers anisotropy, but is based on geometrical optics, was applied by Reyes to radial and bipolar configurations [Reyes 1998] (see also [Zumer 1988]). Kriezis compared the FDTD method with a raytrace approximation for nematic LC droplets [Kriezis 2002].
All results shown in the following are calculated with rigorous FDTD simulations for TM polarized light. Fig. 3.24 shows the calculated intensity and phase distributions in an area around the capillary and the nearfield intensities 800 nm behind the capillary in the direction of propagation for different capillary configurations. The radius of the capillary is 2λ. The wavelength is equal to λ = 550 nm. The ordinary and extraordinary refractive indices of the liquid crystal material are assumed as $n_o$ = 1.5 and $n_e$ = 1.8. The refractive index outside the capillary is n = $n_o$ =1.5. Because of the higher refractive index of the ambient medium, which was adapted to the liquid crystal material, we do not have strong

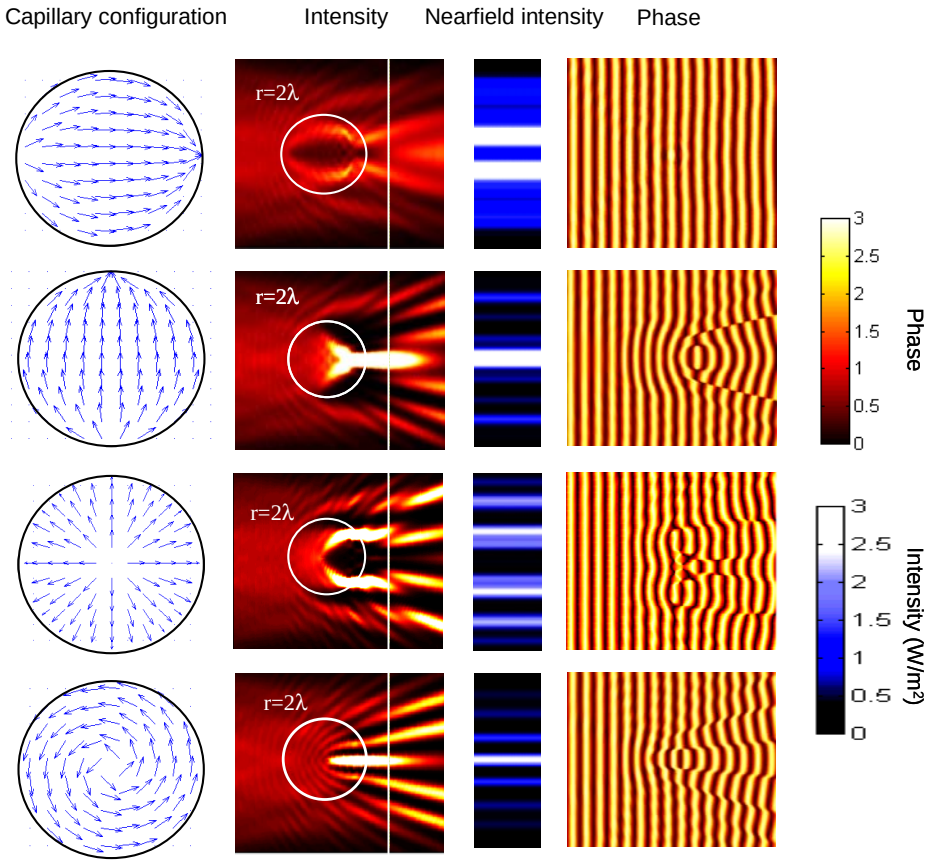


Fig. 3.24: From left to right: Director configuration in the LC capillary, intensity (time-averaged length of the Poynting vector) (W/m$^2$) (area 4.5 x 5.6 µm), nearfield intensity (W/m$^2$) on the white line vs. distance, phase of magnetic field (rad); λ = 550 nm. The TM-polarized plane wave comes from left, $n_o$ = 1.5, $n_e$ = 1.8, environment n = 1.5. The capillary configuration from top to bottom are: bipolar(1), bipolar(2), radial and concentric

reflection at the capillary as in the case of n = 1.0 shown in Fig. 3.23.

The simulations in Fig. 3.24 underline the significant dependence of the diffraction effects on the anisotropic structure inside the capillary. The capillary of bipolar configuration with the average direction of the director parallel to the incident light wave (first row in Fig. 3.24) has almost no influence on the phase field of the entering TM polarized light. But the bipolar configuration perpendicular to the incident light wave (second row in Fig. 3.24) shows an optical behavior, which is similar to that of a cylindrical isotropic lens.

The effects of the radially and concentricly configured anisotropic capillaries (3rd and 4th row in Fig. 3.24) are more surprising. Already the nearfield intensity distributions show a larger dispersion of the light. The phase fields are more perturbed and the field behind the radial capillary is characterized by some significant phase singularities.

Concentrating on the radial configuration, we will now investigate the light diffraction by capillaries of different diameters filled with a nematic liquid crystal material in the radial configuration. Like above, we will calculate the intensity and phase distributions in the capillary and the surrounding area, the nearfield intensity directly behind the capillary (marked with a white perpendicular line in the intensity distribution images) and the farfield intensity. Again we use the FDTD method in two dimensions for TM

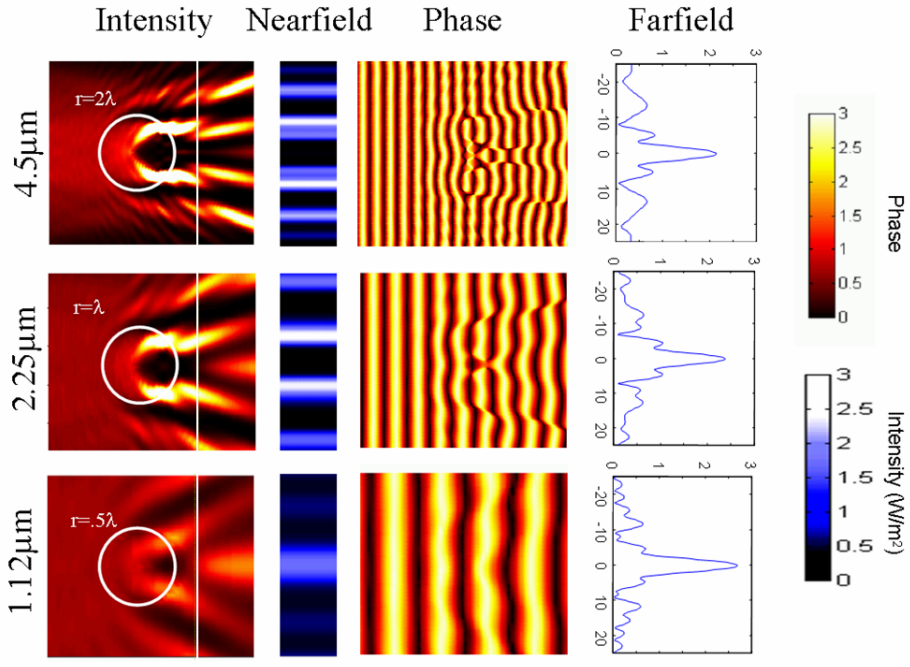


Fig. 3.25: Dispersion by the capillary of radial LC configuration and of different sizes. From left to right: intensity (time-averaged length of the Poynting vector) ($W/m^2$), nearfield intensity ($W/m^2$) on the white line vs. distance, phase of magnetic field (rad), farfield intensity vs. angle (°); $\lambda = 550$ nm, TM-polarization, $n_o = 1.5$, $n_e = 1.8$, environment n = 1.5.

polarization. The farfield is calculated with the Rayleigh-Sommerfeld approximation [Saleh &Teich 1991], using the complex amplitude on a line behind the capillary. Fig. 3.25 shows the simulation results. If the radius of the capillary is downsized, the perturbation to the phase-field is reduced and the farfield intensity will be more concentrated to the zero propagation order. Interestingly, the influence to the farfield is not as high as it could be assumed from the intensity distributions in the nearfield. Particularly, for the capillary of the radius $2\lambda$ the nearfield intensity is strongly diversified by the capillary but the farfield remains strongest in the direct straight propagation.

### *3.2.3 LIQUID CRYSTAL GRATINGS*

In this section we demonstrate the application of the FDTD method described in 3.3.1 to alignment patterned liquid crystal films where the alignment is planar and homeotropic for different domains. Using elastic theory the nematic director field can be analytically calculated with the method of conformal mapping.
Recently, liquid crystal displays with multi-domain alignment were developed [Titus et al. 1999]. They show interesting optical properties concerning viewing angle and polarization of light. Polarization insensitive spatial light modulators [Bos et al. 1995] have very high efficiencies when used as switchable gratings and beam deflectors. The light propagation through such anisotropic gradient refractive index system is not anymore easy to handle especially if the director configurations contain twist deformation. Here we want to discuss planar oriented liquid crystal director fields without any twist distortion. They serve as general model systems for anisotropic gradient index gratings. The alignment will be patterned with homeotropic and planar alignment under strong anchoring conditions. In that case an analytical model allows calculating the director profile in the “one constant approximation” and the light propagation can be simulated by different methods afterwards [Geurst et al. 1975, Vitek & Kléman 1957, Okana et al. 1994]. We use the Berreman matrix method [Berreman 1972] to compare the simulations made with a finite-difference time-domain method [Taflove & Hagness 2001]. The far field and the diffraction efficiencies are calculated. The diffraction properties of a periodic arrangement of such structures are explored by propagating the emerging light to the far field.

#### DIRECTOR FIELD

When two adjacent regions on a substrate surface of a nematic liquid crystal cell are subjected to different anchoring conditions, the boundary between the two regions

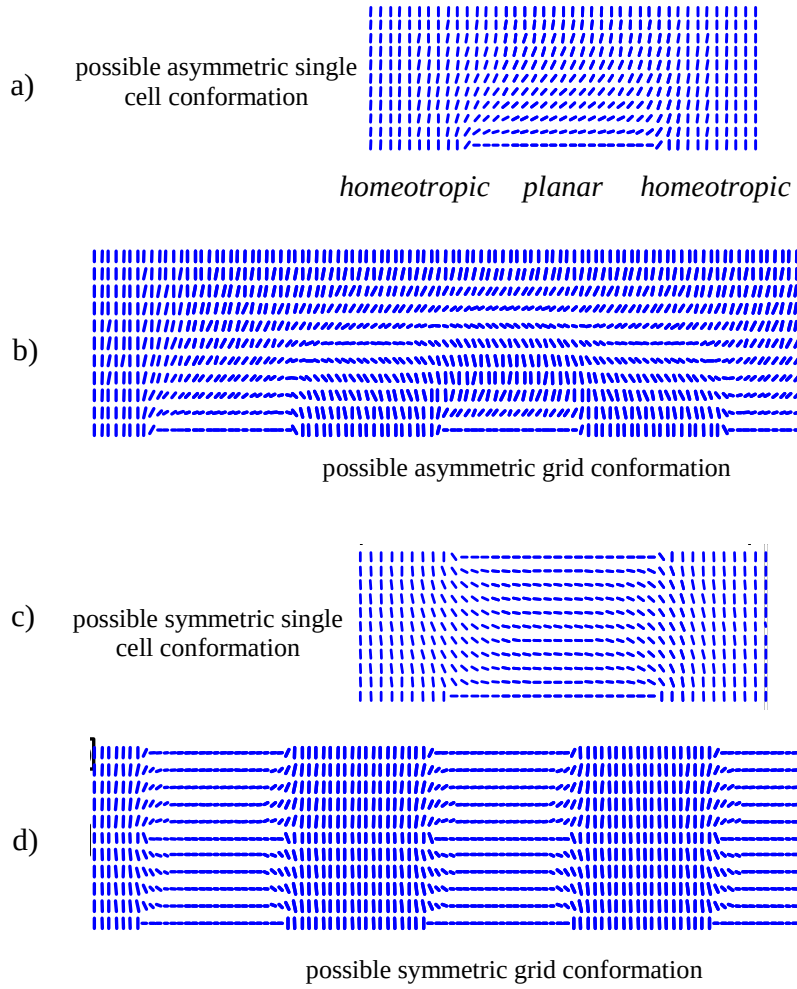


Fig. 3.26 : Possible LC director conformations for cells and grids with symmetric and asymmetric boundary conditions. The calculations were made with the conformal mapping method

constitutes a disclination line attached to the surface substrate, i.e. a surface disclination. Disclinations sticking at a solid-nematic interface also occur when the substrate is not flat or has sharp corners or edges. The director configurations around the surface disclinations associated with modified flat substrates can be analyzed using a function theory method [Okana et al. 1994]. In the following we assume that the director field is two-dimensional; the state of alignment in the liquid crystal cell depends only on the x and y coordinates, i.e. the director **n** is in the (x,y)-plane. We assume that the surface anchoring of the liquid crystal is always strong. Fig. 3.26 shows different LC cell structures, first as single cell conformation and then as grid cell. The single cell structure in Fig. 26a and the grid structure in Fig. 26b are asymmetric and the anchoring conditions change at the bottom of the cell between homeotropic and planar. The anchoring conditions of the structures Fig. 3.26c und Fig. 3.26d are symmetric and so are the corresponding grid

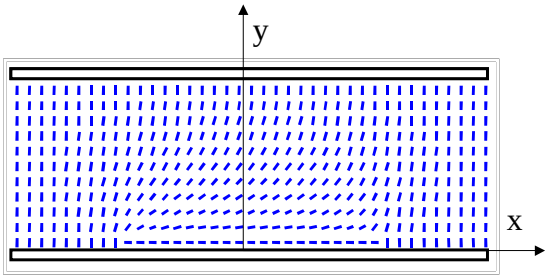


Fig. 3.27: Nematic director field for a liquid crystal cell of modified substrates with one alignment-patterned surface. The planar alignment is imposed on the lower substrate from $x = -a$ to $x = a$.

conformations. All shown structures are theoretically possible by energy considerations. Whether conformations appear in reality depends on the corresponding free energy of the distortion. In the following, we will present a director field calculation for a single asymmetric cell, made with the method of conformal mapping.

Consider a cell in which the liquid crystal is confined between two parallel-plane substrates at distance d. Let the x axis lie in the bottom substrate and the y axis perpendicular to that plane, as shown in Fig. 3.27. The director

$$\mathbf{n} = (\cos\phi, \sin\phi, 0) \tag{3.27}$$

is in the (x,y) plane and forms a tilt angle $\phi(x,y)$ with the x-axis. We impose the boundary conditions for the director so that we have on one substrate surface uniform alignment and on the other a modified substrate as shown in Fig. 3.27. The alignment conditions change from homeotropic to planar and from planar to homeotropic at positions $x = -a$ and $x = a$, respectively. In the "one constant approximation" [de Gennes 1993] the free energy F of the distortion is given by

$$F = \frac{1}{2} K \iint \left[ (\partial\phi/\partial x)^2 + (\partial\phi/\partial y)^2 \right] dx\,dy \quad , \tag{3.28}$$

where K is the elastic constant. The equilibrium configuration of the director, in which F is locally minimal, must satisfy the two-dimensional Laplace equation [Courant & Hilbert 1931]

$$\partial^2\phi/\partial x^2 + \partial^2\phi/\partial y^2 = 0 \ , \tag{3.29}$$

subjected to the boundary conditions. One now introduces a complex variable $z = x + iy$ and considers a regular function $\Phi$ in the complex z plane. Then the real and imaginary parts of $\Phi$ are harmonic functions satisfying the Laplace equation (3.29). Here we assume that the imaginary part of $\Phi$ satisfies the given boundary conditions. However, in general, it is not an easy task to determine the required regular function directly. Therefore one uses the method of conformal mapping (see for instance [Churchill 1960]). By means of a

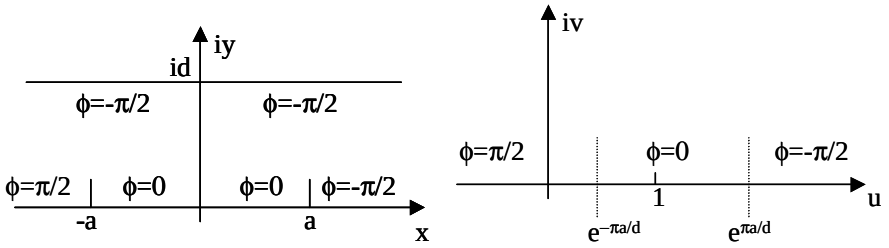


Fig. 3.28: The complex z- and w-plane with boundary conditions before and after conformal mapping.

suitable regular function $w = f(z) = u + iv$ one maps the domain $0 \le y \le d$ of the complex z-plane conformal onto the upper half of the complex w-plane. If we can find a regular function $\Psi(w)$ in the w-plane which satisfies the boundary condition in the w-plane than transforming back into the original z-plane we have the required solution $\varphi(x,y)$ of the boundary value problem as the imaginary part of $\Phi(z) = \Psi(f(z)) = \psi(x,y) + i\varphi(x,y)$, which maps the x-axis (y = 0) and the line y = d onto the u-axis, as shown in Fig. 3.28.

In the w-plane a regular function, whose imaginary part is compatible with the boundary conditions, is found to be

$$\Psi(w) = 1/2 \cdot \left(\log\left(w - e^{-\pi a/d}\right) - \log\left(e^{\pi a/d} - w\right)\right) \quad . \tag{3.30}$$

This is because the logarithm function for complex variables $\log(z) = \ln|z| + i\arg(z)$ changes the imaginary part from 0 to $\pi$ when changing the variable z from positive to negative values, i.e. $\mathrm{Im}(\log(-a)) = \pi$ and $\mathrm{Im}(\log(a)) = 0$ for a real and $a > 0$. The distinction between the director positions $\theta$ and $\theta \pm \pi$ is irrelevant for the tilt angle of the nematic liquid crystal director [de Gennes 1993]. Therefore there are different possibilities to create the boundary conditions and functions $\Psi(w)$ that fulfill these boundary conditions. Different director configurations are possible, where one is the energetically favourable. The configuration shown in Fig. 3.27 is the one with the lowest free energy [Geurst et al. 1975, Okano et al. 1994].

Backward transformation of the function $\Psi(w)$ gives

$$\Phi(z) = \Psi\left(e^{\pi z/d}\right) = 1/2 \cdot \left(\log\left(e^{\pi z/d} - e^{-\pi a/d}\right) - \log\left(e^{\pi a/d} - e^{\pi z/d}\right)\right) \quad . \tag{3.31}$$

After simplification, one finds finally the tilt angle profile $\phi(x,y)$ as the imaginary part of $\Phi(z)$ as

$$\varphi(z) = 1/2 \cdot \arctan\left(\frac{\sin(\pi y/d)\sinh(\pi a/d)}{\cos(\pi y/d)\cosh(\pi a/d) - \cosh(\pi x/d)}\right) \quad . \tag{3.32}$$

The model allows the extension to gratings with more than one period. Using Eq. (3.32) we are now able to calculate director configurations for arbitrary cell thicknesses and sizes of the alignment patterned structure.

## LIGHT PROPAGATION SIMULATION

Anisotropic gradient index media are difficult to handle with conventional light propagation simulation methods like ray tracing. In a previous study [Scharf 2000] it was found that the limit of spatial resolution of alignment-patterned gratings is given by the thickness of the liquid crystal layer. Experimental results and simulations proved that a simple Jones matrix calculation is not sufficient to understand the optical properties of such spatial resolution-limited gratings because of strong gradients in the refractive index distribution.

In order to investigate the propagation of light passing through a liquid crystalline structure of micrometer size we used the rigorous FDTD method presented in section 3.2.1. This allows the simulation of the time-dependent electric and magnetic fields for a region that is two-dimensional and possibly anisotropic. For the director profile described above in the previous chapter, the condition for which the problem can be separated in TE and TM polarizations is again fulfilled (see section 2.2). This is because the Maxwell equations for such a problem decouple for these two perpendicular linear polarizations.

Perfectly matched layer (PML) boundary conditions were used to avoid disturbing reflection from the borders of the simulation box. The FDTD method, in contrast to the methods of geometrical and matrix optics, delivers results which include diffraction and scattering. As an example, Fig. 3.29 shows an amplitude and phase distribution for TM polarization at a wavelength of 550 nm. The corresponding director profile is shown in Fig. 3.27. The spatial distribution of the birefringence causes a focalization of the intensity and the phase is modulated. The simulation box is 5.5 µm high and 6.875 µm

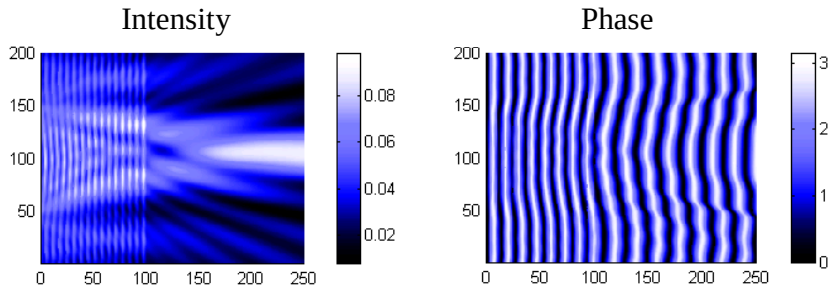


Fig. 3.29: Intensity and phase of light propagating through the structure shown in Fig. 3.27 ($2a = d = 2.75\ \mu m$, $\lambda = 550$ nm) with the FDTD anisotropic method; TM polarized light coming from the left (scales: number of layers in steps of 27.5 nm)

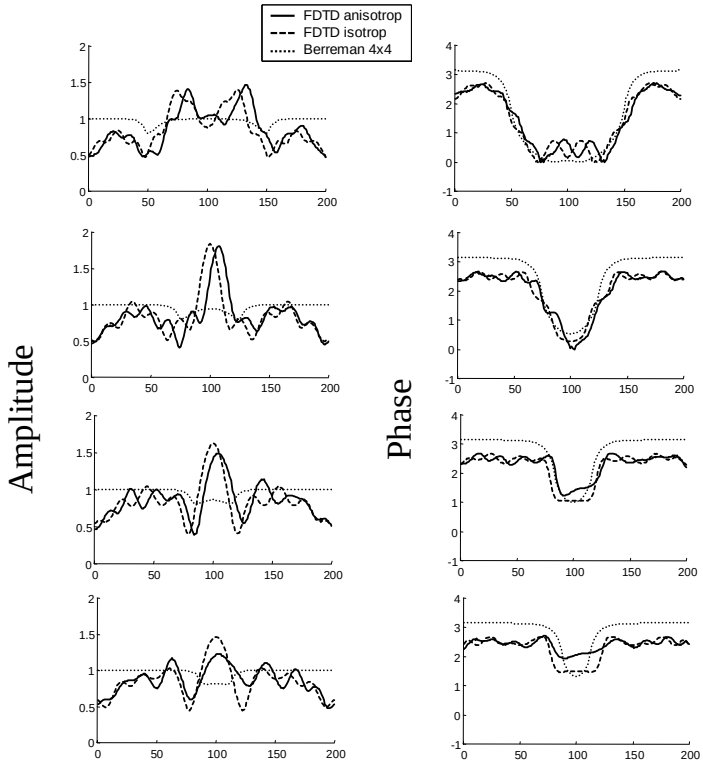


Fig. 3.30: Amplitude (left) and phase (right) at the LC structure exit for different pattern sizes and calculation methods. Alignment-pattern size from top to bottom: 2a = d, 0.5d to 0.25d with d = 2.75 µm. The graphs show the results for a 4x4 Berreman method, gradient index method with an effective index and the rigorous anisotropic simulations (horizontal scale: number of layers in steps of 27.5 nm)

wide with a discretization of 20 points per wavelength. The liquid crystal layer has a thickness of 2.75 µm and the regions inside and outside the liquid crystal are distinguished in the phase pattern by the smaller wavelength inside the liquid crystal.

To compare different optical simulation techniques, we calculated the amplitude and phase profiles at the exit of the liquid crystal structure with three different methods. The results are shown in Fig. 3.30 for three different pattern sizes. Since the director configuration has no twist distortion, the polarizations are separable. The amplitudes and phases in Fig. 3.30 are shown for incident linear polarization with the polarization direction lying in the x-y plane (TM). The rigorous simulations including anisotropy are compared with the Berreman matrix method and a rigorous simulation where the medium is assumed nonhomogeneous but isotropic (see also section 3.2.2). The refractive index gradient profile for the isotropic FDTD is found by calculating an effective refractive index for each point of discretization for the direction normal to the substrate surfaces. This is done with equation (3.26). The isotropic approach with the FDTD method allows

taking the gradient into account and their performance can be compared with advanced polarization ray tracing methods [Kosmopoulos & Zenginoglou 1987].
Comparing first the amplitude profiles in Fig. 3.30, one sees immediately remarkable differences in the amplitude distribution. For the Berreman Matrix method we get only a small modulation of the intensity, because for the Berreman matrix calculation the intensity modulation is only produced in the region of very strong distorted nematic director fields. The rigorous methods show amplitude variations of more than 50% due to the influence of the gradient in the birefringent distribution. Beside this, the Berreman method and the gradient index calculation without anisotropy give symmetric distributions of amplitude and phases. Only the rigorous FDTD method including anisotropy shows the expected asymmetry of the intensity and phase, caused by the asymmetry of the structure (Fig. 3.27). In general, the phase profiles differ not much and it can be concluded that the difference between the calculated light propagation models lies in the pronounced amplitude distribution.
The main criteria to characterize such structures if they are arranged in gratings are the diffraction efficiencies. For comparison, we calculated the diffraction efficiencies in the Fraunhofer approximation [Goodman 1996] by Fourier transforming the complex amplitudes shown in Fig. 3.30. It is clear that this can only give us an indication of the problem of the spatial resolution limit of liquid crystal alignment-patterned gratings because the director configuration for a single pixel of planar oriented liquid crystal and a grating of such structures will not be the same. Nevertheless, in good approximation we can accept this and we calculated the diffraction efficiencies for the different methods of the -2,-1,0,+1,+2 order. The results are shown in Table 3.1. Clearly, we see that already for a structure size comparable with the thickness of the liquid crystal layer the calculated efficiencies for the matrix method and the rigorous approach differ considerably. Having a look at the zero order intensity for the structure size equal to the thickness d we find for the anisotropic rigorous simulation an intensity in the zero order of $I^{A}_{0} = 0.6$. For the isotropic rigorous simulation the intensity in the zero order is $I^{I}_{0} = 0.59$ and for the Berreman matrix method we get an intensity of $I^{B}_{0} = 0.06$. The diffraction efficiency for the rigorous methods and the matrix method differs by one order of magnitude, which has been confirmed by experiments on twisted systems [Scharf 2000]. For smaller structure sizes, the difference is less pronounced because of the very small diffraction efficiencies due to smaller phase shifts. Remarkable effects coming up for very small structure sizes where the simulation results of all three models differ a lot. At a size structure of $d/8 = 5\lambda/8$ the asymmetry of diffraction efficiencies becomes large and the structure shows the behavior of a subwavelength grating. In general, the diffraction efficiencies calculated with the Berreman and the gradient index methods are too large and do not show the correct symmetry.

| Size | Method \ Diffraction order | -2 | -1 | 0 | +1 | +2 |
|---|---|---|---|---|---|---|
| d | Anisotropic | 0.0236 | 0.0785 | 0.6003 | 0.1163 | 0.0145 |
| | Isotropic | 0.0212 | 0.0998 | 0.5913 | 0.0996 | 0.0210 |
| | Berreman | 0.0295 | 0.3797 | 0.0553 | 0.3797 | 0.0295 |
| d/2 | Anisotropic | 0.0576 | 0.1104 | 0.5374 | 0.1313 | 0.0839 |
| | Isotropic | 0.0761 | 0.1255 | 0.5132 | 0.1257 | 0.0761 |
| | Berreman | 0.0745 | 0.1775 | 0.3961 | 0.1775 | 0.0745 |
| d/4 | Anisotropic | 0.0283 | 0.0347 | 0.7302 | 0.0432 | 0.0496 |
| | Isotropic | 0.0700 | 0.0725 | 0.5898 | 0.0724 | 0.0700 |
| | Berreman | 0.0492 | 0.0824 | 0.6289 | 0.0824 | 0.0492 |
| d/8 | Anisotropic | 0.0040 | 0.0126 | 0.8878 | 0.0162 | 0.0100 |
| | Isotropic | 0.0397 | 0.0416 | 0.7194 | 0.0416 | 0.0396 |
| | Berreman | 0.0302 | 0.0443 | 0.7554 | 0.0443 | 0.0302 |

Table 3.1: Diffraction efficiencies for different diffraction orders of alignment-patterned gratings. The structure size is given with respect to the thickness d = 2.75 μm of the liquid crystal layer. The wavelength is 550 nm. The numbers indicate the positive and negative diffraction orders.

### *3.2.4 CONCLUSIONS*

The FDTD as a rigorous space-grid time-domain technique was applied to confined LC problems. In the case of nematic LC capillaries we demonstrated the necessity of the use of a rigorous method taking into account the anisotropy in comparison with a simplified method that neglects the anisotropy of the medium. For the case of LC gratings we have shown that light propagation in such gradient index optical systems with anisotropy has to be handled also with a rigorous method for the simulation of light propagation. For a diffraction analysis of high-resolution liquid crystal gratings, where the resolution is given by the thickness of the liquid crystal cell, it is not sufficient at all to study a gradient index model or use an approach with the Berreman matrix method.

We calculated intensity, phase distribution and far-field behaviour of “soft” LC gratings with the rigorous FDTD method. A step further would be the study of light propagation through anisotropic gradient index media with twist structures. That is more complicated to handle, because three-dimensional rigorous calculations are required.

# 4 BLUE PHASES

This chapter treats Blue Phases as special cubic liquid crystal (LC) phases, which offer a selforganized natural model of a 3D photonic crystal. Blue Phases will be described and investigated theoretically and experimentally. The interaction of light with Blue Phases will be simulated by a 4x4 matrix algorithm like it was used in section 3.1 but extended to the application of anisotropic 3D systems. We calculated Müller matrices of the Bragg reflected light. The theoretical results will be compared with experimental observations. We will treat special cases, such as the effect of dyes in the LC material.

## 4.1 INTRODUCTION

Blue Phases (BP) are something special in the world of LC, because they are real "crystals" in the sense that there are translational symmetries in three independent directions. Nevertheless, like other LC phases, the molecules have mean equilibrium positions but only a certain degree of order. The crystal periodicity of the BP is on a scale of hundreds of nanometers and therefore Bragg reflection effects caused by the crystal occur at the wavelengths of the visible light. This leads to observation of effects in the optical and not in the X-ray domain where crystallography is practiced for crystals in molecular dimension.

BP are exhibited by chiral nematic (cholesteric) LC materials with a sufficiently short pitch. Because chiral nematic liquid crystals were originally made from cholesterol derivatives they are also called cholesterics. Optical properties of the helical phases of these materials were already investigated in the sections 3.1.2-7.

The BP, filled in a capillary, exhibit in reflection a strong scattering for blue light, like it is shown in a figure in [Demus & Richter 1978]. Nevertheless, the term "Blue Phases" is misleading, because platelets of this LC phase appear under the microscope also in other colors. This first detection of BP was made more than 100 years ago [Reinitzer 1888] together with the detection of the first liquid crystals at all. The understanding of BP has begun around 1970, as the general interest in liquid crystals lead to extensive investigations. In 1906 Lehmann observed BP as a metastable LC phase without birefringence in thin layers and supposed it to be a different type of LC and not only special textures of cholesterics [Lehmann 1906]. Saupe recognized the strong rotational power of the BPs and proposed a chiral cubic lattice structure because of the isotropy of the material [Saupe 1969]. Other structural models have been proposed, for instance the randomly oriented globules theory [Gray & Winsor 1974] and the modified helix structure model [Bergmann et al. 1979]. The model now established is the disclination

model [Meiboom et al. 1981], which suggests a three-dimensional lattice of linear defects with isotropic cores. So, the BP are understood as consisting of so-called double twist cylinders, which are arranged to form a cubic lattice in different ways.
The BP occur in three different phases as BPI, BPII and BPIII in a very small temperature range between the isotropic and the helical state. The BPI has a body centered cubic symmetry (bcc), the BPII is simple cubic (sc). Grebel et al. applied a Landau theory to the phase transitions of the chiral nematics and confirmed the body centered cubic nature of the BPI and the simple cubic symmetry of the BPII, but their theoretical phase diagram does not fit well with experimental data [Grebel et al. 1984]. The disappearing of the BPII for higher chiralities could not be explained by this theory and another predicted space group (interestingly the special cubic symmetry, which was proposed as first trial by Saupe [Saupe 1969]) could not be confirmed by experimental data. In contrast to BPI and BPII, the BPIII does not exhibit a cubic Bragg scattering and does not form single crystal platelets, but it is birefringent and optically active. The BPIII, which appears at the highest temperature, looks amorphous and was called “blue fog” [Marcus 1981]. The structure of the BPIII is not yet completely understood and still subject of discussion (see for instance [Crooker & Kitzerow 1992]). Electron micrographs of a freeze fractured BPIII let suppose a spaghetti-like disordered arrangement of double-twist cylinders [Zasadzinski et al. 1986]. Another proposition is the icosahedral edge model with translational symmetry of an icosahedral quasicrystal [Rokhsar & Sethna 1986].
Still 10 years ago BP were considered as “not yet of technological interest” [Wright & Mermin 1989]. Today, BP are investigated with respect to photonic crystal applications, like cavity-free lasing [Cao et al. 2002]. Special efforts are made to stabilize such phases by polymerization [Kikuchi et al. 2002].

## 4.2 BLUE PHASE LATTICES

### *4.2.1 STRUCTURE MODELS*

Twist arrangements of rod-like chiral nematic molecules base on the fact that a slightly rotated neighbor of these chiral objects is energetically favored compared to a parallel neighbor. For instance, the low-temperature phase of chiral nematic LCs is helical, i.e., twisted in one direction. In the following we will describe structures that are twisted in more than one direction.
Following the results of Meiboom et al., the BP are composed of “double twist cylinders”, which are modeled by twisted nematic structures and have the same cross-section at every position along the axis [Meiboom et al 1981]. The arrangement in the

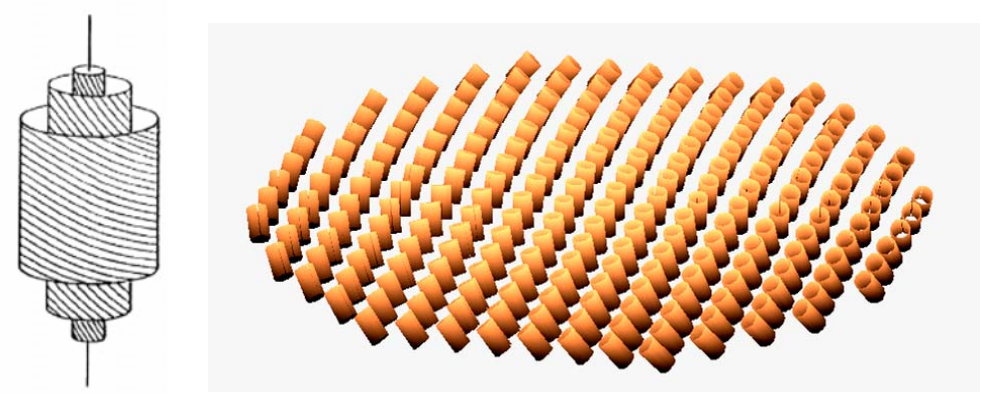

Fig. 4.1: Double-twist cylinder (left) and cross section of a double twist cylinder (right). The twist is right-handed coming from every direction. The director orientation on the axis is 0°, at the borders 45° with respect to the cylinder axis.

cross-section is double-twisted, i.e., the nematic director twists in every direction perpendicular to the cylinder axis (it rotates along “two” orthogonal directions). This is in contrast to the twist in one single direction around the pitch axis in the case of the helical phase of chiral nematic LCs. It can be proved analytically that the double twist arrangement has locally lower distortion energy than the helical arrangement [Meiboom et al 1981]. If the constituents of the chiral nematics are thought as screwlike objects and the most efficient way to pack a group of those about a central object, the double twist takes maximal advantage of the helical screw symmetry. This is also proven by molecular field simulations [Memmer 2000]. The helical arrangement allows a twist to the neighboring object only in one direction and remains parallel to the central “screwlike object”. Figure 4.1 shows the director field in the cross-section of a double-twist cylinder. The double twist is energetically more favorable than the simple helical arrangement, but this is only proven for the local case. If this is valid also for global arrangements (the whole cylinder) depends on the radius of the cylinder. It has been shown that the helical phase is favored globally if the radius cylinder is large enough [Wright & Mermin 1989]. For smalls cylinder radii the double twist cylinder is energetically more favorable than the helical arrangement of the same volume. It turns out that this is also valid for suitable *arrangements* of double twist cylinders as it corresponds to the real BP structure. The double twist cylinders (all of the same handedness) have to be arranged in three mutually orthogonal axes. By this way, the director-fields match between neighbored cylinders (Fig. 4.2).

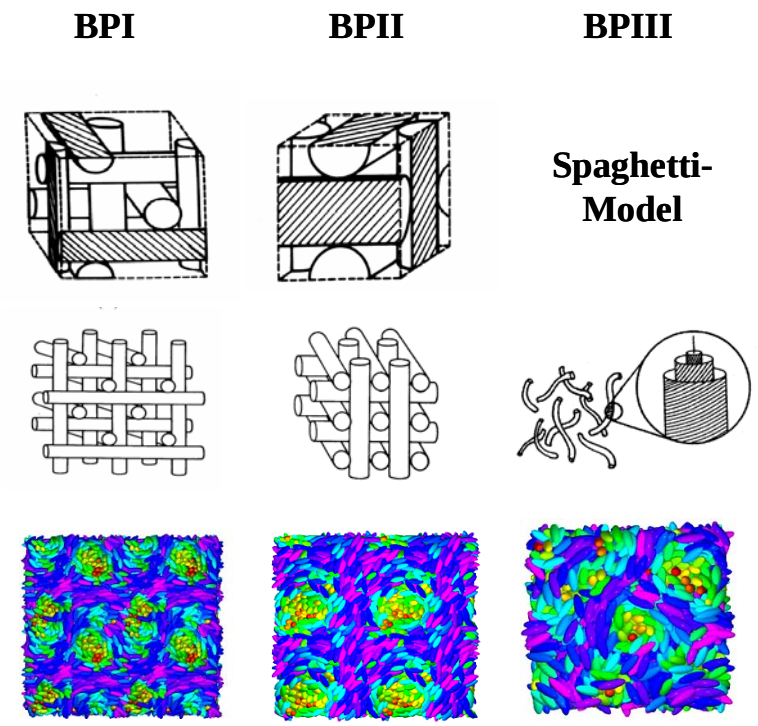


Fig. 4.2 : Elementary cubes (first row) and lattice structures (second row) from double-twist cylinders of the BPI, BPII and BPIII; taken from [Dubois-Violette & Pansu 1988]. The third row shows molecular field simulations for the 3 BPs; taken from [Memmer 2000].

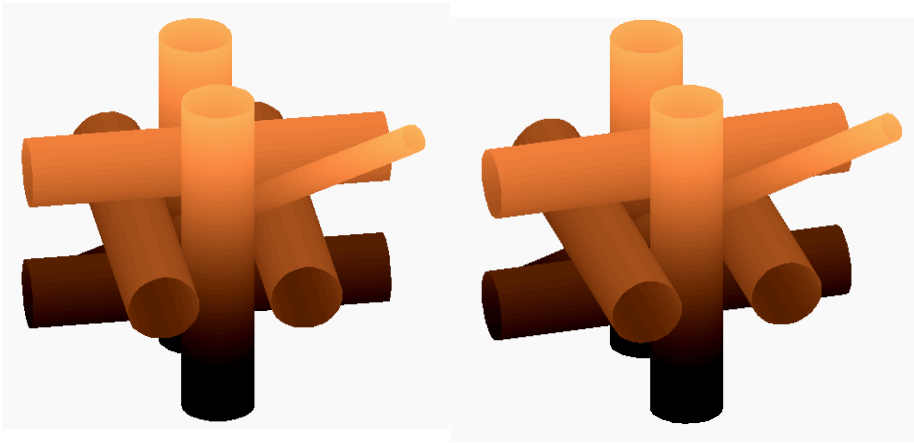

Fig. 4.3: Stereorepresentation (use the viewing method as described for Fig. 3.16) of a BPII lattice with defect line (diagonal thin cylinder). Geometrically, the defect line has a radius of $r\left(\sqrt{2}-1\right)/2$; r is the radius of the double twist cylinders

The BPI and BPII form periodical lattices in different arrangements of the double twist cylinders. Figure 4.2 shows the elementary cubes and the corresponding lattice structures from the double-twist cylinders for the BPI and the BPII as well as the scheme of the so-called spaghetti model of the amorphous BPIII. Spoken in crystallographic terminology:

the BPI is a body centered cubic array with an $O^8$ space group and the BPII model has a simple cubic translational symmetry with an $O^2$ space group [Wright & Mermin 1989]. We remember here that the directors represent the mean equilibrium orientations of the nematic molecules, which do not have perfect order. This is visualized in the simulations of Memmer (third row in Fig. 4.2). The molecules are free to diffuse inside the medium on condition that they keep a given average orientation at each place. The side length of the unit cells is between 200 and 500 nm. Every cube contains approximately $10^7$ molecules of the order of 5x5x25 $Å^3$.

For the BPII, the diameter of the double twist cylinders is of the order of a quarter of the pitch of the chiral nematic material. That causes a continuous twist at discrete axes of the lattice. The space between the double-twist cylinders is assumed as isotropic. Three double twist cylinders can be arranged that they are free of defects. However, a lattice arrangement of these cylinders produces also an inclination on certain lines in the lattice (see Fig. 4.3). By this way the BPI and BPII can be considered as lattices of defect lines of the order −1/2. The defect core radius can be calculated to be in the range of 10 nm after [Oswald & Pieranski 2000]. For the BPII the defect lines form 2 lattices of the diamond type [Oswald & Pieranski 2000].

In the following, we will focus on the BPII structure. Calculations concerning the optics of BP in section 4.3 and experimental investigations in section 4.4 are only made for the BPII phase. The right side of Fig. 4.4 shows a cut through the cubic elementary cell of a BPII. From top to bottom we follow the twist of the director by an angle of $\pi$, which corresponds to passing through two cylinders. Crossing one cylinder corresponds to a twist change of $\pi/2$. For this reason the half pitch of the material is equal to the cube side

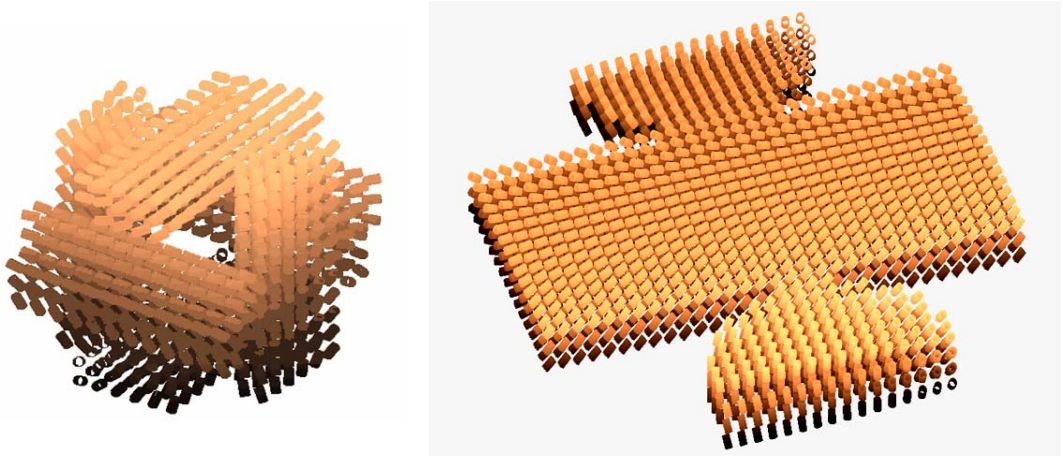

Fig. 4.4: Director configuration of a BPII unit cell (left) and the cut of a BPII (right) at the top of the unit cell. The cut shows the cross-section of the double-twist cylinder along its axis (lying in the plane) and the cross-sections (perpendicular to the axis) of the neighboured double twist cylinders. At the points of contact between the three cylinders the directors match.

length of the BPII.

### *4.2.2 BRAGG REFLECTION OF SIMPLE CUBIC CRYSTALS*

Since liquid crystal BP (LCBP) are cubic crystals (with a certain interior arrangement of the rod-like LC molecules), Bragg reflection occurs at certain directions when the sample is illuminated with monochromatic light. For that reason, LCBP can be considered as anisotropic photonic crystals with weak refractive index contrast.
Using a microscope with conoscopic setup (Fig. 4.5), the directions of Bragg reflection are observed in the focal plane and they appear as lines, the so-called Kossel lines [Kossel et al. 1935]. Every Kossel line corresponds to Bragg reflection of light at a certain set of planes described by the Miller indices h,k,l, where h,k,l are positive integer numbers and the vector (h,k,l) is the normal to this set of planes. For instance, the set of planes [100], [010] and [001] is parallel to three non-parallel sides of the unit cell cube of the lattice; the set of planes [111] is parallel to a space diagonal of the cubic unit cell.
Bragg reflection occurs for a set of planes if

$$\cos\theta = \frac{\lambda\sqrt{h^2+k^2+l^2}}{2na} \tag{4.1}$$

with the wavelength $\lambda$, the Bragg angle $\theta$, the side length a of the cubic cell, the averaged refractive index n and the Miller indices h, k, l of the scattering lattice planes of the cubic crystal. Using Eq. (4.1) makes it possible to calculate the diffraction pattern of a crystal for arbitrary wavelengths by applying the formula to every set of planes of the crystal and adding the Kossel lines graphically. The BPII is a simple cubic structured crystal, i.e.,

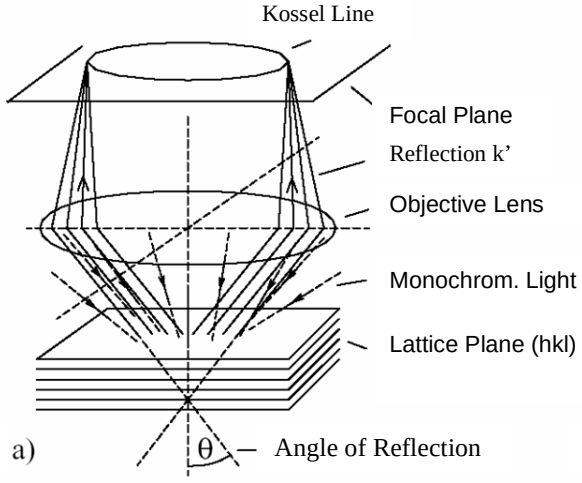


Fig. 4.5: Conoscopic setup, used as procedure for Kossel diagrams; Figure from [Jérôme & Pieranski 1989]

Bragg reflection occurs for all lattice planes, in other words: for all triplets of non-negative integers h, k, l with h+k+l>0 in equation (4.1). The BPI has a body centered cubic structure, i.e., Bragg reflection occurs only if h+k+l is an odd number larger than 1. Details about selection rules for lattices of different symmetry can be found in [Schwarzenbach 1993].

Applying (4.1) to a cubic crystal of a period of 240 nm we did calculate the Kossel lines for a simple cubic symmetry (corresponding to BPII) and a body centered cubic symmetry (corresponding to BPI) for different wavelengths. Figure 4.5 shows the Kossel diagrams for these symmetry types and a crystal in [1 0 0] orientation, i.e., parallel to the focal plane. According to the selection rule for body centered cubic structures (see [Schwarzenbach 1993]) Bragg reflection will be observed at the set of planes represented by [h,k,l] = [1,1,0] like it is shown in the second row of Fig. 4.6. The corresponding Eq.

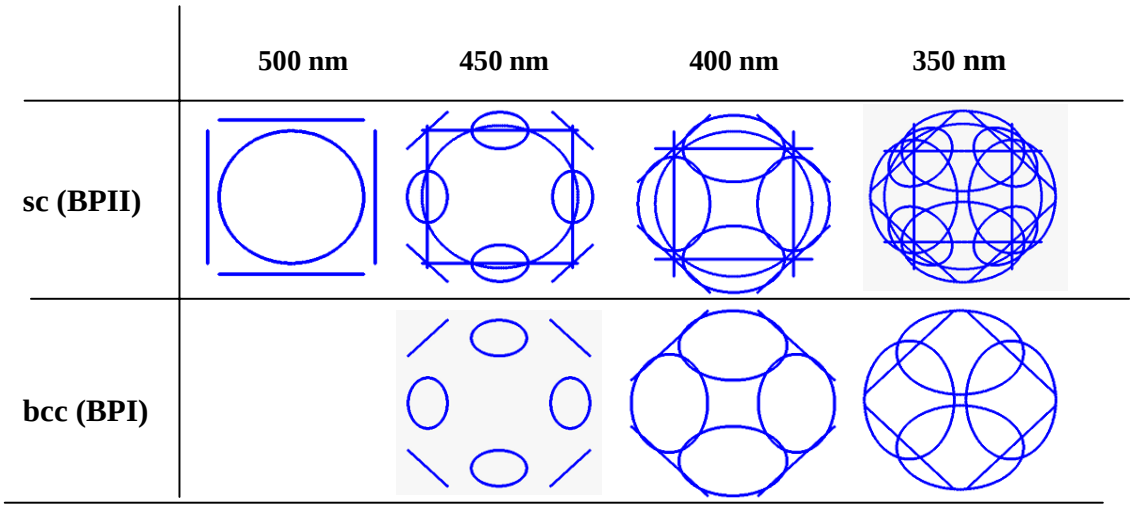


Fig. 4.6 : Kossel diagrams at different wavelengths for simple cubic (sc) and body centered cubic (bcc) lattice structures with a period of 200 nm for crystals in [1 0 0] orientation

(4.1) cannot be satisfied for $\lambda = 500$ nm and no Bragg reflection occurs at this wavelength.

This method delivers the location of Kossel lines but no additional information, like intensity or phase of the Bragg reflected light. The inner structure of the unit cell is not taken into account. Yet, for isotropic gratings the reflection intensity on the Kossel lines and the distribution of the light intensity on different Kossel lines depends strongly on the lattice fill-factor and the indices of refraction inside the lattice.

Nevertheless, this (crystallographic) method yields good results concerning the qualitative diffraction patterns also for LCBP. It is also useful to determine the crystal orientation, the lattice period and to distinguish the BP type.

In section 4.3 we will investigate the optical behavior of the BPII lattice in considering the anisotropic structure of the unit cell.

## 4.3 PLANE WAVE APPROACH TO THE OPTICS OF BLUE PHASES

Optics of BPs were investigated by crystallographic methods [Jérôme & Pieranski 1989], many-wave optics methods [Belyakov & Dmitrienko 1989] and Fourier methods based on assumptions about the dielectric tensor properties [Hornreich & Shtrikman 1993].
We have tested several approaches to model optical properties of three dimensional anisotropic structures. Among them are the finite difference time domain (FDTD) method, the Fourier modal method and more classical matrix methods like rigorous matrix methods for stratified media. As a fast and reliable method to study the optics of LCBP structures we used the 4x4 Berreman matrix method, which we already applied to three-dimensional liquid crystal problems in previous investigations [Bohley & Scharf 2002]. For the special case of BP structures a 4x4 matrix method was already applied by [Berreman 1984].

### *4.3.1 MATRIX METHOD FOR ANISOTROPIC CRYSTALS*

The 4x4 Berreman method is based on the assumption that light propagation can be described as reflection (or transmission) by a stratified medium, as described and applied in section 3.1. In order to find the Bragg reflection of the crystal for a certain direction, we divide the crystal into parallel and equidistant planes which are perpendicular to the propagation direction, as it is shown in Fig. 4.7. The local dielectric tensor is calculated by equation (2.11), which was derived in section 2.4. Next, we average the dielectric

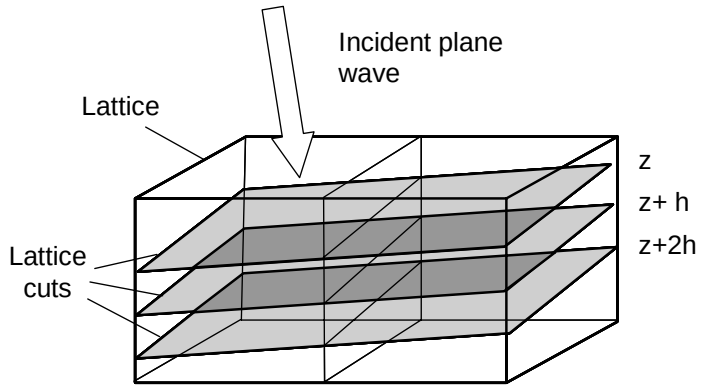


Fig. 4.7: Lattice and cuts through the lattice perpendicular to the incident plane wave

tensors in each of these parallel planes. The average is made arithmetically, which is justified if the wavelength of the incident light is much larger than the period of the anisotropic crystal. So we get for a certain propagation direction of light a stack of dielectric tensors along the propagation direction through the crystal. In the following this procedure will be illuminated when applied to a BPII crystal (section 4.2.1).
The left side of Fig. 4.8 shows the typical appearance of such director planes in two examples and the right side of Fig. 4.8 shows the corresponding averaged biaxial index-ellipsoid.

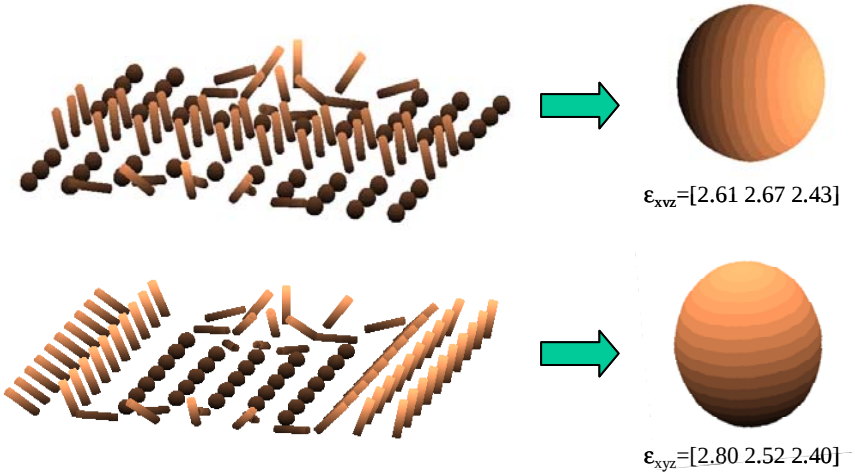


Fig. 4.8: Examples of two different cuts through the BPII director field (uniaxial elements) and the corresponding (biaxial) index ellipsoids, obtained by averaging the dielectric tensors of the [1 0 0] lattice planes

Figure 4.9 demonstrates the behavior of the biaxial index-ellipsoid more exactly. The dielectric tensors will be observed passing through a BPII lattice in the [1 0 0] orientation in a depth of 840 nm, which corresponds to 3.5 lattice periods. The eigenvalues of the averaged dielectric tensors are $\varepsilon_x$, $\varepsilon_y$ and $\varepsilon_z$ (arranged according to their size). We assumed for the ordinary refractive index $n_o = 1.5$ and for the extraordinary index $n_e = 1.8$. So, the eigenvalues of the averaged dielectric tensor are between 2.25 and 3.24.

Passing through the cubic crystal at normal incidence we get averaged dielectric tensors with the same period as the spatial period of the lattice (here: 240 nm), i.e., the side length of the unit cell. In our example this period corresponds to 20 layers of a thickness of 12 nm (see the left side of Fig. 4.9). The orientation angles of the biaxial index ellipsoid change with the same period. Note that the semiaxes of the biaxial index ellipsoid vary only a little around the mean value. At the same time, these mean values $n_x$, $n_y$ and $n_z$ are distinctly different. On the other hand, the orientation angles $\xi$ and $\theta$ remain constant as $\xi = \pi/2$ and $\theta = 0$ and $\varphi$ increases linearly. That means, the biaxial index ellipsoid keeps approximately the same form but changes its orientation by twisting when

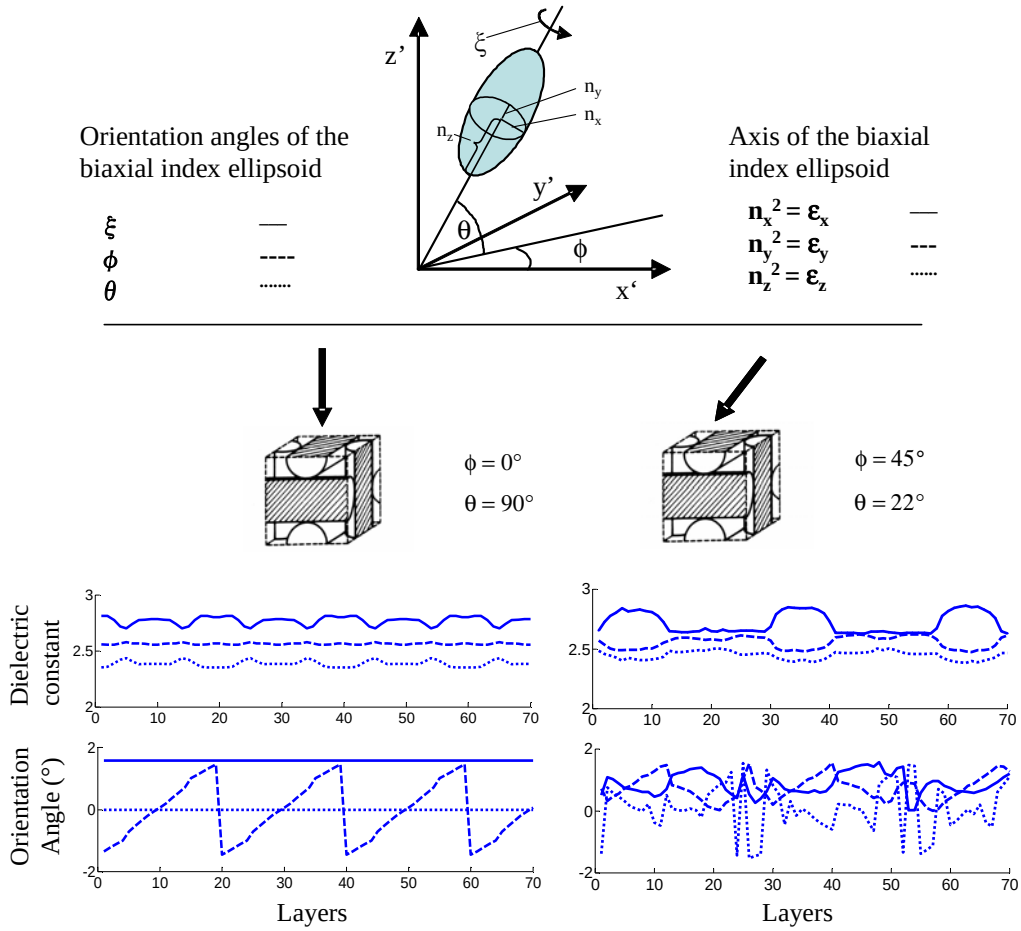


Fig. 4.9: Top: Geometry of the biaxial index ellipsoid in the cartesian system x'-y'-z'. Bottom: Orientation angles of the biaxial index ellipsoid (left side) and the dielectric constants $e_i = n_i^2$ vs. the layer number. The left column is for normal incidence and the right column for oblique incidence.

the light traverses the BPII crystal in the [1 0 0] direction. This behavior reminds to the helical phase of a chiral nematic LC, where the uniaxial index ellipsoid twists when passing through the structure normally.

The situation is more complicated for oblique incidence, as shown on the right side of Fig. 4.9. For oblique incidence at $\phi = 45°$ and $\theta = 22°$ the period of the dielectric tensors is about 28 layers instead of 20 layers for normal incidence. A good discrimination of the dielectric values is no more possible.

The calculated dielectric tensor stack for a certain direction of incidence is now used to calculate the optical properties of the lattice with the 4x4 matrix method of Berreman [Berreman 1972]. We will model the interaction of the plane wave with the real crystal lattice at oblique incidence by the interaction of the wave with the artificial stack of planes extracted perpendicular to the wave propagation, as described above. Figure 4.10

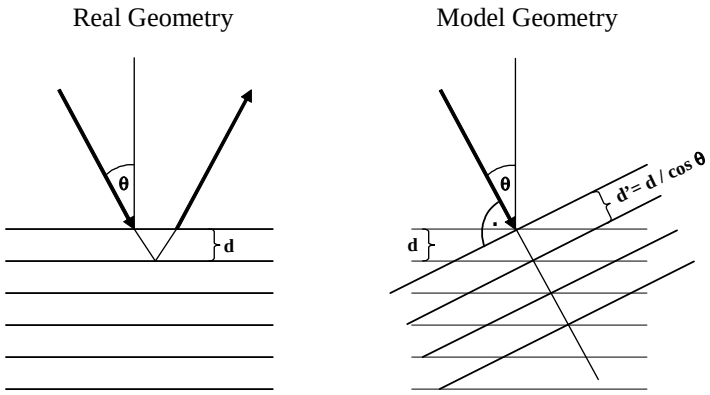


Fig. 4.10 : Left: Geometry of a lattice of period d in Bragg reflection.
Right: The model geometry, in which the Bragg reflection is considered as being of normal incidence for an artificial lattice of the period d'. The artificial lattice consists of planes which were obtained by intersecting the original lattice normal to the incident plane wave.

compares the real and the artificial situation. The left side of Fig. 4.10 shows the Bragg reflection at a lattice of period d. The right side shows the same lattice in our model, which assumes Bragg reflection as being normal to the artificial lattice planes.

In the model geometry (right side of Fig. 4.10) the plane wave pass through the same optical paths as in the real geometry (left side of Fig. 4.10). Note that by reasons of the crystal symmetry the plane waves "see" on their incident way the same dielectric tensor stack as on their reflected way. This fact is covered also in the model geometry with normal incidence onto the artificial crystal. We assume that the transitions of the dielectric tensor inside the medium are smooth and for that reason no total reflection occurs.

In the real geometry Bragg reflection appears for the wavelength

$$\lambda = 2\bar{n}d\cos\theta \quad , \tag{4.2}$$

where $\bar{n}$ is the average index of refraction of the lattice. In the model geometry, Bragg reflection occurs for the wavelength

$$\lambda' = 2\bar{n}d' = 2\bar{n}d/\cos\theta \quad , \tag{4.3}$$

where d' is the lattice period of the artificial lattice. Substituting $\cos\theta$ in (4.2) and (4.3) gives

$$\lambda' = 4\bar{n}^2 d^2 / \lambda \quad . \tag{4.4}$$

That means, Bragg reflection, which occurs for the real geometry at the wavelength $\lambda$, will appear with the same intensity and phase behavior for the model geometry at the wavelength $\lambda'$ according to Eq. (4.4).
Using this wavelength transformation the 4x4 Berreman method can be applied to anisotropic crystals. The output are Jones matrices of reflection and transmission for a chosen wavelength. Note that this method is a plane wave approach and neglects lateral scattering in the medium. The method can be applied to investigate reflection and transmission in arbitrary anisotropic crystals.

### *4.3.2 APPLICATIONS TO THE BLUE PHASE II STRUCTURE*

REFLECTION SPECTRA

Based on the BPII model used in the previous sections we did calculate the reflection spectrum of a BPII layer with the matrix method explained above. We assumed a BPII layer in [1 0 0] orientation with a thickness of 10 µm, an ordinary index of refraction $n_o = 1.5$, and an extraordinary index $n_e = 1.8$. For the space between the double twist cylinders we assumed isotropic space with the average refraction index n = 1.61 fulfilling the relation $n^2 = (n_e^2+2n_0^2)/3$ [Blinov & Chigrinov 1994].
Figure 4.11 shows the calculated reflection spectra for different polarizations. The light is at normal incidence (left) and at oblique incidence at 20° (right). For all types of polarization we get a selective reflection, which is strongest for the circularly polarized light of the handedness of the chiral nematic material. Like for the helical phase of the chiral nematic LC material the reflection spectrum is shifted to shorter wavelengths for

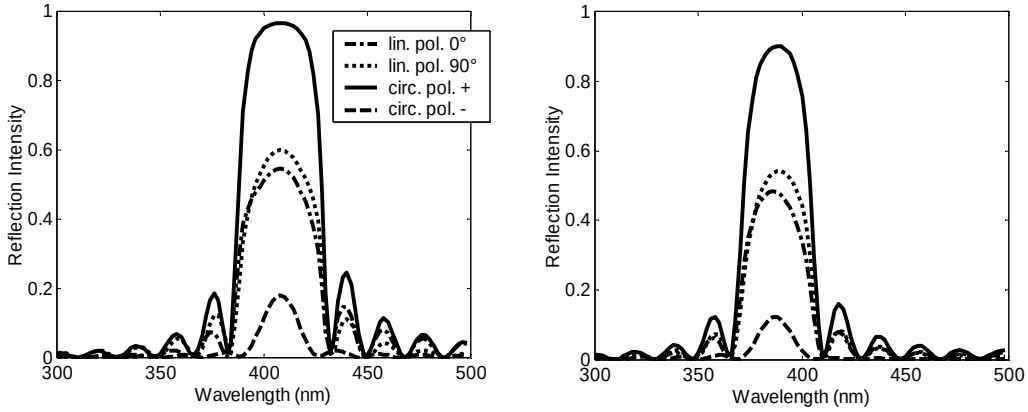


Fig. 4.11 : Reflection spectra of a BPII at normal (left) and oblique incidence at an angle of 20° (right) for different polarizations of the incident light. Strong selective reflection is observed for the circular polarization of the same handedness as the chiral material.

oblique incidence.
The wavelength region with selective reflection depends on the orientation of the crystal. At normal incidence the squares of the selective reflection wavelengths for the [1 0 0], [1 1 0] and [1 1 1] orientations are related like 1:2:3, as it turns out from Eq. (4.1). In section 4.4 we will see how this affects to the colorful occurrence of the BP crystals.

DIFFRACTION PATTERNS

In order to investigate the whole spatial optical behavior of a BPII layer, we evaluate the Jones matrices in reflection and transmission for every direction of incidence and for different wavelengths. The intensities will be mapped into the focal plane and we obtain intensity and phase distributions, which we call “diffraction pattern”. These calculated diffraction patterns correspond to the observation in the conoscopic plane of a microscope (see Fig. 4.5).
Simulated diffraction patterns for a BPII crystal in [1 0 0] and [1 1 0] orientation are shown in Fig. 4.12. We assumed the same material parameters as before. The incident light is right-handed circularly polarized. Figure 4.12 shows clearly the Kossel lines in four-fold symmetry for the [1 0 0] orientation and two-fold symmetry, as it is expected for the [1 1 0] orientation. The “opening” of the Kossel lines for decreasing wavelengths was already figured out in section 4.2.2 by means of the “crystallographic method”.

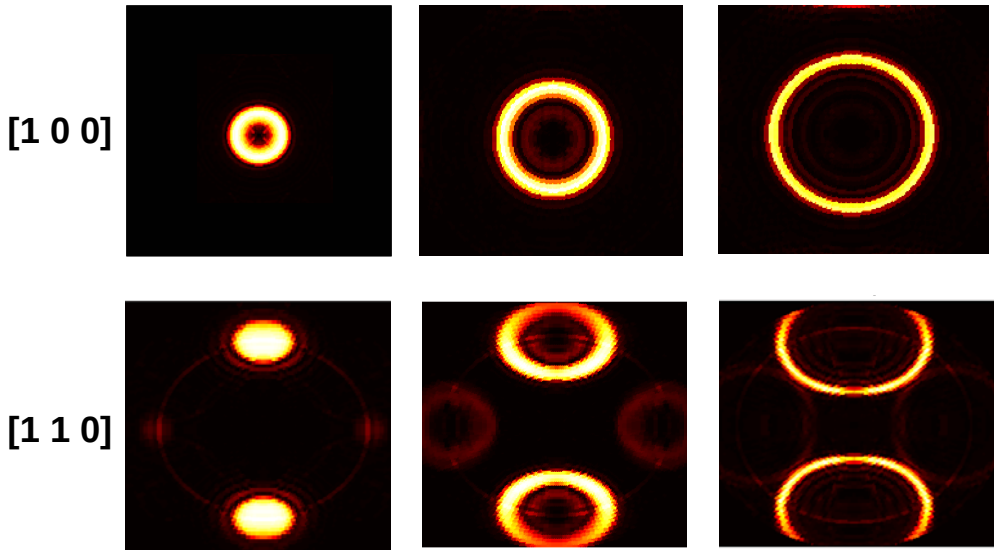


Fig. 4.12: Simulated reflection diffraction patterns of BPII in [1 0 0] (top) and [1 1 0] (bottom) orientation for different wavelengths. (From left to right: 652 nm, 570 nm, 424 nm). The structure is cubic with a cell side length of 200 nm, $n_o = 1.5$, $n_e = 1.8$. Interference patterns are composed of reflection intensities calculated for directions up to an incident angle of $\theta = 70°$.

In [Bohley & Scharf 2003] we did investigate among other things the intensity behavior of Kossel lines at cross points in comparison with results of [Miller et al. 1996]. Now, we focus on the polarization properties of the reflected light on the Kossel lines. Furthermore, we are interested in the polarization properties of the Bragg reflected light depending on the polarization of the incoming light.

POLARIZATION OF BRAGG REFLECTED LIGHT

We are especially interested in the [1 0 0] crystal orientations. For that purpose, we have calculated an interference pattern for the same parameters as above and obtained intensities and phases of the Bragg reflection on a special Kossel line which is circular symmetric in the conoscopic plane at an incidence of $\theta = 45°$. The calculations were made for a wavelength of 467 nm. Figure 4.13 shows at the top left the reflection

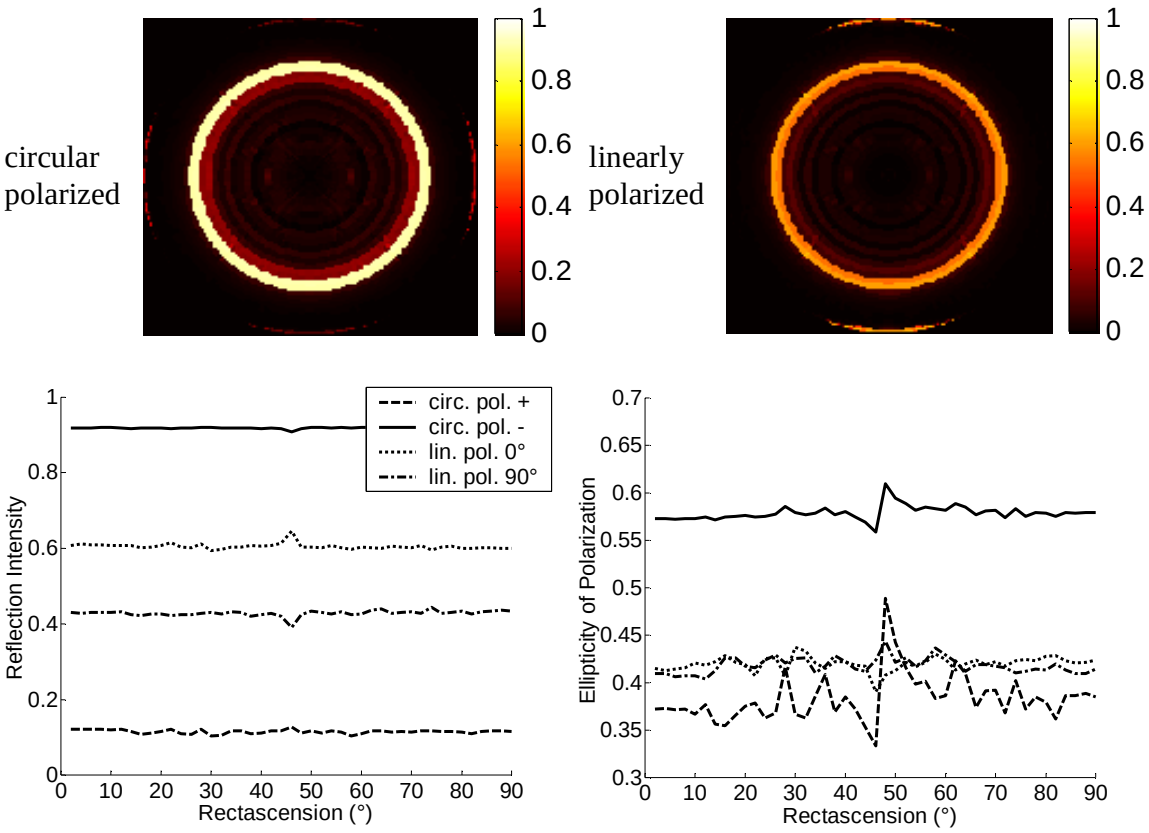


Fig. 4.13: Top: Simulated reflection diffraction patterns of BPII in [1 0 0] orientation for a wavelength of 467 nm. Left side: circular polarized incident light; Right side: linear polarized light parallel to the x'-axis ($\phi = 0$)
Bottom: Reflection intensity and ellipticity of the polarization for the Bragg reflected light of different input polarization vs. the rectascension angle $\phi$ (Fig. 4.9)

intensities in the conoscopic plane for left handed circular polarized light (the LC structure is also left handed) and at the right the reflection intensities for linearly polarized light (parallel to the x'-axis, i.e., $\phi = 0°$). As expected, we get higher reflection intensity for the circularly polarized light with the same handedness as the structure, and a lower reflection intensity for the opposite circular polarization (left side at the bottom of Fig. 4.13). For linear input polarizations we get approximately half the reflection intensity as for the case of circularly polarized light of the material handedness.

Analyzing the ellipticity of the Bragg reflected light on the Kossel line in Fig. 4.13, it is possible to compare simulated and measured results. Flack et al. measured Mueller matrices of Bragg reflected light for different types of BP, with linear polarized incoming light and oblique incidence at $\theta = 45°$ [Flack et al. 1982]. From measurements at single points they concluded that the Mueller matrices of the BPI and BPII phases are those of a homogeneous elliptical polarizer with an ellipticity of approximatively 0.7 (where the ellipticity is defined as the amplitude ratio of the axes of the polarization ellipse). That is, of a material, which reflects a specific elliptical polarization of the ellipticity 0.7. We have simulated the reflection behavior along a whole Kossel line and found the same principal behavior but other values for the ellipticity, depending on the rectascension $\phi$ of the direction of the incident light. For a [1 0 0] oriented BPII crystal we found ellipticities of the eigenpolarizations between 0.5 and 0.65. The corresponding normalized Mueller matrices M for $\phi = 0°$, $\phi = 45°$, $\phi = 90°$ and averaged over $\phi = 0°$ to 90° are

$$M(0°) = \begin{pmatrix} 1.000 & -0.139 & 0.135 & 0.922 \\ -0.139 & 0.350 & 0.010 & -0.100 \\ -0.135 & -0.010 & 0.306 & -0.193 \\ 0.922 & -0.100 & 0.193 & 0.957 \end{pmatrix} \quad M(45°) = \begin{pmatrix} 1.000 & 0.082 & 0.204 & 0.909 \\ 0.082 & -0.341 & -0.016 & 0.124 \\ -0.204 & 0.016 & -0.383 & -0.140 \\ 0.909 & 0.124 & 0.139 & 0.958 \end{pmatrix}$$

$$M(90°) = \begin{pmatrix} 1.000 & 0.139 & -0.131 & 0.923 \\ 0.139 & 0.340 & 0.062 & 0.108 \\ 0.131 & -0.062 & 0.297 & 0.194 \\ 0.923 & 0.108 & -0.194 & 0.956 \end{pmatrix} \quad Mav = \begin{pmatrix} 1.000 & 0.072 & 0.093 & 0.921 \\ 0.072 & 0.014 & 0.001 & 0.108 \\ -0.093 & -0.001 & -0.026 & -0.068 \\ 0.922 & 0.108 & 0.068 & 0.960 \end{pmatrix}.$$

These matrices were calculated from the Jones matrices obtained by using the method described in section 2.5.2. They describe a Stokes vector transformation like a reflecting elliptical polarizer whereas the major axis of the corresponding polarization ellipse changes slightly with the rectascension angle $\phi$. The average Matrix *Mav* describes the Mueller matrix of the plane wave which is reflected by a polycrystalline specimen allowing all azimuthal orientations of the crystal platelets. This is the normalized matrix

of an elliptical polarizer and it is in good agreement with the single point measurements showed in Fig. 3(b) of [Flack et al. 1982] and also with the considerations in [Hornreich & Shtrikman 1981] for polycrystalline specimens.

## 4.4 EXPERIMENTAL RESULTS

### *4.4.1 PREPARATION AND APPEARANCE OF BPII CRYSTALS*

In order to characterize liquid crystalline Blue Phases we investigated the phase transitions of a mixture of the chiral dopant CB15 and the liquid crystal mixture E48 (both from Merck). For different weight ratios we found the typical appearance of the BPII by slowly cooling down from the isotropic phase. The phase diagram gives information about the most appropriate weight ratio for the absolute temperature and the temperature range of the BP. The appearance of the phases at different temperatures was observed with a polarization microscope (DMRP Leica) (mainly between crossed polarizers) and a high precision hot stage Instec HS1 (better than 10 mK relative). We found as the most suitable mixture a weight ratio of 55% CB15 in E48 for which the transition point of the isotropic phase to the BP is at 25.5°C and the transition from the BP to the cholesteric is at 22.3°C. For smaller weight ratios the transition points are at higher temperatures and also the temperature width of the BPs is larger. However, we preferred to work at room temperature. The mixtures are easily super-cooled. Therefore, the recording of phase diagrams is a lengthy procedure.

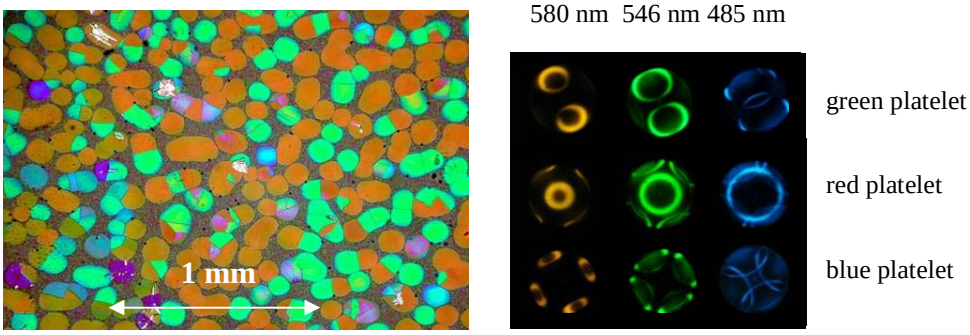


Fig. 4.14: BPII platelets with a domain size of 100-150 µm (left); corresponding Kossel patterns for different wavelengths and platelets of different colors (right)

In order to obtain BP crystals with a domain size large enough to produce interference patterns, we tried different cooling rates for the 55% CB15-E48 mixture. Slow cooling, with a rate of 0.001 K/min, from 27°C to 25°C allows the growth of BPII crystals with domain sizes up to 200 µm. The typical appearance of different colors, which correspond

to different crystal orientations, is shown in the left side of Fig. 4.14. The photograph was taken in reflection between crossed polarizers.
The reflection behavior of the BPII was investigated also with the conoscopic setup of the polarization microscope (Fig. 4.5). Diffraction patterns of the BP crystals were obtained (right side of Fig. 4.14), which show the Kossel lines, corresponding to Bragg reflection caused by the crystalline structure of the BPII. For the observation of diffraction patterns and their polarization properties high quality large crystals are required. Therefore, we used industrially fabricated test cells with rubbed polyimide coating (produced at ASULAB S.A.). The typical thickness of the LC layer was 7 μm. The surface substrates were 300 μm thick, allowing to use microscope objectives with high numerical aperture. The diffraction patterns in Fig. 4.14 are digital photographs, taken in the focal plane of the polarization microscope objective (100 x 1.3 oil Zeiss) for different wavelengths selected by conventional interference filters (Edmund Scientifics) with a full-width half-maximum of 10 nm.

### *4.4.2 POLYMERIZATION OF BP CRYSTALS*

The structure of the blue phase is very fragile and small changes in the composition of the mixture can be enough to destroy the three dimensional self-organized nanostructure. In order to stabilize BP crystals with a sufficient domain size, we investigated photopolymerization for different materials. The materials are usually stable within a temperature range of 1K. To control the polymerization conditions we investigated polymerization with a mercury discharge lamp HBO100 in a fluorescence microscopy setup. Controlling the temperature with the microscope hot stage, we achieved in situ

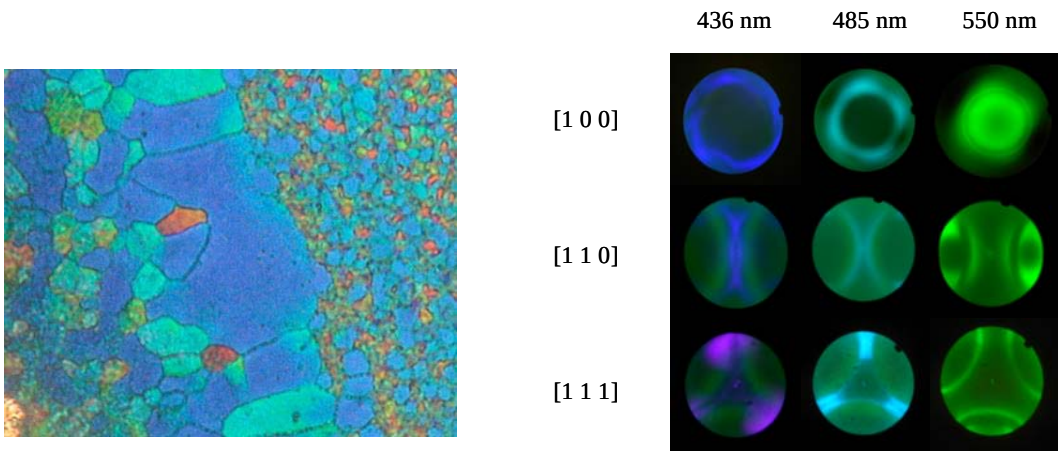


Fig. 4.15: Texture and Kossel diagrams of frozen liquid crystalline BPs obtained from a polymeric liquid crystalline system.

polymerization of the Blue Phases.
Two different concepts are promising: The first is the photo-polymerization of BP and the second is the polymerization by gel formation and stabilization [Kikuchi et al. 2002].
In order to photopolymerize a BP we used a side chain liquid crystal polymer from Wacker that shows a BP at 180°C. With this material we obtained very stable BP

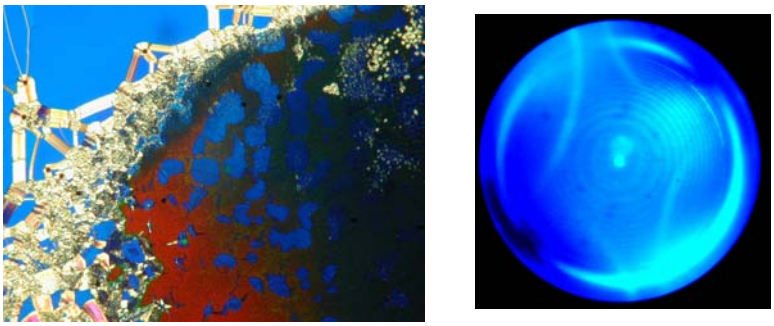

Fig. 4.16: Left: micrograph of a photopolymerized mixture of RM257, CB15 and E48. Right: diffraction pattern of one BP crystal domain for a wavelength of 485 nm.

crystals. A typical texture of this photopolymerized BP is shown on the left side of Fig. 4.15. Kossel diagrams were obtained with the same conoscopic setup as before. The three different crystal orientations [1 0 0], [1 1 0] and [1 1 1] are clearly visible by the different symmetry types of the diffraction patterns.
Polymerization by gel formation was obtained using a mixture of a liquid crystal mesogenic monomer (RM257), a liquid crystal mixture (E48) and a chiral dopant (CB15). Under weak UV exposure, this allows stabilization and leads to a weakly linked network, a gel. At the transition point from the isotropic to the BP (33°C) we photopolymerized with different amounts of ultraviolet light and managed to freeze a region which contains a cholesteric phase with the typical oily streaks (left region of the left image in Fig. 4.16) and a BP region (middle of the left image in Fig. 4.16) with crystalline domains of blue appearance. These domains remained stable and we investigated diffraction patterns of the BP domains. These patterns showed Kossel lines (example on the right side of Fig. 4.16) but not as clearly as in Fig. 4.15, which indicates a degeneration of the polymerized BP crystal. The polymerization of better quality BP crystals will be the subject of further investigations.

### *4.4.3 DIFFRACTION PATTERNS IN EXPERIMENT AND SIMULATION*

To prove the simulation concept presented in section 4.3.1 we compared the simulation results with experiments. Between crossed polarizers the Kossel lines for single crystals of the BP are not uniform in intensity. As an example we have chosen a platelet with a [1

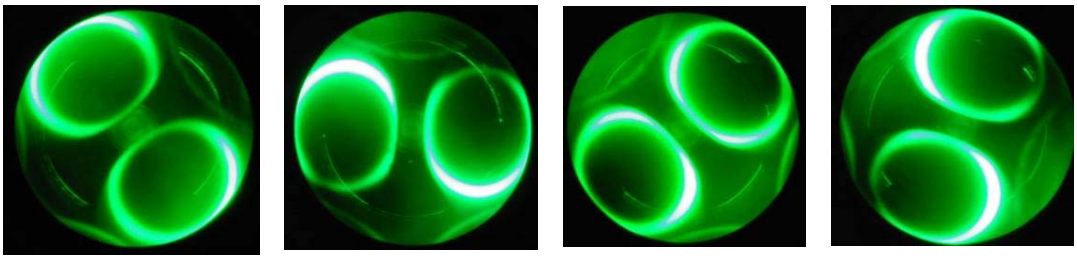

Fig. 4.17: Photographed Kossel patterns of a BPII crystal in [1 1 0] orientation at 546 nm between crossed polarizers for different rotational orientations with respect to the polarizers. The BP was obtained by a mixture of 55% chiral dopant CB15 in the Liquid Crystal E48.

0 0] crystal orientation. We obtained a diffraction pattern in the expected two-fold symmetry. When the BP crystal is rotated between crossed polarizers the intensity of the Kossel lines varies depending on the position. Fig. 4.17 shows photographs of diffraction patterns, taken of a BPII crystal in [1 1 0] orientation. The crystals were grown from the 55% CB15-E48 mixture, which was used already in section 4.4.1.

These diffraction patterns were simulated by the matrix method described in section 4.3.1. Figure 4.18 shows at the bottom photographs of the Kossel patterns of the BPII mixture, taken between crossed polarizers for different orientations of the polarizer. We

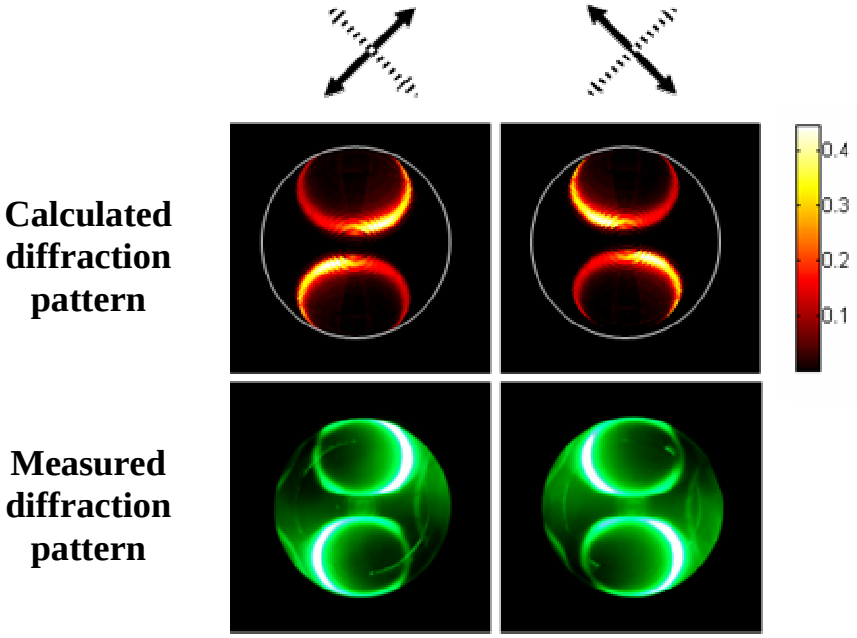


Fig. 4.18: Top: Calculated BPII diffraction pattern in reflection up to an azimuth angle of 70° in a crossed polarizer set-up; left side: analyzer 45° and polarizer 135° to the sample, right side: analyzer 135° and polarizer 45° to the sample. Bottom: Photograph of a BPII diffraction pattern, with the same crossed polarizer setup as in the simulation

have chosen again a BPII crystal platelet with [1 1 0] orientation. The polarizers are oriented at 45° as shown on top of the figure. This behavior has been confirmed by the simulations, as can be seen clearly by direct comparison in Fig. 4.18. The intensity distribution is shown for the LCBP crystal and a scale is given for the absolute value of reflected intensities. Although the intensity distribution looks very much the same there is no complete coincidence. That might be caused by the response of the digital camera or the high numerical aperture of the objective. The conoscopic images depend also on the quality of the polarizers.

### *4.4.4 BLUE PHASE OF DYE DOPED LIQUID CRYSTALS*

In some recent publications fluorescent dye-doped LCs are used to establish functionalities like electrically tunable lasers [Matsui et al. 2003], non-linear induced self waveguiding [Warenghem et al. 1998] and fluorescence in a chiral nematic LC host [Schmidtke & Stille 2003].
Absorptive dyes are mainly used to achieve special functionalities. The Heilmeier display for instance is using a dichroic dyed Fréedericksz cell, which makes use of anisotropic absorption feature [Heilmeier & Zanoni 1968]. Furthermore, for some liquid crystal devices, the need for external polarizing filters can be reduced or eliminated. The light propagation in chiral structures with dyes is changed significantly [Sah & Suresh 1994]. This leads to the assumption that incorporation of absorptive dyes allows for tuning the optical reflection and transmission properties of LCBP.
Liquid crystals that contain suitable dichroic (anisotropic) dyes can absorb polarized light. Depending on the dye material used, one can have absorption parallel or perpendicular to the director orientation. Usually, mixtures of dyes and LC hosts are studied. The established guest-host interaction between the dye molecule and the liquid crystal causes an alignment of the dye. This provides the possibility to modulate the light propagation additionally. In order to study LCBP produced by dye-doped LC materials we did investigate a mixture of 2% P80 (dye), 55% CB15 in E48 (liquid crystal), which has a BPII. We observed the Kossel lines in reflection and transmission with the help of interference filters. Figure 4.19 shows photographs of diffraction patterns of a LCBP crystal in [110] orientation, established by slow cooling. A contrast inversion is observed when switched from reflection to transmission observation conditions. In the case of [100] orientation, the intensity distribution shows only a slight change when rotated. The situation gets more spectacular when we look at a different crystal orientation. Here we have a typical example how drastically the optical properties can be changed. Changing from reflection to transmission shows the same contrast inversion. But now the contrast

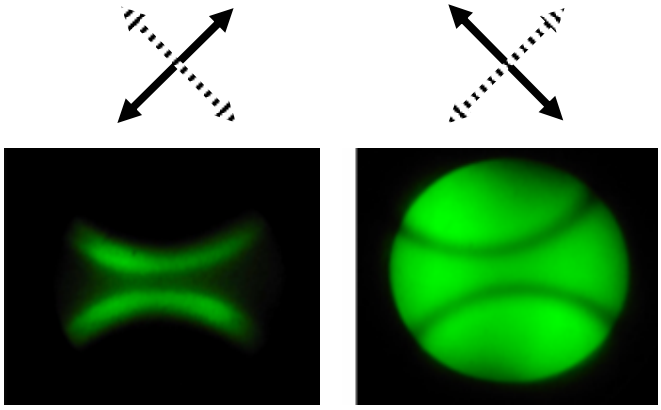

Fig. 4.19: Photograph of diffraction patterns in transmission up to an azimuth angle of 70° for a mixture of 2% P80, 55% CB15 in E48 at 25° illuminated with monochromatic light at 535 nm. The pattern was photographed in a crossed polarizer set-up. Left side: analyzer 45° and polarizer 135°. Right side: analyzer 135° and polarizer 45°

of the diffraction pattern becomes dependent on the orientation and changes the contrast for different orientations with respect to the polarizers.

Because of the very complicated light propagation conditions it is difficult to find simple arguments to explain this behavior. Therefore it is worth to simulate this situation with the method described in section 4.3.1. The optical behavior of the material is determined by its dielectric tensor. Absorption is described by the imaginary part of the refractive

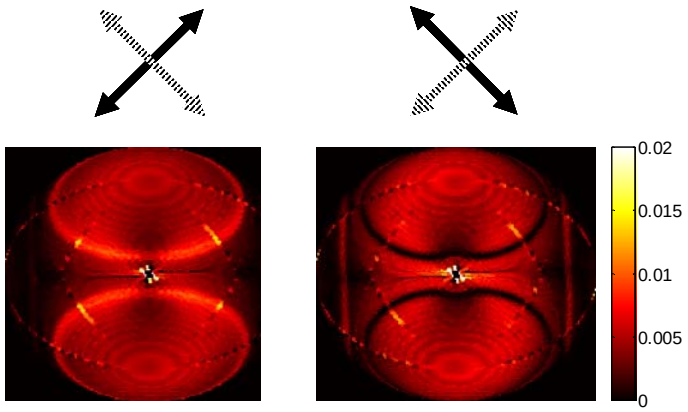


Fig. 4.20: Calculated diffraction patterns in transmission at 535 nm for a BPII with absorption at the extraordinary axis in [1 1 0] orientation. Azimuth angles up to 90°. Crossed polarizer set-up. Left side: analyzer 45° and polarizer 135°. Right side: analyzer 135° and polarizer 45°

index. The 4x4 method is able to treat this extension and for the dye doped mixtures we assume absorption only for the extraordinary index (dichroic behavior). In the

simulations shown in Fig. 4.20 we reproduce the same setup as for the observations of Fig. 4.19. We show the transmission diffraction patterns of a [110] BPII crystal in monochromatic light at 535 nm, the refractive indices of the 10 µm thick material are assumed $n_o = 1.5$, $n_e = 1.8\text{-}0.05i$. For a homogeneously aligned nematic LC, this imaginary part of the index causes a contrast ratio of approximately 1:3. The observed (Fig. 4.19) and the calculated diffraction patterns (Fig. 4.20) show the same contrast inversion of the diffraction pattern if the sample is rotated by 90°. We believe that the contrast alternation is due to the strong dichroism of the material.

### *4.4.5 CONCLUSIONS*

The different BP as natural photonic crystals were described and structurally analyzed. We did investigate diffraction patterns of BPII crystals following the simple cubic double twist cylinder model. We did develop a plane wave method based on the 4x4 matrix technique of Berreman, which was extended to anisotropic 3D crystals. To the best of our knowledge, this is the first time that the entire diffraction pattern of a BPII has been calculated. The results are in good agreement with measurements, also for dye-doped LC materials, where, additionally, a contrast inversion of the diffraction pattern can be observed. This effect was confirmed by our simulations. Calculated Müller matrices for special directions of Bragg reflections are in agreement with measurements made by other groups.

BP crystals were grown and photo-polymerized in two different ways, first by producing a gel of a BP polymer and second by polymerizing a mixture of the LC with a mesogenic monomer. We obtained polymerized crystals in different quality, sufficient for producing clear diffraction patterns.

# 5 SUMMMARY AND CONCLUSIONS

In this thesis we present theoretical and experimental results related to polarization optics of periodic media.

Based on general analytical arguments, we explored the propagation of light in anisotropic media. We figured out conditions for the anisotropic medium, which allow the separation of polarization in 2D and 3D problems.

Plane wave approaches lead to different well established optical matrix concepts. The Jones concept treats coherent light in a complex 2x2 notation and the Stokes concept treats noncoherent light in a real 4x4 notation. We elucidated both concepts and explained the relation between them.

The 4x4 Berreman matrix method, based on the Jones concept, is presented. With the help of this method we designed a cholesteric liquid crystal filter by using the concept of apodization. We extended the 4x4 Berreman method to treat the propagation of noncoherent light in quasi-periodic media. This extension refers to the domain structure of the medium and was applied to the reflection by polymer-dispersed cholesteric liquid crystals. This was used for the investigation of the reflected intensity, the accessible colorspace and depolarization effects. The knowledge of these properties is essential for the use of polymer-dispersed cholesteric liquid crystals in reflective display applications. The reflection properties of different stack arrangements of polymer-dispersed cholesteric liquid crystal cells have been investigated. It was figured out that a stack of cholesteric liquid crystal cells with alternating handedness of the material has a higher reflection than the stack of cells with the same handedness.

As a more rigorous propagation method, based on a direct discretization of the Maxwell equations, we have introduced the finite-difference time-domain method. We applied this method to anisotropic materials in 2D and 3D, e.g. nematic liquid capillaries and “soft” liquid crystal gratings. Comparing the results of such rigorous solutions with those obtained by gradient index and matrix methods we have shown that it is necessary to use an exact method for a correct analysis of the interaction of light with complex periodic and anisotropic media such as polymer-dispersed cholesteric liquid crystals (CLC) used for displays.

We have analyzed Blue Phases as natural photonic crystals structurally, as well as related to their optical properties. By using the double twist cylinder model, the dielectric tensor of the unit cell of the BPII was implemented. In order to investigate the diffraction of Blue Phases we extend the 4x4 Berreman method to the application to anisotropic 3D structures. We have explained and reasoned this extension, which treats obliquely incident light as interacting with an artificial anisotropic lattice perpendicular to the direction of propagation. Using this method we have calculated for the first time (to the

best of our knowledge) the entire diffraction pattern of a BPII including intensity and phase distribution. The diffraction patterns are calculated also for dichroic materials. A contrast inversion effect has been observed and described for these materials. The calculated diffraction patterns have been confirmed by direct measurements of Blue Phase diffraction in the conoscopic plane of a polarization microscope.

Crystals of Blue Phases were grown and stabilized by polymerization in two different ways. The obtained crystals are of different quality, but produce clear diffraction patterns. This is an important step forward to the application of Blue Phase crystals as photonic crystals.

For next steps, it would be interesting to examine different BP structure propositions by using the presented plane wave method. So it will be possible to evaluate such models by optical means. Especially, the influence of the unit cell structure on the polarization properties of the Bragg reflected light would give more information about this type of photonic crystals. Furthermore, a complete bandgap investigation of dye-doped materials can by instructive.

This work was partially founded by the Swiss national science foundation project “Liquid crystalline Blue Phases as Photonic Crystals” contract number FN 66829. In addition, we thank ASULAB S.A. for their support.

## 6 REFERENCES


[Abelès 1950] F. Abelès, *Ann. Phys.* **5**, 598 (1950)

[Abu-Safia et al. 1993] H. A. Abu-Safia, A. I. Al-Sharif, I. O. A. Aljarayesh, *Appl. Opt.* **32**, 4831 (1993)

[Allia et al. 1991] P. Allia, C. Oldano, and L. Trossi, *Linear Optics: Matrix Methods* in *Physics of liquid crystalline materials*, I.-C. Khoo and F. Simoni, eds. Gordon and Breach, New York (1991)

[Azzam & Bashara 1977] R.M.A. Azzam, N.M. Bashara, *Ellipsometry and Polarized Light*, Elsevier Science, Amsterdam (1977)

[Belyakov & Dmitrienko 1989] V. A. Belyakov, V. E. Dmitrienko, *Liq. Cryst.* **5**, 839 (1989)

[Berenger 1994] J. P. Berenger, *J. Computational Physics* **114**, 184 (1994)

[Bergmann et al. 1979] K. Bergmann, P. Pollmann, G. Scherer, H. Stegemeyer, *Z Naturf.* **34a**, 253 (1979)

[Berreman & Scheffer 1970] D. W. Berreman, T. J. Scheffer, *Phys. Rev. Letters* **25**, 577 (1970)

[Berreman 1972] D. W. Berreman, *J. Opt. Soc. Am.* **62**, 502 (1972)

[Berreman 1984] D. W. Berreman in *Liquid Crystals and Ordered Fluids*, Vol. 4, eds. A. C. Griffen and J. F. Johnson, Plenum Press, New York, 925 (1984)

[Blinov & Chigrinov 1994] L. M. Blinov, V. G. Chigrinov, *Electrooptic Effects in Liquid Crystal Materials*, Springer, New York (1994)

[Bohley et al. 2001] C. Bohley, T. Scharf, R. Klappert, J. Grupp, *SPIE Proceedings* (*Liquid Crystals V)* **4463**, 181 (2001)

[Bohley & Scharf 2002] C. Bohley, T. Scharf, *Opt. Comm.* **214**, 193 (2002)

[Bohley & Scharf 2003] C. Bohley, T. Scharf, *Proc. SPIE Vol. 5184, Physics, Theory and Applications of Periodic Structures in Optics II,* 202 (2003)

[Bohley & Scharf 2004] C. Bohley, T. Scharf, *J. Opt. A* **6**, 77 (2004)

[Born & Wolf 1959] M. Born, E. Wolf, *Principles of Optics*, Pergamon, New York (1959)

[Bos et al. 1995] P. J. Bos, J. Chen, J. W. Deane, B. Smith, C. Holton, W. Glenn, presented at SID 95 Digest, (1995)

[Brosseau 1998] C. Brosseau, *Fundamentals of Polarized Light*, Wiley, New York (1998)

[Cao et al. 2002] W. Cao, A. Munoz, P. Palffy-Muhoray, B. Taheri, *Nature Mat.* **1**, 111 (2002)

[Chandezon 1980] J. Chandezon, G. Raoult, D. Maystre, *Journal of Optics* **11**, 235 (1980)

[Churchill 1960] R. V. Churchill, *Complex Variables and Applications*, McGraw-Hill, Tokyo (1960)

[Crooker & Kitzerow 1992] P.P. Crooker, H.-S. Kitzerow, *Cond. Mater. News* **1**, 6 (1992)

[Dändliker 1997] R. Dändliker, *Fifth international topical meeting on education and training in optics*, SPIE **3130**, 279 (1997)

[Davis et al. 1998] D. Davis, A. Kahn, X.Y. Huang, J.W. Doane, C. Jones, *Eight color High-Resolution Reflective Cholesteric LCDs*, SID Digest **31.2** (1998)

[de Gennes 1993] P. G. de Gennes, *The Physics of Liquid Crystals*, Clarendon Press, Oxford (1993)

[Delort & Maystre 1993] T. Delort, D. Maystre, *J. Opt. Soc. Am.* **10**, 2592 (1993)

[Demus & Richter 1978] D. Demus, L. Richter, *Textures of Liquid Crystals*, Verlag Chemie, New York (1978)

[Drzaic 1995] P. S. Drzaic, *Liquid Crystal Dispersions*, World Scientific Publishing (1995)
[Dubois-Violette & Pansu 1988] E. Dubois-Violette, P. Pansu, *Mol. Cryst. Liq. Cryst.* **165**, 151 (1988)
[Flack et al. 1982] J. H. Flack, P. P. Crooker, R. C. Svoboda, *Physical Review A* **26**, 723 (1982)
[Gedney 1996] S. D. Gedney, *IEEE Trans. Antennas and Propagation* **44**, 1630 (1996)
[Gerrard & Burch 1975] A. Gerrard, J. M. Burch, *Introduction to Matrix methods in Optics*, Dover, New York (1975)
[Geurst et al. 1975] J. A. Geurst, A. M. J. Spruijt, C. J. Gerritsma, *J. de Phys.* **36**, 653, (1975)
[Goodman 1985] J. W. Goodman, *Statistical Optics*, Wiley, New York (1985)
[Goodman 1996] J. W. Goodman, *Introduction to Fourier Optics*, 2nd International Edition ed., McGraw Hill, New York (1996)
[Gray & Winsor 1974] G. W. Gray, P. A. Winsor, *Liquid Crystals and Plastic Crystals*, Ellis Horwood, Chichester, Vol. 1 (1974)
[Grebel et al. 1984] H. Grebel, R. M. Hornreich, S. Shtrikman, *Phys. Rev. A* **30**, 3264 (1984)
[Harrington 1968] R. F. Harrington, *Field Computation by Moment Methods*, Macmillan, New York (1968)
[Hashimoto et al. 1998] K. Hashimoto, M. Okada, K. Nishiguchi, N. Masazumi, E. Yamakawa, T. Taniguchi: *Reflective Color Display Using Cholesteric Liquid Crystals*, SID Digest **31.1** (1998)
[Courant & Hilbert 1931] R. Courant, D. Hilbert, *Methoden der Mathematischen Physik*, Springer Verlag, Berlin (1931)
[Hornreich & Shtrikman 1981] R. M. Hornreich, S. Shtrikman, *Phys. Lett.* **82A**, 354 (1981)
[Hornreich & Shtrikman 1993] R. M. Hornreich, S. Shtrikman, *Phys. Rev.E* **47**, 2067 (1993)
[Jérôme & Pieranski 1989] B. Jérôme, J. Pieranski, *Liq. Cryst.* **5**, 799 (1989)
[John et al. 1995] W. D. St. John, W. J. Fritz, Z. J. Lu, D.-K. Yang, *Physical Review E* **51**, 1191 (1995)
[Jones 1941] R. C. Jones, *J. Opt. Soc. Am.* **31**, 488 (1941)
[Jones 1956] R. C. Jones, *J. Opt. Soc. Am.* **46**, 126 (1956)
[Keller 1962] J. B. Keller, *J. Opt. Soc. Am.* **52**, 116 (1962)
[Khan et al. 2001] A. Khan, X.-Y. Huang, R. Armbruster, F. Nicholson, N. Miller, B. Wall, J. W. Doane, SID 01 Digest **27** (2001)
[Khoo 1988] I. C. Khoo, *Prog. Opt.* **27**, 105 (1988)
[Kikuchi et al. 2002] H. Kikuchi, M. Yokota, Y. Hisakado, H Yang, T. Kajiyama, *Nature Materials* **1**, 64 (2002)
[Kogelnik 1969] H. Kogelnik, *Bell System Tech. J.* **48**, 2909 (1969)
[Kosmopoulos & Zenginoglou 1987] J. A. Kosmopoulos, H. M. Zenginoglou, *Appl. Opt.* **26**, 1714 (1987)
[Kossel et al. 1935] W. Kossel, V. Loeck, H. Voges, *Z. Phys.* **94**, 139 (1935)
[Kriegsmann et al. 1987] G. A. Kriegsmann, A. Taflove, K. R. Umashankar, *IEEE Trans. Antennas and Propagation* **35**, 1248 (1987)
[Kriezis & Elston 2000] E. E. Kriezis, S. J. Elston, *Opt. Comm.* **177**, 69 (2000)
[Kriezis 2002] E. E. Kriezis, *Microwave and Optical. Technology Letters* **35(6)**, 437 (2002)
[Kunz & Lee 1978] K. S. Kunz, K. M. Lee, *IEEE Trans. Electromagnetic Compatibility* **20**, 328 (1978)
[Lehmann 1906] O. Lehmann, *Z. Phys. Chem.* **56,** 750 (1906)

[Li 1997] L. Li, *J. Opt. Soc. Am. A* **14**, 2758 (1997)
[Li 1998] L. Li, *J. Mod. Opt.* **45,** 1313 (1998)
[Maystre 1978] D. Maystre, *J. Opt. Soc. Am.* **68**, 490 (1978)
[Meiboom et al. 1981] S. Meiboom, J. P. Sethna, P. W. Anderson, W. F. Brinkmann, *Phys. Rev. Lett.* **46**, 1216 (1981)
[McMaster 1961] W. H. McMaster, *Rev. mod. Phys.* **33,** 8 (1961)
[Memmer 2000] R. Memmer, *Liq. Cryst.* **27(4)**, 533 (2000)
[Miller & Gleeson 1996] R. J. Miller, H. F. Gleeson, J. E. Lydon, *Phys. Rev. Lett.* **77(5)**, 857 (1996)
[Moharam & Gaylord 1982] M. G. Moharam, T. K. Gaylord, *J. Opt. Soc. Am.* **72**, 1385 (1982)
[Morf 1995] R. H. Morf, *J. Opt. Soc. Am.* **12,** 1043 (1995)
[Mur 1981] G. Mur, *IEEE Trans. Electromagnetic Compatibility* **23**, 377 (1981)
[Okano et al. 1994] K. Okano, K. Kitahara, E. Ushizawa, *Jpn. J. Appl. Phys.* **33**, 6262 (1994)
[Oswald & Pieranski 2000] P. Oswald, P. Pieranski, *Les Cristaux Liquides*, Gordan and Breach, Paris (2000)
[Peréz et al. 1998] I. V. Peréz, S. G. García, R. G. Martín, B. G. Olmedo, *Microwave Opt. Technol. Lett.* **18**, 126 (1998)
[Petit 1980] R. Petit, ed. *Electromagnetic theory of gratings*, Springer-Verlag, Berlin (1980)
[Rayleigh 1907] Lord Rayleigh, *Proc. Roy. Soc. Ser. A* **79**, 399 (1907)
[Reinitzer 1888] F. Reinitzer, *Monatsh. Chem* **9**, 412 (1888)
[Reyes 1998] J. A. Reyes, *Phys. Rev. E* **57**, 6700 (1998)
[Rokhsar & Sethna 1986] D. S. Rokhsar, J. P. Sethna, *Phys. Rev. Lett.* **56**, 1727 (1986)
[Sacks et al. 1995] Z. S. Sacks, D. M. Kingsland, R. Lee, J. F. Lee, *IEEE Trans. Antennas and Propagation* **43**, 1460 (1995)
[Sah & Suresh 1994] Y. Sah, K. A. Suresh, *J. Opt. Soc. Am.* **11(2)**, 740 (1994)
[Saleh &Teich 1991] B. E. A. Saleh, M. C. Teich, *Fundamentals of Photonics*, John Wiley & Sons, New York (1991)
[Saupe 1969] A. Saupe, *Mol. Cryst. Liq. Cryst.* **7**, 59 (1969)
[Scharf 2000] T. Scharf, presented at 29. Arbeitstagung Flüssigkristalle, Freiburg Breisgau (2000)
[Scharf & Bohley 2002] T. Scharf, C. Bohley, *Mol. Cryst. Liq. Cryst.* **375**, 491 (2002)
[Schwarzenbach 1993] D. Schwarzenbach, *Cristallographie*, Presses Polytechnique et universitaires romandes, Lausanne (1993)
[Southwell 1989] W. H. Southwell, *Appl. Opt.* **28**, 5091 (1989)
[Taflove & Brodwin 1975a] A. Taflove, M. E. Brodwin, *IEEE Trans. Microwave Theory and Techniques* **23**, 623 (1975)
[Taflove & Brodwin 1975b] A. Taflove, M. E. Brodwin, *IEEE Trans. Microwave Theory and Techniques* **23**, 888 (1975)
[Taflove & Hagness 2000] A. Taflove, S. C. Hagness, *Computational Electrodynamics*, Artech House, Boston (2000)
[Titus et al. 1999] C. M. Titus, P. J. Bos, J. R. Kelly, E. C. Gartland, *J. Appl. Phys.* **38**, 1488 (1999)
[Umashankar & Taflove 1982] K. R. Umashankar, A. Taflove, *IEEE Trans. Electromagnetic Compatibility* **24**, 397 (1982)
[Vitek & Kléman 1975] V. Vitek, M. Kléman, *J. de Phys.* **36**, 59 (1975)
[de Vries 1951] H. de Vries, *Acta Cryst.* **4**, 219 (1951)
[Warenghem & Henninot 1998] M. Warenghem, J. F. Henninot, *Opt. Express* **2(12)**, 483 (1998)

[Waterman 1975] P. C. Waterman, *J. Acoust. Soc. Am.* **57**, 791 (1975)
[Witzigmann et al. 1998] B. Witzigmann, P. Regli, W. Fichtner, *J. Opt. Soc. Am. A* **15**, 753 (1998)
[Wright & Mermin 1989] D. C. Wright, N. D. Mermin, *Rev. Mod. Phys.* **61**, 385 (1989)
[Wu & Yang 2001] S.-T. Wu, D.-K. Yang, *Reflective Liquid Crystal Displays*, Wiley, New York (2001)
[Yariv 1997] A. Yariv, *Optical Electronics in Modern Communications*, Oxford University Press, New York (1997)
[Yariv &Yeh 1984] A. Yariv, P. Yeh, *Optical Waves in Crystals*, Wiley, New York (1984)
[Yee 1966] K. S. Yee, *IEEE Trans. Antennas and Propagation* **14**, 302 (1966)
[Yeh & Gu 1999] P. Yeh, C. Gu, *Optics of Liquid Crystal Displays*, Wiley, New York, (1999)
[Yeh 1979] P. Yeh, *J. Opt. Soc. Am.* **69**, 742 (1979)
[Ziolkowski 1997] R. W. Ziolkowski, *IEEE Trans. Antennas Propagat.* **45**, 375 (1997)
[Zumer 1988] S. Zumer, *Phys. Rev. A* **37**, 4006 (1988)

## ACKNOWLEDGEMENTS

Thanks to:

- Prof. René Dändliker for his work as thesis advisor and director. He gave me the opportunity to work in the field of optical physics. I appreciate his didactic capabilities and clear explications of complex things.
- Dr. Toralf Scharf for warm meals and being my direct supervisor. This man is brim-full of ideas and nevertheless, he introduced me patiently into the field of optics.
- Prof. Hans-Peter Herzig and Dr. Holger Stark for reviewing the thesis and being members of the jury.
- Dr. Joachim Grupp for the same and the interesting 7 months at ASULAB S.A. in 1998/1999.
- The Applied Optics group at the Institute of Microtechnology for their collegial support.
- Carsten Rockstuhl for fruitful cooperation, professional and amicable support, interesting discussions. This human being has antennae for different ranges and a brain to process the recorded information.
- Christophe Weiteneder for being friend and jogging partner.
- Dr. Gerben Boer for the office colleague he was and for introducing me into the mysterious mores of the Neuchâtel natives.
- Omar Manzardo, for the jazz music we played together and late discussions.
- Alexis Gabadinho for speaking French with me and correcting me. Following the grammarian Alexander, who repeated the false phrase discretely in the right way.
- Dr. Martin Salt for correcting my German English (these acknowledgements, too).
- Prof. Siegfried Hoffmann for showing me that science is more than science.
- My mathematics school teacher Klaus Pigorsch.
- The writers Robert Walser, Musil and “Paare, Passanten” of Botho Strauss.
- My parents for everything they have done for me.
- My daughter Annabell for encouraging me and waiting for me these years.
- My girlfriend P for being there for me.